IMAGING OF SLOW DISSOCIATION OF THE LASER INDUCED FRAGMENTATION OF MOLECULAR IONS

by

BISHWANATH GAIRE

M.S., Tribhuvan University, Nepal, 2001

AN ABSTRACT OF A DISSERTATION

submitted in partial fulfillment of the
requirements for the degree

DOCTOR OF PHILOSOPHY

Department of Physics
College of Arts and Sciences

KANSAS STATE UNIVERSITY
Manhattan, Kansas
2011

Abstract

Lasers are being used widely for the study and manipulation of the dynamics of atomic and molecular targets, and advances in laser technology makes it possible to explore new areas of research — for example attosecond physics. In order to probe the fragmentation dynamics of molecular ions, we have developed a coincidence three-dimensional momentum imaging method that allows the kinematically complete study of all fragments except electrons. Recent upgrades to this method allow the measurement of slow dissociation fragments, down to nearly zero velocity, in intense ultrafast laser fields. Evidences for the low energy breakup are presented using the benchmark molecules diatomic H_2^+ and polyatomic H_3^+. The low energy fragments in H_2^+ dissociation are due to the intriguing zero-photon dissociation phenomenon. This first experimental evidence for the zero-photon dissociation is further supported by sophisticated theoretical treatment. We have explored the laser pulse length, intensity, wavelength, and chirp dependence of zero-photon dissociation of H_2^+, and the results are well described by a two-photon process based on stimulated Raman scattering. Similar studies of the slow dissociation of H_3^+ reveal that two-body dissociation is dominant over three-body dissociation. The most likely pathways leading to low-energy breakup into $H^+ + H_2$, in contradiction to the assessments of the channels in at least one previous study, are explored by varying the laser pulse duration and the wavelength. In addition, we have investigated the dissociation and single ionization of N_2^+, and an interesting high energy feature in addition to the low energy has been observed at higher intensities. Such high energy results from the breakup of molecules in excited states are accessible at higher intensities where their potential energy is changing rapidly with the internuclear distance. We have extended the intense field ionization studies to other molecular ions N_2^+, CO^+, NO^+, and O_2^+. The dissociative ionization of these molecules follow a general mechanism, a stairstep

ionization mechanism. Utilizing the capability of the upgraded experimental method we have measured the non-dissociative and dissociative ionization of CO^+ using different pulse lengths. The results suggest that dissociative ionization can be manipulated by suppressing some ionization paths.

IMAGING OF SLOW DISSOCIATION OF THE LASER INDUCED FRAGMENTATION OF MOLECULAR IONS

by

BISHWANATH GAIRE

M.S., Tribhuvan University, Nepal, 2001

A DISSERTATION

submitted in partial fulfillment of the
requirements for the degree

DOCTOR OF PHILOSOPHY

Department of Physics
College of Arts and Sciences

KANSAS STATE UNIVERSITY
Manhattan, Kansas
2011

Approved by:

Major Professor
Itzik Ben-Itzhak

Copyright

Abstract

Lasers are being used widely for the study and manipulation of the dynamics of atomic and molecular targets, and advances in laser technology makes it possible to explore new areas of research — for example attosecond physics. In order to probe the fragmentation dynamics of molecular ions, we have developed a coincidence three-dimensional momentum imaging method that allows the kinematically complete study of all fragments except electrons. Recent upgrades to this method allow the measurement of slow dissociation fragments, down to nearly zero velocity, in intense ultrafast laser fields. Evidences for the low energy breakup are presented using the benchmark molecules diatomic H_2^+ and polyatomic H_3^+. The low energy fragments in H_2^+ dissociation are due to the intriguing zero-photon dissociation phenomenon. This first experimental evidence for the zero-photon dissociation is further supported by sophisticated theoretical treatment. We have explored the laser pulse length, intensity, wavelength, and chirp dependence of zero-photon dissociation of H_2^+, and the results are well described by a two-photon process based on stimulated Raman scattering. Similar studies of the slow dissociation of H_3^+ reveal that two-body dissociation is dominant over three-body dissociation. The most likely pathways leading to low-energy breakup into $H^+ + H_2$, in contradiction to the assessments of the channels in at least one previous study, are explored by varying the laser pulse duration and the wavelength. In addition, we have investigated the dissociation and single ionization of N_2^+, and an interesting high energy feature in addition to the low energy has been observed at higher intensities. Such high energy results from the breakup of molecules in excited states are accessible at higher intensities where their potential energy is changing rapidly with the internuclear distance. We have extended the intense field ionization studies to other molecular ions N_2^+, CO^+, NO^+, and O_2^+. The dissociative ionization of these molecules follow a general mechanism, a stairstep

ionization mechanism. Utilizing the capability of the upgraded experimental method we have measured the non-dissociative and dissociative ionization of CO^+ using different pulse lengths. The results suggest that dissociative ionization can be manipulated by suppressing some ionization paths.

Table of Contents

List of Figures

List of Tables

Acknowledgments

I would take this opportunity to thank many people who have provided their guidance, contribution, and support to me during the course of this research work over the years.

I would like to sincerely thank my supervisor, Professor Itzik Ben-Itzhak for his outstanding guidance, teaching, and enthusiasm of scientific work. He has been very encouraging and supportive throughout my time in the group and has made every effort to guide me to the next level. He has given me the freedom to organize the experiments the way I wanted so that I could develop my experience at leading projects and I really feel fortunate for these opportunities.

I would like to acknowledge Professor Kevin Carnes, without whom it would not be possible for me to get this work into this form — he has provided me with much help and support. He always kept his door open for me whenever I had an issue with computer language programming or needed technical advice for the experiment. He taught me not only good Physics but also good English in order to be very clear in scientific writing.

I am extremely grateful to the other members, former and current, of Itzik's research group. Post-doctoral researcher Dr. Pengqian Wang offered me the basics of the experimental method and I would like to thank you Pengqian for all the ideas on running the experiments at the early stage when I joined the group. Same applies to Dr. Arthur Max Sayler who has spent time teaching me all the steps from data sorting to electronics. Many thanks to Dr. Jarlath McKenna for his interest, guidance, and endless help in my understanding and scientific work. Jarlath, I owe a lot to you, you helped me in every step from conducting experiments through to analysis and correcting my writing including this thesis. I wish you all the best for your career. I would like to say thank you to all the excellent graduate and undergraduate students; Nora G. Johnson, Mohammad Zohrabi, Utuq Ablikim, Ben Berry, Mat Leonard, Eli Parke, Adam Summers, Sam Haugland and REU students Forest Roberts, David Miller, Bret Polopolus, Sam Roland, and Bethany Jochim.

It has been a great experience to know and work with you all. Mohammad, you helped me a lot when it was just you and me to run the experiments; I wish you all the best for the rest of your research work. Same goes to you Nora, with whom I learned much together in the earlier stages. And to Utuq and Ben and I hope you already have had a good start by having a couple of research projects. Forest Roberts, Bret Polopolus and Adam Summer have done simulations with the deflector and a huge thank you to you all.

I wish to thank Professor Brett Esry and his group (especially Dr. Fatima Anis and Jianjua Hua) for invaluable theoretical contributions to this project. I have learnt very much ranging from the basics to the highly advanced in AMO physics through his classes and from discussions with him. I would like to thank Professor Lew Cocke for his fruitful discussions on some of the projects and help for my career. Same goes to Professor Zenghu Chang, I have had an opportunity to learn about the laser systems from the optics classes he offered.

The experimental results discussed in this work are made possible with the help and support of Dr. Charles Fehrenbach for the ion beam and the KLS group for laser beam. Professor Zenghu Chang's group (especially Dr. Hiroki Mashiko, Dr. Kun Zhao and Yi Wu) have provided their expertise in producing the laser beam. I would like to thank all of you.

I would also like to thank all the JRML personnels and the staffs of the Physics Department, for being extremely helpful and supportive during my stay in KSU.

I would like to express my sincere thanks to Professor J Kenneth Shultis, Professor Brett Esry, Professor Zenghu Chang, Professor Kevin Carnes, and Professor Daniel Higgins for kindly agreeing to be in my thesis committee. Professor Kevin Carnes is kind enough to replace Professor Zenghu Chang, who is unable to to attend due to his demanding schedule for the final exam.

Finally, I am deeply grateful to my entire family, grandmother, father, mother, brothers, and sisters, for their love, help, and support despite being physically far for years and I thank you all. In addition, a huge thank you to my wife Kabita for the support and sacrifices that

she has made while I was in graduate school, taking very good care of our daughters Bidushi (four years) and Kamana (two months), and too many other things to list.

This work was supported by the Chemical Sciences, Geosciences, and Biosciences Division, Office of Basic Energy Sciences, Office of Science, U.S. Department of Energy.

Dedication

Dedicated to my family

Chapter 1

Introduction

1.1 Motivation

The study of laser[1]-matter interactions leads to a fundamental understanding of the structure and properties of the matter and also of the behavior of atoms and molecules in response to electromagnetic radiation. There is a growing interest in the interaction of lasers with diffuse matter, as this will lead to new ways to probe and manipulate chemical reactions [1–3]. Advances in laser technology, e.g. shorter and brighter bursts of electromagnetic energy, are creating new opportunities in this respect [3–5]. Atoms and molecules in the gas phase are commonly used targets for these studies. Molecules provide a richer scope for study compared to atoms, as they pose some additional degrees of freedom, e.g. they can vibrate and/or rotate, which are sometimes challenging in experiments. For example, measurements of vibrational and rotational energy spectra require better resolution. Molecular ions probed in an intense laser field are produced from neutral molecules either by ionizing them with the same laser pulse or by using an ion beam extracted from an ion source. The ions produced by these methods have some advantages and disadvantages over each other that will be discussed later. In the context of the present study we probe a fast beam of molecular ions with intense ultrashort laser pulses.

[1]The word laser stands for Light Amplification by Stimulated Emission of Radiation.

1.2 Focus

The focus of the present work is on slow dissociation of the molecular ions induced by ultrashort intense laser pulses. In this context, slow dissociation means the molecule breaks into fragments, without losing any electrons, that carry very low kinetic energy, typically of the order of 0.1 eV or less. These molecular ion beam targets enable (i) kinematically complete studies of dissociation as both neutral and ionic fragments can be detected (ii) studies of key molecular systems that are simpler or non existing in the form of neutral molecules and (iii) exploration of the system at relatively low laser intensities. We specifically use the benchmark molecules H_2^+ — the one electron diatomic molecule, H_3^+ — the simplest polyatomic molecule, and some other small many-electron diatomic molecules like O_2^+ for these slow dissociation studies. To facilitate this study a major upgrade of the experimental method was needed in order to enable measurements of fragments with low breakup energy down to nearly 0 eV.

The choice of an O_2^+ target is mainly to present evidence of the capabilities of our upgraded method. This molecule is also chosen to verify that the low energy breakup has a higher probability than high energy breakup as expected from the structure of this molecule. In contrast to O_2^+, slow dissociation of H_2^+ is expected to have lower probability than fast dissociation, and its measurement gives us more confidence about the method. Such low energy breakup studies of H_2^+ provide insight into the validity of the previously reported mechanisms of a slow dissociation [6–8]. In the case of H_3^+, it is to show the extension of the method to a polyatomic system and to add to the fundamental understanding of the physical mechanisms responsible for low energy dissociation.

In addition to studies of slow dissociation, we also discuss fast dissociation, *i.e.* releasing higher energy (of the order of 4—10 eV) in the dissociation and ionization of many electron molecules, *i.e.* stripping electrons from molecules using intense laser pulses. In single ionization, *i.e.* removing only one electron, the molecule can either break up into two charged fragments, known as dissociative ionization, or remain in a metastable state without

breaking into fragments, known as non-dissociative ionization. We will discuss mechanisms for such breakup of the molecules.

Before going into the introductory details of the mechanisms involved in laser induced dissociation and ionization of molecules, the outline of this dissertation is presented next.

1.3 Document organization

The last section of this chapter describes the relevant molecular dissociation and ionization mechanisms that are useful for understanding the experimental results presented in this document. The main core of the present work will focus on the slow dissociation of the benchmark molecules H_2^+ and H_3^+ in ultrashort intense laser pulses as discussed in the next chapters.

Chapter Two, entitled "Experimental Method", will begin with the method that was used for previous studies followed by a more detailed description of the method designed specifically for the imaging of laser induced slow dissociation of molecular ions. We also report some results as evidence for the capabilities of this method. In fact this upgraded setup also works for studies of dissociative and non-dissociative ionization of many-electron homonuclear and heteronuclear (nearly mass symmetric [2]) diatomic molecules.

In Chapter Three, entitled "Slow Dissociation of Molecular Ions", we present the measurements of slow dissociation of H_2^+ and H_3^+ and discuss the mechanisms of such low energy breakup. Chapter Four, entitled "Fast Dissociation and Ionization of N_2^+", begins with the studies of dissociation of N_2^+ that shows two distinct features, *i.e.* low and high energy breakup. We present the pathways of dissociation and then the ionization mechanism.

Chapter Five, entitled "Laser Induced Ionization of Molecules", begins with the studies of the laser induced dissociative ionization of many-electron diatomic molecules N_2^+, CO^+, NO^+ and O_2^+. Then we discuss the non-dissociative ionization of CO^+. We conclude with Chapter Six, entitled "Summary and Future Directions". We present a summary of the

[2]Heteronuclear where the nuclear masses are not very different, e.g. CO^+ in contrast to very different masses, e.g. OH^+.

importance of the intense field studies discussed in this work and the possible directions for further studies in the future with this new experimental method.

Finally, Appendices cover mostly the technical aspects of this work that are useful in using the method and the setup discussed here.

Below we present the main underlying mechanisms in laser-molecule interactions that are relevant to our present study.

1.4 Mechanisms of molecular fragmentation

The interaction of an intense laser pulse with diffuse matter in the form of atoms, molecules, and molecular ions has been explored widely (see reviews in [9–12]). The simplest molecule, H_2^+, is a preferred target for both theory and experiment. It serves as a testing ground since exploring the physics of this single electron system is a much less demanding task than studying a more complex many-electron system. In the intense field the molecules either dissociate, by a low-order photon absorption leading to low-energy breakup resulting in a neutral atom and an ionic fragment, or ionize releasing higher energy due to repulsion between the ionic fragments. Some of the important mechanisms that have been observed in these studies and are useful in understanding laser-matter interactions include bond softening (BS) [13, 14], vibrational trapping (VT, also known as bond hardening) [15], above-threshold dissociation (ATD) [14, 16, 17], and Coulomb explosion (CE) [18–20].

Typically, in a strong laser field, molecular dissociation yields a kinetic energy release (KER) that is much lower than what one would expect for photodissociation in the weak field limit. This has led to the discovery of the bond softening mechanism [13, 14]. In order to understand the dissociation mechanisms we use a Floquet representation [10, 21–26] with laser-dressed potentials. An alternative picture, where a transition between any two states is represented by vertical up and down arrows corresponding to the absorption and emission of photons, respectively (see e.g. Ref. [27]), is also in common use.

In the diabatic Floquet representation the emission and absorption of n photons corre-

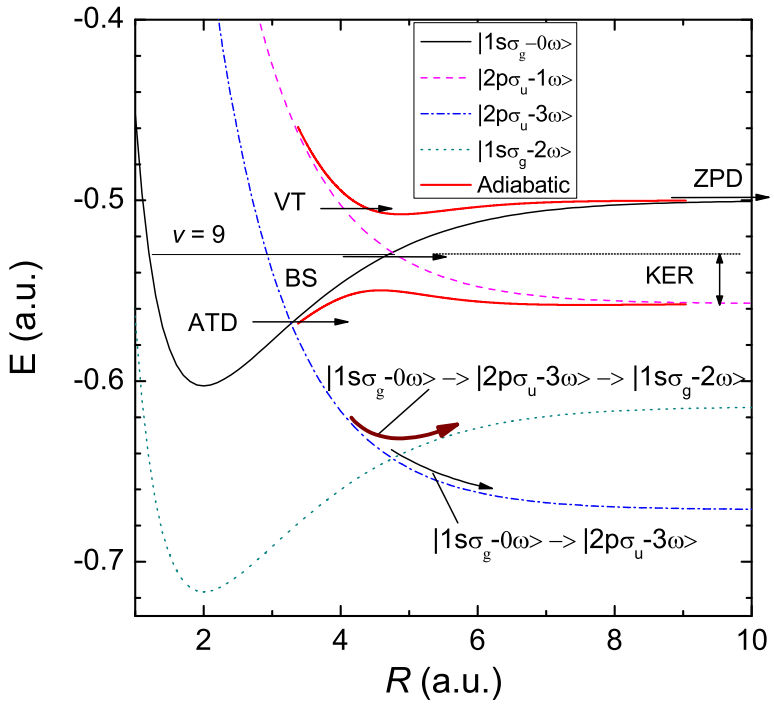

Figure 1.1: *Born-Oppenheimer potentials of H_2^+, dressed by net absorbed number of photons, $n\omega$ for 790 nm light. Also indicated are the vibrational trapping (VT), bond softening (BS), zero-photon dissociation (ZPD), and above-threshold dissociation (ATD) mechanisms.*

sponds to the up or down shift of the Born-Oppenheimer potential energy curves (PECs) by n times the photon energy, $\pm n\omega$, respectively. The resulting dressed states are denoted by the state followed by the label $\pm n\omega$, as shown in Fig. 1.1. For example, the $2p\sigma_u$ state after one photon absorption is denoted as $|2p\sigma_u - 1\omega>$. A molecular transition between different photon dressed potentials occurs by diabatic coupling. Figure 1.1 shows the laser-dressed diabatic $1s\sigma_g$ and $2p\sigma_u$ Born-Oppenheimer potential energy curves (PECs) of H_2^+ in the Floquet representation. The next higher lying excited electronic states are about 11 eV above the dissociation threshold of the $1s\sigma_g$ and $2p\sigma_u$ (much greater than the photon energy 1.57 eV of 790 nm light) and hence are not shown here.

We have shown the adiabatic Floquet PECs, for which the field dressed diabatic potentials with dipole coupling are diagonalized, in Fig. 1.1, in addition to the diabatic curves. Now, the crossing between the diabatic curves becomes an avoided crossing, *i.e.* the en-

ergy gap near the $|1s\sigma_g - 0\omega>$ and $|2p\sigma_u - 1\omega>$ crossing in Fig. 1.1 becomes wider with the increasing strength of the laser field. One can imagine the formation of a potential well of different width and depth above this crossing depending on the laser field strength. Non-adiabatic coupling determines the transition between different adiabatic pathways.

A molecule, near the diabatic crossing of $|1s\sigma_g - 0\omega>$ and $|2p\sigma_u - 1\omega>$, can make a transition governed by molecular dipole selection rules between the curves. In the adiabatic picture there is a gap, and the molecule then dissociates through the process of bond softening [13, 14] (marked as BS in Fig. 1.1). Basically, when the light interacts with the molecules the height of the potential barrier of an electronic state of the molecule is suppressed to an energy below the energy of an occupied vibrational level (e.g. vibrational level v=9 in Fig. 1.1) such that the molecule can dissociate. The molecule can also tunnel through the barrier as the barrier width is reduced, however the likelihood of tunneling is small compared to the dissociation over the barrier as the reduced mass of the molecule is large. Though the transition probability is larger for the vibrational states close to the crossing, other vibrational states lying above or below the crossing can make a transition to the $|2p\sigma_u - 1\omega>$ curve and dissociate by BS with net one photon absorption.

In addition, vibrational states just above the crossing of $|1s\sigma_g - 0\omega>$ and $|2p\sigma_u - 1\omega>$ may be trapped in the shallow potential well formed only when the laser is present. This process is named vibrational trapping [8, 11, 15] and is shown schematically in Fig. 1.1 with the label VT. However, this mechanism is only present in the simplified one dimensional aligned model calculations [10], which do not include nuclear rotation, that solve the Schrödinger equation for H_2^+ potentials. This phenomenon, sometimes also referred to as "stabilization", disappears in the calculations that include nuclear rotation as discussed in Ref. [28, 29].

When dissociation occurs by the absorption of more than the net minimum number of photons needed for dissociation, e.g. $|2p\sigma_u - 3\omega>$, it is called above-threshold dissociation [16, 17, 30], in analogy to above-threshold ionization [31] where the photoelectron spectrum shows peaks separated by photon energy. The vibrational states near the crossing of $|1s\sigma_g -$

$0\omega>$ and $|2p\sigma_u - 3\omega>$ have a higher probability of dissociating by ATD along the $|2p\sigma_u - 3\omega>$ state. This transition can follow more than one pathway, *i.e.* it can either remain on the $|2p\sigma_u - 3\omega>$ curve or end up on the $|1s\sigma_g - 2\omega>$ curve by a transition at the next crossing between the $|1s\sigma_g - 2\omega>$ and $|2p\sigma_u - 3\omega>$ states. The latter pathway results in the stimulated emission of a photon. Since it is the adiabatic path it is more likely to occur in the presence of the laser field [30]. This latter transition is indicated with a thick curved arrow in Fig. 1.1. For both ATD pathways the KER is larger than for dissociation by the bond softening mechanism. In general, ATD has a higher KER and a lower probability of occurring than BS because of the larger number of photons involved.

Similar to molecular dissociation by BS, ionization of molecules typically yields lower KER than that predicted for ionization at their equilibrium internuclear distance (R_e). This is due to enhanced ionization [32, 33], *i.e.* higher ionization probability, for stretched molecules with larger internuclear separation R than R_e. This mechanism can be viewed as ionization of the molecule along its dissociation path. Moreover, like dissociation, ionization may also be explained using the dressed-states picture as demonstrated recently by Esry *et al.* [34] in order to explain the structures observed in the ionization of H_2^+, H_2 [35–37] and also in the case of N_2^+ ionization [38]. While fundamentally this is a multiphoton interpretation (explicitly referring to photons), it is still useful even in the intensity regime where ionization would traditionally be described as occurring by electron tunneling. Indeed, as pointed out by Esry *et al.* [34], the multiphoton dressed-states picture works best near the appearance intensity for ionization where curve crossings just begin to open (*i.e.* crossings between the dressed $1/R$ ionization and dressed dissociation curves), and hence the observation of the peaks in the KER from different paths is possible. At higher intensities, these KER peaks are broadened from their low intensity values and therefore the structure is washed out. This can be viewed as a widening of the avoided curve crossings at high intensity, just like the adiabatic curves in Fig. 1.1, leading to ionization over a broader range of internuclear separation R and hence wider KER spread.

One of the mechanisms in intense field ionization is tunnel ionization [39], where the electron tunnels through the potential barrier in the presence of the laser field. This is the first step in the three step model [3, 40, 41] used to explain high harmonic generation and other strong field phenomena. Electron rescattering [40] is a phenomenon associated with tunnel ionization. When an electron is ionized from the molecule in the presence of a periodic linearly polarized laser field, this ionized electron gains energy in the electric field of the laser and returns to the parent ion after typically $\sim$3/4 of a laser cycle. This is referred to as a rescattered electron and it can excite or ionize an additional electron(s) from the core or get captured while emitting radiation, a process known as high harmonic generation [5, 42, 43]. High harmonic generation enables the generation of attosecond pulses that opens an interesting area of research [3, 44]. In the case that the electron does not gain enough energy from the field after tunneling, it can be captured by the Coulomb potential of the ion and leave the atom in a highly excited state, a mechanism referred to as frustrated tunneling ionization [45]. For molecules this frustrated tunneling ionization mechanism can lead to very high energy in the dissociation with the excited neutrals [46]. One can test the electron rescattering mechanism by using circularly polarized light as the ionized electron does not have a chance to come back to the parent ion.

Another commonly used phenomenon to describe the ionized molecules is Coulomb explosion (CE) [18–20, 47–49]. This occurs when the laser field is intense enough so that the molecule is ionized to a repulsive potential energy curve (PEC), often approximated by a Coulomb potential given by $q_1 q_2/R$ (in atomic units), where q_1 and q_2 are the atomic charges. The fragments thus repel each other and "explode". By measuring the KER distribution and assuming that ionization occurs rapidly on a Coulombic potential, the R dependence of ionization can be retrieved from the measured KER distribution. This is the basic idea for the Coulomb explosion imaging technique [20, 50]. That is, if ionization occurs at small R the resulting fragments share high KER, and at large R they share low KER.

A phenomenon often observed in the intense field molecular ionization is alignment.

There are generally two types of alignment to consider, *geometric* and *dynamic* alignment [11, 51–53].

Geometric alignment: Molecules that are aligned at some angle with respect to the electric field of the laser are ionized preferentially over other molecules. This angle dependent nature of the ionization of molecules is called geometric alignment and is different for each molecule, mainly dependent on the shape of the orbital of the valence electrons [54]. This rate and angular dependence of the ionization of molecules based on the shape of the valence electronic cloud has been predicted by the *Molecular Ammosov-Delone-Krainov (MO-ADK) theory* [54]. Furthermore, this model successfully explains the enhancement and suppression of the ionization rate of some molecules over atoms with similar ionization potential [55].

Dynamic alignment: It is possible for molecules to align themselves in the presence of the laser due to the torque exerted by the electric field of the laser. This behavior is called dynamic alignment [52, 53]. In addition to alignment during the laser pulse, it has also been shown that the molecules can continue to align after the pulse, a phenomenon referred to as *post-ionization alignment* [56–58]. Classically, this phenomenon is discussed using a rigid rotor model. Quantum mechanically, it is explained in terms of populating multiple rotational levels leading to a higher degree of alignment [59].

In addition, let us introduce two very common ionization mechanisms that are relevant to the discussion of the multi electron dissociative ionization (MEDI) of molecules in an intense laser field.

Direct ionization [60, 61]: In this case the molecules are ionized near R_e without any, or with very little, stretching of their internuclear distance during their breakup (see Fig. 1.2(a)) *i.e.* ionization occurs near $R \simeq R_e$. The transition is almost vertical, hence the nuclei can be treated as frozen. If the molecular potentials are repulsive as is typically the case for states of multiply ionized molecules, the resulting KER will usually be high.

Charge-resonance enhanced ionization (CREI) [32, 62]: In order to explain the measured KER in ionization that is lower than expected from the Coulomb explosion at R_e, an en-

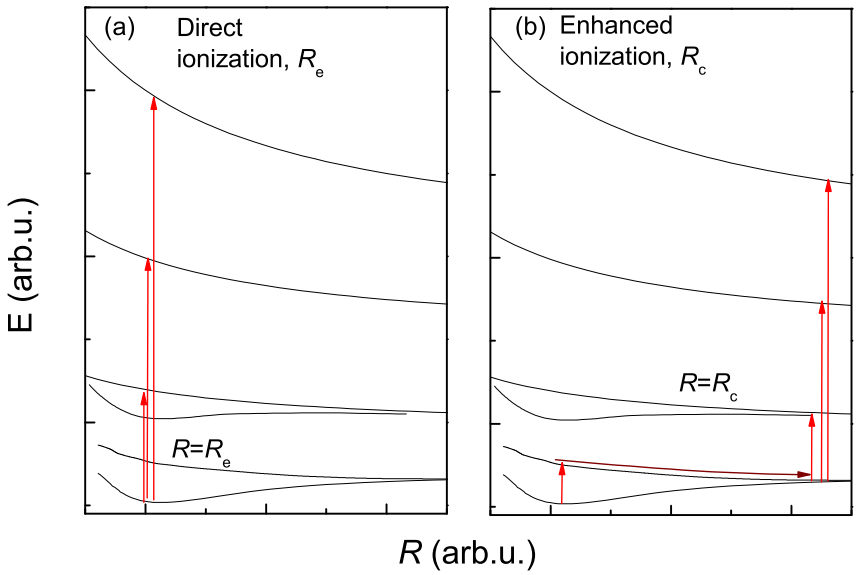

Figure 1.2: *Schematic diagrams illustrating the different mechanisms for the multiple ionization of a typical molecule, AB^+, in an intense laser field (a) direct ionization and (b) enhanced ionization. For a discussion of the mechanisms refer to the text.*

hanced ionization mechanism has been suggested [32, 62]. This mechanism considers the nuclear motion and has been explained in terms of the stretching of the molecule prior to ionization such that the electron localizes on one of the two nuclear centers. Hence, the ionization will be enhanced once the electron is localized – herein we refer to this process as enhanced ionization. This leads to the ionization of molecules at some R that is greater than R_e and is called the critical internuclear distance, R_c, (see Fig. 1.2(b)).

The mechanisms presented here will be used in the following chapters in order to explain the results of our measurements on laser-induced breakup of molecules. Before going into these results, we introduce the experimental method developed and used to produce them.

Chapter 2

Experimental Method

2.1 Introduction

Imaging of molecular fragments is a powerful method for the study of molecular breakup. This allows one to understand the dynamics of the breakup process. We use a coincidence three-dimensional (3D) momentum imaging technique to study laser induced fragmentation of molecular ions. Details on this experimental method are discussed here. The experimental arrangement consists of four major components: a pulsed laser, a direct current ion beam, an interaction region, and a coincidence 3D momentum imaging setup shown schematically in Fig. 2.1.

The coincidence 3D momentum imaging setup, developed previously by our group [12, 63–65], can be used (i) without applying any static electric field, referred to, in here, as field free imaging (FFI) or (ii) applying a static electric field along the ion beam direction using a spectrometer, referred to as longitudinal field imaging (LFI). The very basic characteristics of these imaging techniques are summarized in Table 2.1 and described in the next section. These methods have a limitation on the study of the low energy breakup of molecules.

This limitation has been removed by developing a couple of newer versions of our coincidence 3D momentum imaging method. In one case we use a static electric field in the transverse direction to the ion beam using an electrostatic deflector, referred to as transverse field imaging (TFI). In the other case we apply longitudinal and transverse fields in

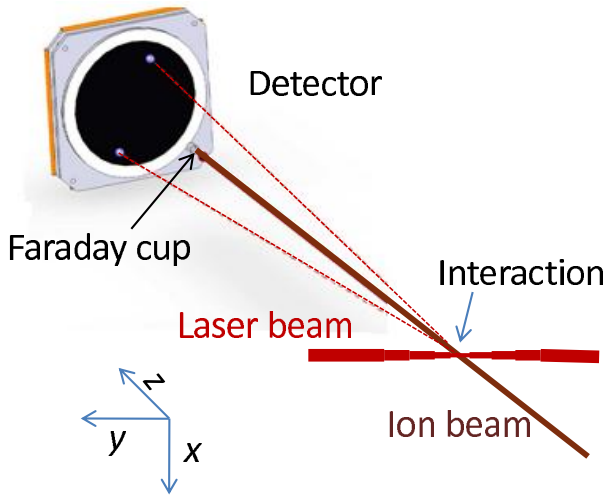

Figure 2.1: *Schematics of the experimental apparatus with four components: laser beam, ion beam, interaction region, and coincidence 3D momentum imaging setup. The ion beam is along the z direction and the laser propagation is along the y direction.*

Table 2.1: *Summary of different imaging methods possible with our experimental apparatus.*

Method	Applied static field	Field direction	Fragment separation	Distortions	Low KER measurements
FFI	No	–	Limited	No	No
LFI	Spectrometer	Along z	In time	Yes	No
TFI	Deflector	Along y	In space	Yes	Limited
LATFI	Spectrometer and deflector	Along z and y	Both in time and space	Yes	Yes

combination using a spectrometer and a deflector, respectively, referred to as longitudinal and transverse field imaging (LATFI). First, we discuss briefly the previous methods, *i.e.* FFI and LFI. Then we present details of the upgraded techniques, *i.e.* TFI and LATFI, that have been developed as part of this project for the measurements of very low KER (down to nearly 0 eV). In addition, these new methods allow the study of dissociative and non-dissociative single ionization of the many-electron homonuclear and heteronuclear (nearly mass symmetric) molecular ion beams. Furthermore, the non-dissociative ionization studies can be extended to atomic ion beams.

Discussion of the imaging techniques is followed by a few examples in order to demonstrate the capabilities of the LATFI method. Also, the comparison between the measurements from the LFI and the LATFI methods are discussed. Other possible aspects of the LATFI techniques that are not feasible with the LFI method for the study of interactions between an intense laser field and molecules are outlined.

For completeness, a brief description of the other components of the experimental apparatus that are similar for all the imaging techniques possible with our experimental method is presented.

2.2 Coincidence 3D momentum imaging technique

Time of flight (TOF) mass spectrometry [66, 67], two-dimensional momentum imaging [68, 69], and coincidence three-dimensional momentum imaging [12, 63, 64] techniques have been used to study the interaction between an intense laser and molecular-ion targets. In addition, there are different kinds of techniques developed that are in use by other groups for the study of the interaction of an intense laser and neutral gas molecular targets, e.g. field free imaging [70, 71], TOF mass spectrometry [53, 72–75], covariance mapping [76], mass-resolved momentum imaging (MRMI) [77], cold-target recoil ion momentum spectroscopy (COLTRIMS) [78], and velocity-map imaging (VMI) [79]. Here we focus on the method developed previously by our group, *i.e.* coincidence 3D momentum imaging and its working principles. The basics of the experimental arrangement are shown schematically in Fig. 2.1.

The laser used in our measurements is a Ti:Sapphire system that provides linearly polarized short pulses [30 fs full width at half maximum (FWHM) in intensity], 2 mJ energy per pulse at 2 kHz repetition rate with a fundamental wavelength of about 790 nm. Ultrashort (few cycle) pulses are generated, when needed, by compressing the regular amplified pulses using a neon-filled hollow-core fiber and chirped mirror arrangement to achieve $\leq$10 fs (FWHM) duration [80]. The laser beam is transported to the ion beam setup and focused onto the ion beam target at the interaction region using an f=203 mm off-axis parabolic

mirror.

The molecular ion targets in our studies are produced by electron impact ionization of gas molecules in an ion source. The electron bombardment produces a plasma in the source and the ions are then extracted. Using the following steps we get the ion beam with the desired mass-to-charge ratio and beam energy. These ions are (a) accelerated with a voltage of up to 30 kV, (b) analyzed according to their momentum-to-charge ratio using a magnetic field, (c) steered and focused using electrostatic ion optics, and (d) collimated using a couple of four-jaw slits.

The interaction region is defined as the point where the focused laser beam crosses the ion beam. The breakup fragments are detected with a time- and position-sensitive detector. Any undissociated primary ion beam is collected in a small Faraday cup kept in front of the detector to monitor beam current and prevent the detector from being hit by the ion beam. Using the laser intensity at the interaction as a control parameter we study the breakup of the molecules. In our experiments the laser intensity at the interaction point is varied either by using neutral density filters [81] or by moving the position of the focus along the laser propagation direction [82], called intensity difference scanning (IDS).

As mentioned earlier in Section 2.1 our coincidence 3D momentum imaging setup can be used in different conditions depending upon the system under study (see Table 2.1). In all cases we separate each fragmentation channel from the others, and then get the momenta of each fragment using the measured TOF and position of the hit of the fragment on the detector. In some cases assumptions are needed, e.g. in the FFI method dissociation is separated from ionization channels using the energy of the breakup. It is believed that the KER from dissociation is lower than from ionization. Calculations of KER and angular distributions are briefly described here and detailed in Appendix A for each of these methods. The angular distribution is expressed in terms of the angles ϕ and θ (azimuthal and polar angles). In particular θ is defined as the angle between the laser polarization and the molecular dissociation axis. The molecular breakup is symmetrical about the azimuthal

angle ϕ and in some circumstances we use this fact to reconstruct losses in the measured data. Each of the imaging methods we use has some advantages and disadvantages that are discussed below in the corresponding subsections.

2.2.1 Field free imaging (FFI)

Field free imaging (FFI) is the most commonly used beam fragment imaging technique [70, 71]. It can be used in our experimental apparatus without applying any static electric field. The fragments from the breakup will travel to the detector with TOF similar to each other. Their relative position on the detector and TOF difference is determined by the breakup momentum in the transverse and longitudinal directions, respectively.

Here is a brief description of how we get the momentum, KER, and angular distribution from the measured time and position of the fragments. We begin with the calculation of momentum along the x direction.

x direction

The displacement equation along the x direction for the first fragment to reach the detector is

$$x_1 - x_{0_i} = (v_{0x_i} + v_{1x})t_1 \tag{2.1}$$

where x_1 is the measured position, t_1 is the measured time, v_{1x} is the dissociation velocity component, v_{0x_i} is the velocity component of a specific molecular ion at the dissociation point, and x_{0_i} is the dissociation point of a specific molecular ion. In a similar way, for the second fragment we can write

$$x_2 - x_{0_i} = (v_{0x_i} + v_{2x})t_2 \tag{2.2}$$

where the parameters have similar meanings as in equation (2.1) except they are for the second particle as denoted by the subscript 2. We also use momentum conservation in the center of mass (CM) system

$$m_1 v_{1x} + m_2 v_{2x} = 0 \tag{2.3}$$

where m_1 and m_2 are the masses of the first and second fragments, respectively. Here we have three equations and four unknowns — $x_{0_i}, v_{0x_i}, v_{1x}$, and v_{2x} that we can solve with an assumption.

We choose to use $\overline{x}_{0_i}$ *i.e.* the average of the x_{0_i} distribution computed for all events and denote as $x_0{=}\overline{x}_{0_i}$. This assumption is valid as long as the size of the laser beam at the interaction is smaller than the ion beam. This is one of the reasons we do not use the zIDS method (*i.e.* IDS by moving the position of the laser focus), for very low laser intensities, as the laser beam becomes comparable to or bigger than the ion beam. We compute v_{0x_i} for each event such that we eliminate the possible broadening effects in the energy resolution of our system from the spread in the initial beam energy.

Solving equations (2.1), (2.2), (2.3) and simplifying for v_{1x} gives (details in Appendix A)

$$v_{1x} = \frac{x_1 - x_2 + v_{0x_i}(t_2 - t_1)}{t_1 + \beta t_2} \tag{2.4}$$

where $\beta \equiv \beta_{12} = \frac{m_1}{m_2}$ is the mass ratio of the fragments. The momentum component along the x direction is $p_{1x} = m_1 v_{1x}$.

For the FFI method the parameters along the y direction are the same as along the x direction and hence are skipped here. However, we write these equations explicitly for the other methods so that any modifications needed are followed easily.

z direction

The velocity components along the z direction are calculated using the TOF of the fragments. The TOFs of the first and second fragment to reach the detector are given by

$$t_1 = \frac{d - z_i}{v_{0z_i} + v_{1z}} = \frac{d(1 - z_i'')}{v_{0z_i} + v_{1z}} \tag{2.5}$$

$$t_2 = \frac{d - z_i}{v_{0z_i} + v_{2z}} = \frac{d(1 - z_i'')}{v_{0z_i} + v_{2z}}, \tag{2.6}$$

where d is the distance from the interaction region to the detector, z_i is the initial point of the dissociation with respect to the laser and ion beam crossing, $z_i'' = \frac{z_i}{d}$ is the scaled initial

point of dissociation, v_{0z_i} is the velocity of a specific molecular ion at the dissociation point in the z direction, and v_{1z} and v_{2z} are the dissociation velocities of the first and the second fragments along the z direction, respectively. Conservation of momentum implies

$$m_1 v_{1z} + m_2 v_{2z} = 0. \tag{2.7}$$

Again, we have four unknowns — z_i, v_{0z_i}, v_{1z}, and v_{2z}, and we replace as before z_i with its average value to solve these equations.

Solving for v_{1z}, we can write

$$v_{1z} = \frac{1}{1+\beta}\left(\frac{d(1-z_i'')}{t_1} - \frac{d(1-z_i'')}{t_2}\right) \cong \frac{1}{1+\beta}\left(\frac{d}{t_1} - \frac{d}{t_2}\right) \tag{2.8}$$

where the right side is an approximate expression for $z_i'' \ll 1$ which is typically the case for our measurements. Finally, the momentum along the z direction, denoted by p_{1z}, is given by $p_{1z} = m_1 v_{1z}$.

Now that we have all three components of the momentum, we can get the KER and the angle θ as described below.

KER and cosθ

The KER is given by

$$\text{KER} = \frac{1}{2}m_1 v_1^2 + \frac{1}{2}m_2 v_2^2 = \frac{1}{2\mu}m_1^2 v_1^2 = \frac{p_1^2}{2\mu} \tag{2.9}$$

where $v_1^2 = v_{1x}^2 + v_{1y}^2 + v_{1z}^2$ and μ is the reduced mass of the molecule defined as $\frac{1}{\mu} = \frac{1}{m_1} + \frac{1}{m_2}$.

As the angle θ is defined with respect to the laser polarization, we use a transformation from lab coordinates (x, y, z) to laser coordinates (i, j, k). The laser polarization is along the k direction and $\hat{j}$ is parallel to $\hat{y}$. Then cosθ is

$$cos\theta = \frac{p_{1k}}{\sqrt{p_{1i}^2 + p_{1j}^2 + p_{1k}^2}} = \frac{p_{1k}}{\sqrt{2\mu \text{KER}}} \tag{2.10}$$

In this FFI method, there is no external field and hence no distortions. This means that the resolution is good. However, we can not separate ions from neutrals in this

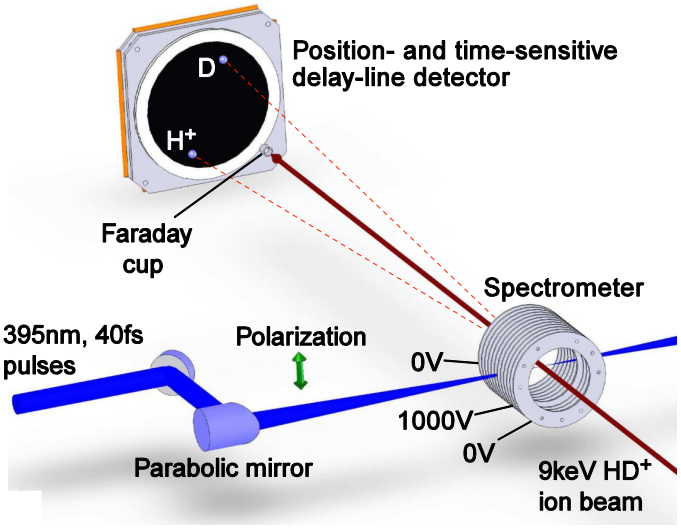

Figure 2.2: *Schematic view of the coincidence 3D momentum imaging for LFI. The static electric field of the spectrometer along the ion beam direction allows the separation of the ions and neutrals by their flight time to the detector. Figure adapted from Ref. [37].*

method, which is not a suitable condition for the study of the laser induced fragmentation of molecules. Because in an intense laser field we see ionization in addition to dissociation, their separation from one another is highly desired. Also, for the low energy breakup, the fragments are captured in the Faraday cup. Due to these reasons we do not use FFI for most of our studies.

Let us move to the imaging method that we have used extensively for previous studies, *i.e.* the LFI. This method allows us to separate different breakup channels and get the kinematics of the molecular fragmentation as discussed briefly below.

2.2.2 Longitudinal field imaging (LFI)

Longitudinal field imaging (LFI) is the experimental method that our group has developed for coincidence 3D momentum imaging for the study of crossed laser and molecular-ion beam targets [12, 63–65]. Details of this method are given in Ref. [65] and hence only a brief discussion is presented here.

The experimental setup consists of a TOF spectrometer that has a series of concentric

rings (see details in Appendix B). The interaction region is within the spectrometer as shown in Fig. 2.2. The uniform static electric field of the spectrometer is along the ion beam direction (z) and hence the name longitudinal field imaging (LFI). This field allows the separation of the fragments by their flight time to the detector, that is according to their mass-to-charge ratio as charged particles are accelerated (or decelerated) with respect to the neutrals. The breakup energy in the transverse direction to the ion beam velocity separates the fragments in position on the detector, as shown schematically in Fig. 2.2 for the dissociation of an HD^+ beam. From time and position information we get the kinematics of the breakup as discussed in Appendix A. The only difference compared to the FFI is along the z direction as we apply the static electric field with the spectrometer, so here we discuss only the z component of the momentum and skip the x and y.

The TOF of ions and neutrals are given by

$$t_1 = \frac{2d_1}{v_{0z_i}}\frac{1}{\eta_1}\left[\sqrt{(1+u_{1z})^2+\eta_1(1-z_i')}-(1+u_{1z})\right]+\frac{d_2}{v_{0z_i}}\frac{1}{\sqrt{(1+u_{1z})^2+\eta_1(1-z_i')}} \tag{2.11}$$

and

$$t_2 = \frac{d(1-z_i'')}{v_{0z_i}(1-\beta u_{1z})} \tag{2.12}$$

respectively, where d_1 is the length of the region within the field of the spectrometer and d_2 is the length of the field-free region such that the total length from the interaction region to the detector is $d = d_1 + d_2$, $z_i' = \frac{z_i}{d_1}$, and $z_i'' = \frac{z_i}{d}$ is the scaled initial position of the dissociation point. Also, we define $u_{1z} = \frac{v_{1z}}{v_{0z_i}}$ as the scaled dissociation velocity along the z direction where v_{1z} is the dissociation velocity of the first fragment along the z direction and v_{0z_i} is the z-velocity component of a specific molecular ion at the dissociation point. The dimensionless parameter η_1 (also called scaled energy) is defined as $\frac{0.8\times q\times V_s}{E_1}$ with q the charge of the fragment, E_1 its energy at the interaction point, and V_s the voltage applied to the spectrometer relative to ground. We solve these equations numerically for v_{1z} after substituting equation (2.12) into equation (2.11).

The momentum component along the z-direction is $p_{1z} = m_1 v_{1z}$. The KER and the angle can be calculated as mentioned before.

Using this technique we have studied the molecular fragmentation dynamics of diatomic and simple polyatomic molecular ions in intense laser fields that include the benchmark system H_2^+ and its isotopes [30, 37, 63, 81], the smallest polyatomic H_3^+ [83], and a few many electron homo- and hetero-nuclear diatomic molecules N_2^+ [38, 84], O_2^+ [84, 85], ND^+ [86], CO^+, and NO^+ [84], CO^{2+} [87], N_2O^+, and others.

For the energetic breakup of molecules we can measure dissociation as well as single and multiple ionization, e.g. Ref.[38, 84]. However, this method is limited to measurements of KER above some minimum value, of the order of 0.1 eV, for the systems we have studied. The reason is fragments with low transverse velocity could not be separated from the primary beam and hence fall into the small Faraday cup that is being used to collect the primary beam and also protect the imaging detector.

This problem of low KER measurement is solved by upgrading the experimental setup while preserving the coincidence nature of the measurements. In the upgraded setup we apply a static electric field in the transverse direction to the ion beam, and the fragments are separated in their position instead of their TOF. More importantly, this transverse deflection separates low KER fragments from the ion beam. This method is presented below in detail.

2.2.3 Transverse field imaging (TFI)

The main idea in this case is to separate the breakup fragments in position instead of in time. We keep the interaction region field free and use an electrostatic deflector in between the interaction region and the detector as shown schematically in Fig. 2.3. The uniform static electric field of the deflector is transverse to the ion beam direction and hence the name transverse field imaging (TFI).

This electrostatic deflector is a parallel plate deflector with two plates separated by D =30 mm and has additional plates in between to reduce the fringe field. A brief description of its geometry is presented here while the details are given in Appendix B. The metallic

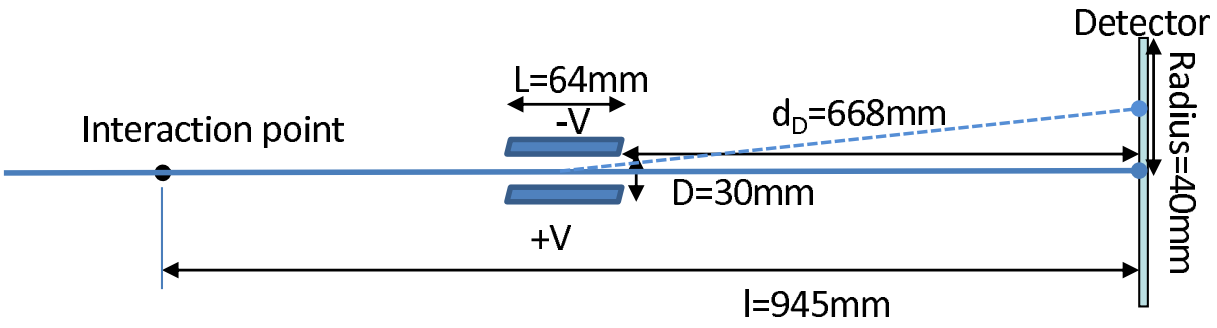

Figure 2.3: *Schematics of a setup for TFI method. The interaction region is field free and the static field of the deflector separates the fragments in position on the detector.*

plates of thickness 1 mm are separated from each other by 4 mm. The length (L) of the deflector along the ion beam direction is 64 mm, and the vertical height (H) is 114 mm. The height of the deflector is sufficient such that the fringe field effects are negligible in the vertical direction. The ions are deflected in the same direction as the laser propagation in the current setup, *i.e.* along y, as we are more flexible in this direction to move the Faraday cup to capture the deflected primary beam.

The fragments are then separated in their position on the detector according to their energy-to-charge ratio. However, the time separation between the fragments only depends on the breakup energy along the ion beam direction. Higher breakup energy provides better time separation. We can set the laser polarization along the ion beam direction in order to increase the time separation between the fragments if the breakup is along the laser polarization.

Separation of channels

Distinguishing the breakup channels and the particles is a challenge in this method because ions with the same energy-to-charge ratio coming from the dissociation and ionization have similar TOF and position on the detector. Separation of the channels by using this method is briefly discussed here and in detail in Appendix C. We separate dissociation and ionization

by using the center of mass (CM) calculated from the measured position and time of the fragments. We find the CM along the x direction, denoted by X_{CM}, from the measured position as defined by

$$X_{CM_{12}}(t) = \frac{m_1 x_1(t) + m_2 x_2(t)}{m_1 + m_2} \tag{2.13}$$

$$X_{CM_{21}}(t) = \frac{m_2 x_1(t) + m_1 x_2(t)}{m_1 + m_2} \tag{2.14}$$

Here we have to define CMs in two different ways as we do not know the order of the hits. As indicated in the equations, each CM should be calculated using positions measured at the same time. In the TFI method, however, t_1 and t_2 are nearly equal and allow us to approximate the CM by using the measured x_1 and x_2, even though they are technically measured at different times. The CMs of dissociation are around the position of the deflected primary beam and differ from the ionization CMs that are around the H^+ distribution, as shown in Fig. 2.4. The CM coordinates along the y direction are defined in a way similar to that for the x direction. And for the T_{CM} we use the measured time of flight of the fragments *i.e.*

$$T_{CM_{12}} = \frac{m_1 t_1 + m_2 t_2}{m_1 + m_2} \tag{2.15}$$

$$T_{CM_{21}} = \frac{m_1 t_2 + m_2 t_1}{m_1 + m_2}. \tag{2.16}$$

Both versions of X_{CM} and Y_{CM} are plotted in a density plot, shown in Fig. 2.4 (left). From that plot, one can distinguish the ionization CM from the dissociation CM. The ionization and dissociation CMs have almost same x coordinate as there is no deflection field in that direction and have different y coordinates due to the deflection along y. From the plot of the T_{CM} (not shown here), one can find the value of T_{CM} to be similar for both dissociation and ionization as there is no static electric field along the z direction.

Next we find the order of hits. In the case of heteronuclear diatomic molecules we have two dissociation channels e.g. $AB^+ \rightarrow A^+ + B$ or $A + B^+$ and their separation is crucial as there might be interesting differences between the two channels. In order to know the order of hits we find the mass ratio ($\beta = \frac{m_1}{m_2}$) using CMs and the measured time and position.

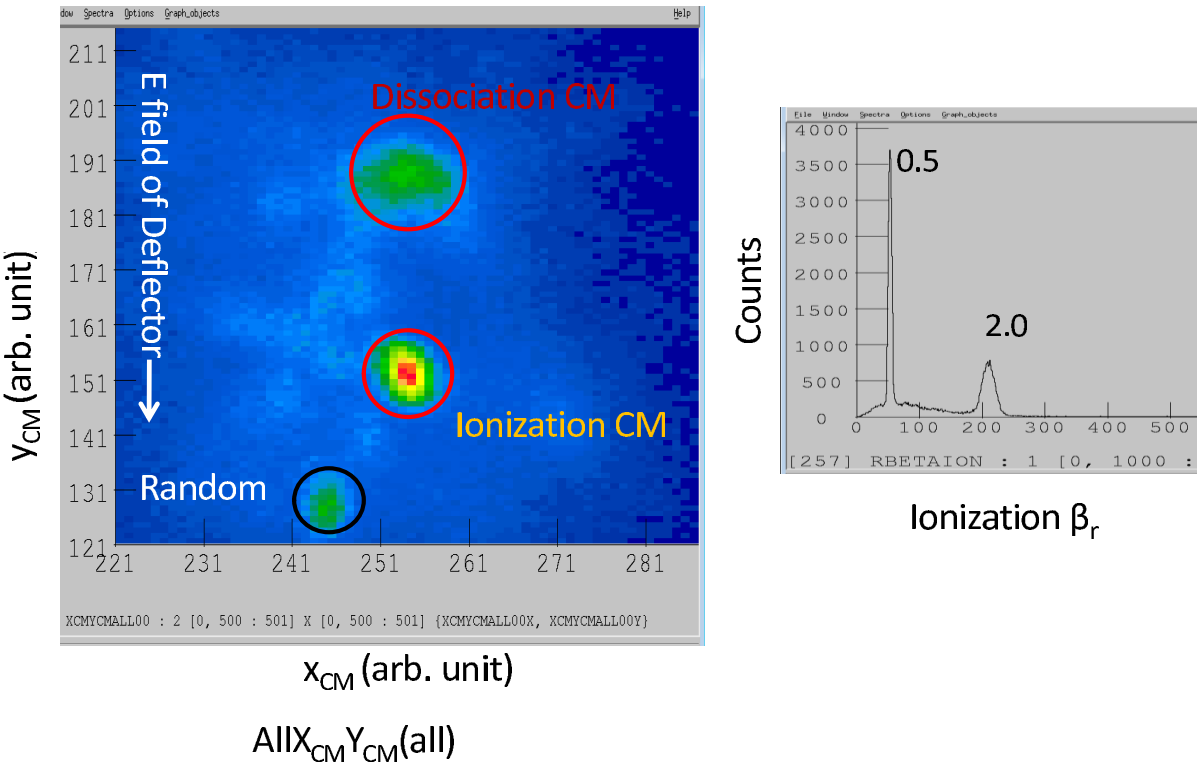

Figure 2.4: *Plots of (left) $X_{CM}\,Y_{CM}$ and (right) β_r in the TFI measurements for heteronuclear HD^+ molecule. Figures are taken from the screen image of the data analysis programm, called SpecTcl. The β_r plot is scaled up by 100, so 50 is for β=0.5.*

Along x direction, we can write $m_1 v_{1x} = -m_2 v_{2x}$, where v_{1x} and v_{2x} are the dissociation velocities of the fragments. Since there is no field along this direction both fragments will have similar TOFs which results in $m_1 x'_1 = -m_2 x'_2$ (approximately by neglecting the small uncertainty in the initial position) where x'_1 and x'_2 are in the CM coordinate system. This in turn suggests that the mass ratio can be evaluated from the measured positions, e.g. from measurements along x direction we can write

$$\beta_x = \sqrt{\frac{(x_2 - X_{CM})^2}{(x_1 - X_{CM})^2}} \tag{2.17}$$

By selecting the dissociation and ionization CMs we can find the mass ratio (β) for corresponding channels. Instead, we find that defining β using all three coordinates is better, so

we use β_r defined as

$$\beta_r = \sqrt{\frac{(x_2 - X_{CM})^2 + (y_2 - Y_{CM})^2 + (v_{0z}(t_2 - T_{CM}))^2}{(x_1 - X_{CM})^2 + (y_1 - Y_{CM})^2 + (v_{0z}(t_1 - T_{CM}))^2}}, \tag{2.18}$$

shown in Fig. 2.4 (right).

We calculate the difference $d_y = \beta y_1 - y_2$ and sum $s_y = \beta y_1 + y_2$) in y for all possible combinations. Using these parameters we distinguish the hits with the correct order in a given channel as shown in Fig. 2.5. Once the channels are separated and selected properly we get the momenta of the fragments as described briefly below (see details in Appendix A).

In this TFI method, the parameters along the x and z directions are similar to the FFI case (Section 2.2.1) as the uniform field acts only along the y direction. So here we compute the momentum component along the y direction, corrected for the fringe field effects as explained in Appendix B.

The displacement equation for the first particle along the y direction can be written as

$$y_1 - y_{0_i} = (v_{0y_i} + v_{1y})t_1 + G_d \frac{\eta_{D_1}}{(1 + u_{1z})^2} \tag{2.19}$$

where y_1 is the measured position, t_1 is the measured time, v_{1y} is the dissociation velocity of the first particle in the y direction, v_{0y_i} is the velocity of a specific molecular ion at the dissociation point along the y direction, and y_{0_i} is the point of dissociation. Also u_{1z} is the scaled dissociation velocity along the z direction, given by $u_{1z} = \frac{v_{1z}}{v_{0z_i}}$, where v_{1z} is the dissociation velocity of the first fragment along the z direction and v_{0z_i} is the velocity of a specific molecular ion at the dissociation point in the z direction. $\eta_{D_1} = \frac{q_1 V_d}{E_1}$ with q_1 the charge of the fragment, V_d the deflector voltage, and the energy of the fragment $E_1 = \frac{1}{2} m_1 v_{0z_i}^2$. The geometry factor for the electrostatic deflector is $G_d = \frac{1}{2}\frac{L}{D}\left(d_D + \frac{L}{2}\right)$, where the length of the deflector is L=64 mm, the separation between the two outermost parallel plates D=30 mm, and the distance from the deflector exit to the detector is d_D=668 mm. So, $G_d = 746.7$ mm. Using SIMION simulations (see Appendix B for details) we found that a scaling correction factor for G_d of 1.2 is required to match this ideal deflector equation to the real one. Hence we use $G_d = 1.2 \times 746.67$ mm=896 mm in our imaging analysis.

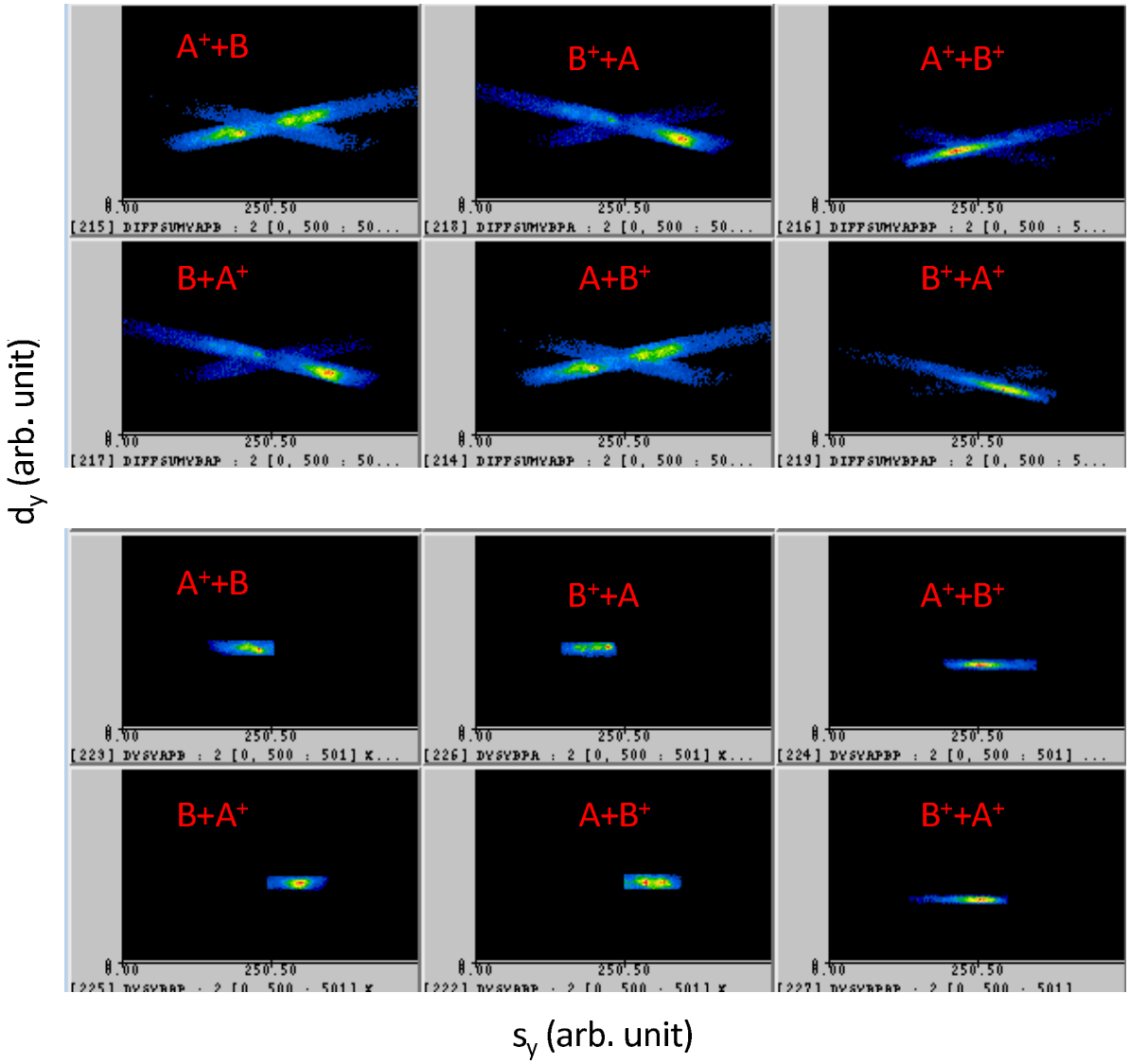

Figure 2.5: *Plots of difference and sum of the measured y values of the two hits, upper pannels for uncorrected mass ratio and the lower panels with correct mass ratio.*

In a similar way, for the second fragment we can write

$$y_2 - y_{0_i} = (v_{0y_i} + v_{2y})t_2 + G_d \frac{\eta_{D_2}}{(1+u_{2z})^2} \tag{2.20}$$

where the parameters have similar meaning as in equation (2.19) but for the second fragment as denoted by the subscript 2.

Subtracting equation (2.20) from equation (2.19), we get $y_1 - y_2 = v_{0y_i}(t_1 - t_2) + v_{1y}t_1 -$

$v_{2y}t_2 + G_d\left(\frac{\eta_{D_1}}{(1+u_{1z})^2} - \frac{\eta_{D_2}}{(1+u_{2z})^2}\right)$. Using momentum conservation along y (*i.e.* $m_1 v_{1y} = -m_2 v_{2y}$) and solving for v_{1y} yields

$$v_{1y} = \frac{y_1 - y_2 + v_{0y_i}(t_2 - t_1) - G_d\left(\frac{\eta_{D_1}}{(1+u_{1z})^2} - \frac{\eta_{D_2}}{(1+u_{2z})^2}\right)}{t_1 + \beta t_2} \tag{2.21}$$

For two body dissociation, the second particle is a neutral and hence q_2 is zero, *i.e.* $\eta_{D_2} = 0$. Once the velocity is found we get the momentum using $p_{1y} = m_1 v_{1y}$.

For the ionization events we have enough time separation between the fragments when the laser polarization is pointing along the ion-beam direction. However, for the dissociation events with very low break up energy the time separation is not sufficient. In this case, one can use the position signals and reconstruct the timing information of the second hit. Instead, it is simpler to use the method with both longitudinal and transverse fields for the measurements of low energy breakup fragments. This method is discussed in the next subsection.

One drawback of the TFI method is that the effective detector size is reduced significantly to about half. In the absence of the transverse field the primary ion beam (*i.e.* the Faraday cup position) is around the center of the detector. With the transverse field all the positive ions are deflected in one direction leaving the other half of the detector redundant. So, for studies ranging from very low energy breakup in dissociation to high energy breakup in multiple ionization, we have to decide which method to use and what strength of the electrostatic field to provide.

The vacuum requirements for measurements in the TFI mode are more stringent. The fraction of the primary ion beam that gets neutralized by collision with the background gas prior to the deflector does hit the detector in this case while it is blocked by the Faraday cup in the absence of a transverse field.

2.2.4 Longitudinal and transverse field imaging (LATFI)

As pointed out in the previous subsection, the time separation between fragments with very low breakup energy is not sufficient in the TFI method, and therefore the time signal of

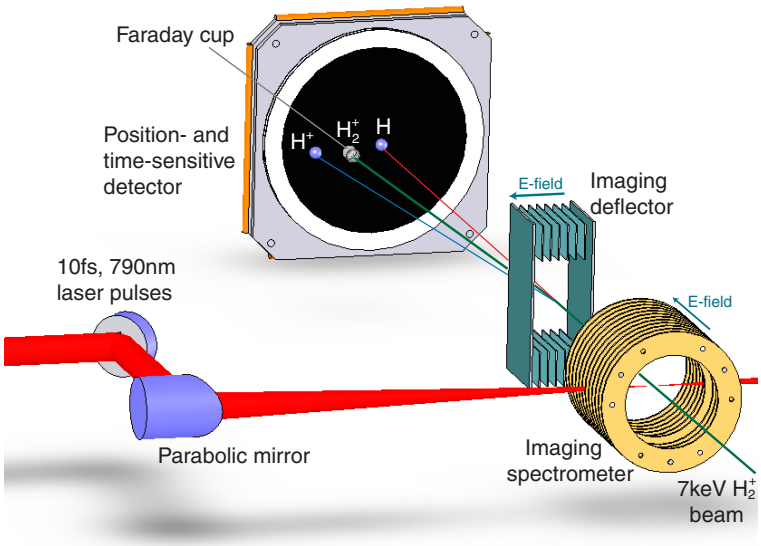

Figure 2.6: *Schematic view of the coincidence 3D momentum imaging setup with the LATFI method using both spectrometer and deflector. This has been used to measure KER distributions down to KER≅0 eV (sub ∼1 meV) of molecular breakup. The neutrals hit the detector where the primary ion beam would hit in the absence of the deflector field. The primary beam is deflected and captured in a Faraday cup. Fragment ions are deflected further out compared to the primary ion beam. Figure taken from Ref. [88].*

the second particle is lost. Also in the LFI method these very low energy fragments are lost in the Faraday cup. To solve this problem and measure KER down to nearly 0 eV, we have combined the best of the LFI and TFI methods. We use both the longitudinal and transverse static electric fields together, hence the name longitudinal and transverse field imaging (LATFI). The longitudinal field, provided by the spectrometer (discussed in Section 2.2.2), allows the separation of fragments in time, and the transverse field, provided by the deflector (discussed in Section 2.2.3), allows the space separation of the fragments as discussed below.

This method still preserves the coincidence nature of the measurement. The interaction region is within the spectrometer as in the case of the LFI setup [63, 64], as illustrated in Fig. 2.6 for a H_2^+ beam. The fragments from the breakup travel toward the time- and position-sensitive detector. The remaining undissociated ion beam is collected in an off-axis Faraday cup to prevent damage of the detector and to monitor the beam current.

The basic idea is that the neutral fragments hit the detector where the primary ion beam would hit in the absence of the deflector field. The primary ion beam is deflected by the transverse field toward a small off-axis Faraday cup. The fragment ions with smaller energy-to-charge ratio than the primary beam are deflected further out. Hence the fragments including the ones with very low KER are separated in their position on the detector. The timing separation is provided with the longitudinal static electric field of the spectrometer as in Section 2.2.2.

Using the TOF and position of the fragments measured in coincidence, we reconstruct the full 3D momentum distribution of both fragments, thus retrieving the angular and KER distributions of dissociation and ionization — for the entire range of KER.

The separation of channels in this method is similar to the LFI method. However, the calculation of momentum components is a combination of all the methods discussed in previous subsections and hence is only briefly mentioned here.

x direction

As there is no field in this direction, the FFI expressions (Section 2.2.1) can be used, *i.e.* v_{1x} is given by equation (2.4).

z direction

We have the spectrometer providing longitudinal field in this direction so we use the expressions from the LFI method (Section 2.2.2). Since some of the parameters (like v_{1z} and v_{0z_i}) related to this direction are needed for the calculation of momentum in the y direction, these calculations should precede the calculations in y. Small deviations of the TOF due to the deflector fringe fields are corrected for.

y direction

The transverse field is provided by the deflector, so the TFI equations can be used for this direction *i.e.* v_{1y} is given by a modified version of equation (2.21). This is because an ion

entering the deflector field region has a velocity, denoted by v_{0z_d}, which is different from its velocity (v_{0z_i}) at the interaction. We can write $\frac{1}{2}mv_{0zd}^2 = \frac{1}{2}mv_{0z_i}^2 + qV(z_i)$, where m and q are the mass and charge of the particle and $V(z_i)$ is the voltage at the interaction point within the spectrometer. Then we have,

$$v_{0z_d} = \sqrt{\frac{2qV(z_i)}{m} + v_{0z_i}^2}. \tag{2.22}$$

The expression for the modified v_{1y} is given in Appendix A.4. Since this imaging method is a combination of the other methods, the distortions are from the fringe fields of the spectrometer and the deflector. The effective size of the detector is still smaller than in LFI method and the high rate of the neutrals due to poor vacuum of the system also affects the measurements, as for the TFI method (in Section 2.2.3).

Next, we discuss a few examples of the low KER measurements with the LATFI setup and then its capabilities for other processes.

2.3 Measurements with LATFI method

We have measured low KER in the dissociation of molecules using the LATFI method. This technique has also been implemented for the studies of mass asymmetric molecules. We discuss the limit on the mass ratio of the fragments that can be measured for low-energy breakup. In addition, the LATFI method allows measurements of non-dissociative ionization of singly charged molecular ion targets in the laser field. We begin with the low KER measurements.

2.3.1 Measurements of low KER

In order to demonstrate the ability to measure low KER all the way down to almost zero, limited only by the detection resolution of $\sim 1\,\text{meV}$, we present the results for the dissociation of O_2^+ and H_2^+ in intense short pulses at 790 nm. In the case of O_2^+ dissociation a large peak at very low KER is observed. In the case of H_2^+ dissociation, a weaker low-KER peak compared to a strong bond softening peak around 0.8 eV has been observed.

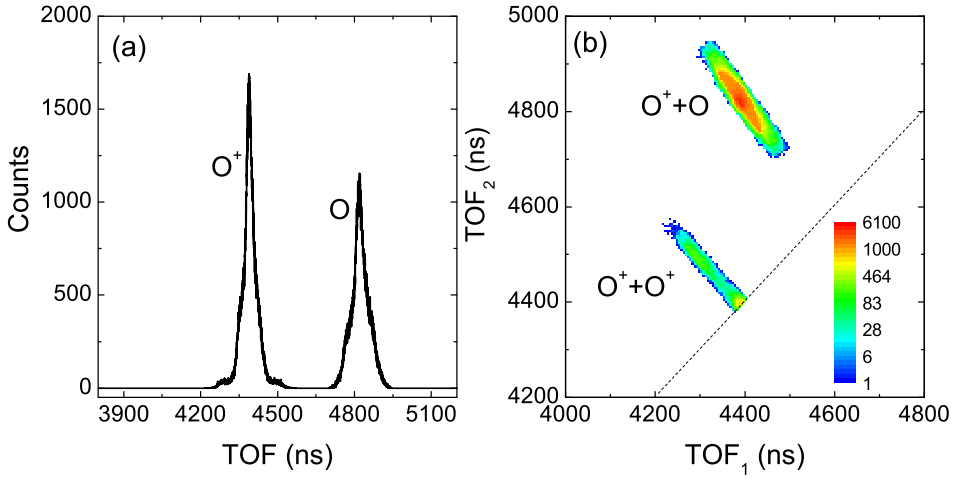

Figure 2.7: *(a) Measured TOF spectrum for the dissociation fragments of O_2^+ using 40 fs 790 nm laser pulses at 4×10^{15} W/cm^2. The O^+ ions are separated from the O atoms in their flight time to the detector. (b) Coincidence TOF density plot. Note that the ionization and dissociation channels are cleanly separated. The dashed line indicates the loci TOF_1=TOF_2. The data displayed in this picture is plotted after applying momentum conservation to the breakup.*

2.3.2 Dissociation of O_2^+

As a test of this newly developed LATFI method we have measured the dissociation of an O_2^+ beam using 40 fs, 790 nm laser pulses. The static electric field of the spectrometer separates ionic and neutral fragments according to their mass-to-charge ratio by their TOF to the detector as exemplified in Fig. 2.7(a). We have also shown a coincidence TOF plot in Fig. 2.7(b), in which the ionization channel (O^++O^+) is nicely separated from the dissociation channel (O^++O). Also, the density plot suggests that the yield of dissociation is much higher than that of ionization.

The addition of the transverse static electric field of the deflector now separates the positive ion and neutral fragments also in position on the detector, as shown in Fig. 2.8. More importantly, it pulls the low-KER fragments out of the primary ion beam and the Faraday cup. These low-KER fragments are distributed around the center of each spot, *i.e.* the O^+ and O spots. The distribution of the O atoms is centered at the point where the

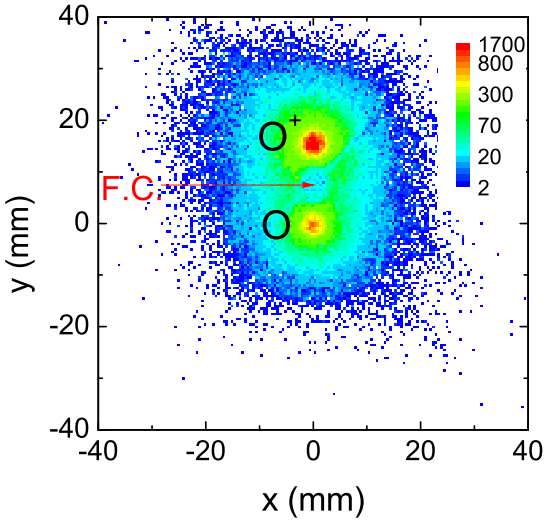

Figure 2.8: *Measured position of the fragments from the dissociation of O_2^+ using 40 fs 790 nm laser pulses at 4×10^{15} W/cm^2. The static field of the imaging deflector was such that the deflection of the charged particles was along the positive y direction. The centers of the position distribution of the O^+ and O are nicely separated from one another and also from the Faraday cup (F.C.) shadow. The data displayed in this picture are plotted after applying momentum conservation to the breakup.*

primary ion beam would hit in the absence of the deflector field. The deflected primary ion beam is at the position of the Faraday cup. The Faraday cup itself and its holder casts a shadow that is visible in Fig. 2.8. This has a small effect on losing counts in the higher energy breakup as it cuts away from the center of the position distribution. In fact this loss of events can be recovered by using the symmetry around the laser polarization, aligned along the ion beam axis in this case, *i.e.* along the azimuthal angle. The O^+ ions are deflected further out than the O_2^+ beam. The distribution of the neutrals is tighter than that of the ions because the ion spot includes ions from ionization with higher KER in addition to the dissociation.

From the time and position information we get the momentum of each fragment. From the momenta the KER and angular distributions are evaluated as mentioned in earlier sections and in detail in Appendix A. At present we discuss only the KER distribution.

The KER distribution of O_2^+ dissociation by 40 fs, 790 nm laser pulses is shown in Fig. 2.9

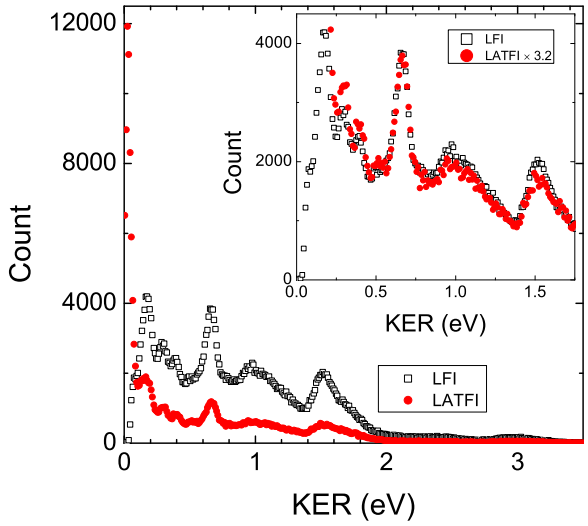

Figure 2.9: *Measured KER distributions for O_2^+ dissociation by 40 fs, 790 nm laser pulses at 4×10^{15} W/cm^2. The LFI measurements are indicated by black open squares and LATFI measurements are indicated with red solid circles. The inset shows the zoomed in version for the low KER region in order to show the structure. The LATFI data is scaled to match the heights of some of the peaks with energy slightly above 0.5 eV.*

for (i) LFI — black open squares and (ii) LATFI — red solid circles. Results from both the measurements display similar features for the energy range that can be measured in both methods. These spectra are very rich in structure. The main difference between the two measurements is that the peak at very low (near 0 eV) energy is absent in the LFI measurements as expected. This is clear evidence that the LATFI setup is working as intended for the measurement of low KER.

The very low KER peak, visible in the LATFI measurement, has a relatively higher yield compared to higher energy peaks that are present in both measurements, as shown in the inset of Fig. 2.9. The peaks in the KER region below 0.5 eV are due to vibrational structure. This suggests that both the setups have comparable energy resolution. In addition these peaks in the LATFI measurements lie on the shoulder of the large peak at very low-KER and hence the relative heights of the peaks seemingly differ from the LFI measurements. The pathways leading to such a KER distribution will be communicated elsewhere [89].

This example of O_2^+ dissociation is one where there is a higher yield at low KER than at

higher KER [89], as seen from the measurements shown above. Next we look for a system with a weaker low-KER feature, *i.e.* as is the case in the dissociation of the benchmark molecule H_2^+.

2.3.3 Dissociation of H_2^+

The measured KER distributions of H_2^+ dissociation in 10 fs, 790 nm laser pulses at an intensity of 1×10^{13} W/cm^2 are shown in Fig. 2.10 using the LFI (black open squares) and LATFI methods (red full circles). These data sets are normalized to the same number of target ions and laser pulses (method is detailed in Appendix D). The distributions in Fig. 2.10(a) show two distinct features — a broad peak around 0.8 eV and a weaker peak at very low KER. The main feature around 0.8 eV KER is mostly due to bond softening and above threshold dissociation. This feature looks similar in both measurements as expected since the energetic fragments can emerge out of the primary beam (and Faraday cup) without any losses in LFI or in LATFI.

However, there is a difference in the low-KER peak as shown in the zoomed-in plot in Fig. 2.10(b). The distribution for the LFI measurements is cut at KER $\sim$ 0.07 eV due to losses of fragments in the Faraday cup. Using the LATFI method we are able to measure the low-KER fragments down to nearly 0 eV. Detailed study of this feature, resulting from zero-photon dissociation, is presented in Chapter 3.

This example, *i.e.* dissociation of H_2^+, demonstrates that we can conduct LATFI measurements even for weaker channels at very low KER.

There is a limitation with the LATFI method on the measurements of mass asymmetric systems. As the breakup energy is shared between the dissociating fragments, we have the problem of losing the less massive fragment off the detector and the more massive fragment in the Faraday cup for certain ranges of KER, depending on the mass ratio of the fragments. For example, a previous study conducted with the LFI method on ND^+ dissociation indicated low-KER features [86] in the two dissociation channels where one channel suffers

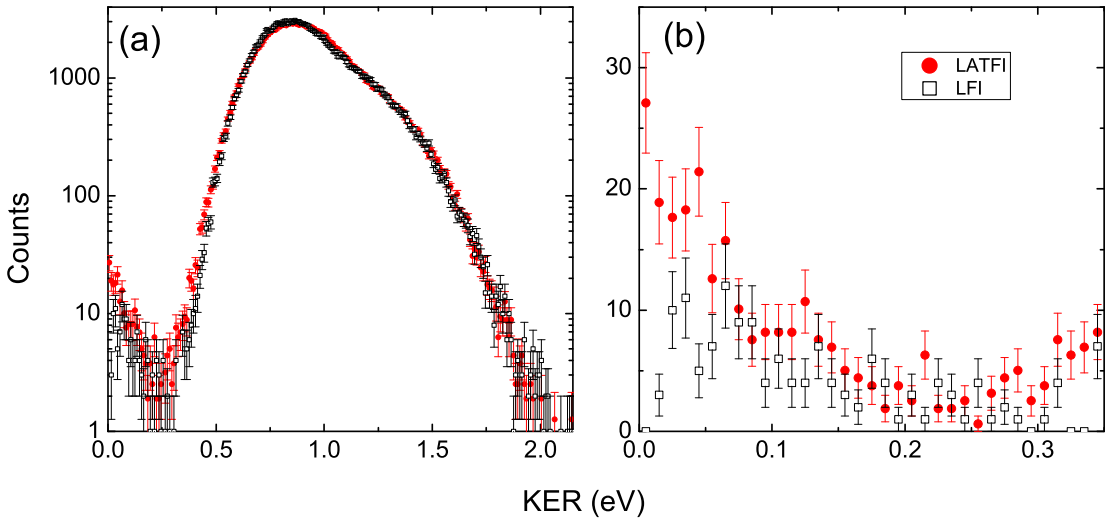

Figure 2.10: *Measured KER distributions of H_2^+ dissociation using 10 fs , 790 nm laser pulses at 1×10^{13} W/cm^2 for LFI — black open squares and LATFI — red solid circles. (a) Log scale plot for the entire KER range (b) As panel (a) but zoomed-in at low KER (below 0.35 eV) and plotted in a linear scale to show the difference between the two imaging methods at very low energy. The error bars indicate the statistical uncertainty in the experimental data.*

from the losses more than the other channel. Next we discuss these measurements of mass asymmetric molecules.

2.3.4 Breakup of mass asymmetric molecules

As we have discussed, the low-KER fragments are lost in the Faraday cup for the LFI measurements. When the fragments are asymmetric in mass, it is the heavier fragment that is mostly lost in the Faraday cup for low energy breakup. Even if we use the LATFI method, there is a limit on the ratio of the masses of the fragments for which we can measure the low KER. This is because the effective size of the detector is reduced. So, if we apply a high deflector voltage, the lighter fragment ions will hit outside of the detector. On the other hand, if we apply a low deflector voltage, the heavier fragment ions will still be lost in the Faraday cup. Similar losses of neutral fragments occur under these condition as the primary beam is not deflected enough from its field free position for this choice of the deflector

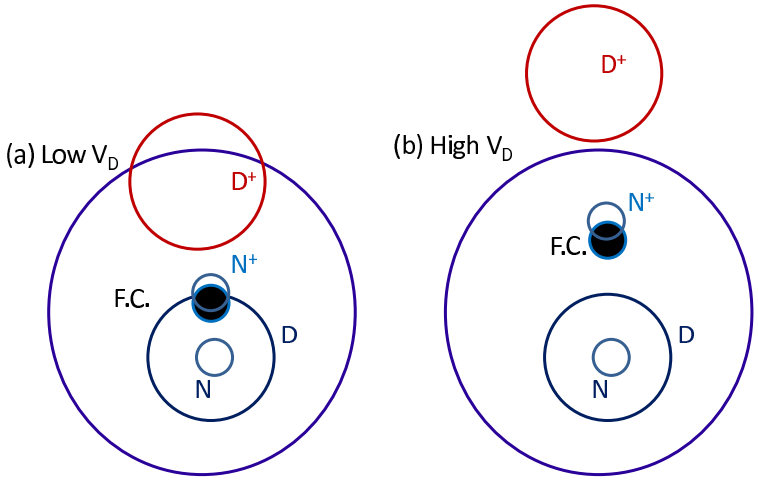

Figure 2.11: *Schematics for the measurement of low KER for mass asymmetric molecules (a) LATFI with low deflector voltage such that the lighter ions (D^+ in this example) hit the detector and most of the heavier ions are lost in the Faraday cup. (b) As (a) but with higher deflector voltage such that the lighter ions miss the detector and the majority of the heavier ions (N^+) are out of the Faraday cup.*

voltage. In addition, when the mass ratio is higher, we have to use a higher beam energy of the primary beam in order to keep proper detection efficiency of the lighter fragments. This use of higher beam energy compresses the position distribution of the fragments on the detector and also requires a higher deflector voltage to deflect compared to the lower energy beam.

To extend our LATFI measurements to somewhat more mass asymmetric molecules, we have to conduct the experiment such that each dissociation channel is measured one at a time to get the complete KER distribution of both dissociation channels. That means we lose the ability of simultaneous measurement of both dissociation channels. This measurement scheme is outlined in Fig. 2.11.

First, we measure the A^++B channel (where A is the lighter fragment) with low deflector voltage such that the lighter ions are mostly within the detector and the majority of the neutrals are out of the Faraday cup. We need to deflect the primary ion beam enough such

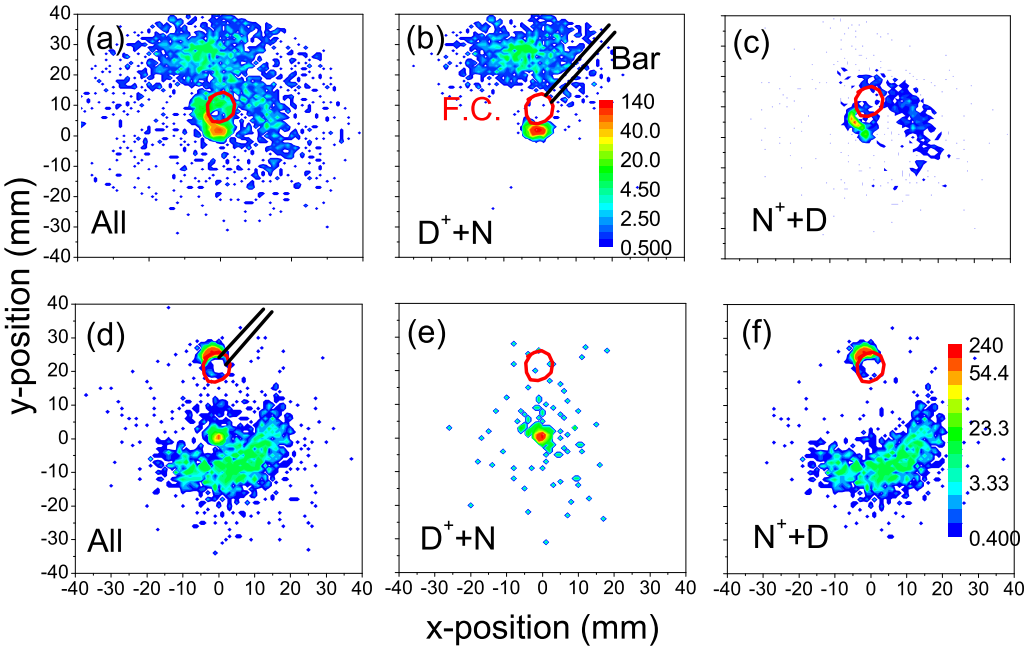

Figure 2.12: *The position spectra of hits of ND^+ fragments (a)—(c) low deflector voltage to measure the D^++N channel, (a) all hits (b) only D^++N hits, and (c) D+N^+ hits. (d)—(f) high deflector voltage to measure D+N^+ channel, (d) all hits (e) D^++N hits, and (f) D+N^+ hits. Faraday cup position is indicated with a red circle and the bar with black lines.*

that the distribution of the neutral fragments has minimum loss due to the Faraday cup, as shown schematically in Fig. 2.11(a) for an ND^+ beam. To that end, we aim the laser polarization along the ion beam direction. This helps to reduce the losses as typically the molecules tend to break along the laser polarization. Moreover it facilitates reconstruction of lost events, which relies on the cylindrical symmetry of the distribution (ϕ symmetry). For good quality data, we need to measure at least 200 degrees in ϕ out of 360 degrees.

Second, we use a higher deflector voltage to focus on the B^++A channel such that heavier ions are mostly out of the Faraday cup and the lighter ions miss the detector, as shown in Fig. 2.11(b). In addition, the neutral fragments are far from the Faraday cup shadow.

Once we get the two data sets for a particular laser intensity, we need to normalize these data sets, as explained in Appendix D. We need to match the two measurements to each other using the KER range of the B^++A channel that was measured in both cases (though less in the scheme shown in Fig. 2.11(a)), and then compare the features in the

KER distributions that are within the same range in both channels.

Results from our measurements of the position of hits on the detector are shown in 2.12, with the upper panels for low deflector voltage (40 V) and the lower panels for high deflector voltage (200 V). It seems that for low voltage on the deflector we can get a reasonable image for the D^++N channel. However, for the higher deflector voltage we are still losing the N^+ fragments in the Faraday cup from the N^++D channel. One can use an even higher deflector voltage (currently limited by the Faraday cup translational motion of the F.C. manipulator) to measure all or a large fraction of this channel. Note that more than 200 degrees of the ϕ range has been measured for the N^++D channel — enough to study this breakup process, though with more complex data analysis.

Using this method, one can measure the dissociation channel (coincidence measurement of one channel at a time) of the molecular fragmentation.

Next we discuss measurements of non-dissociative ionization of the molecular ions that are made possible with the TFI and LATFI techniques.

2.3.5 Measurements of non-dissociative ionization

Measurement of the non-dissociative ionization of molecular ions is another capability of the newly developed TFI and LATFI methods. Non-dissociative ionization results in dications, e.g. when CO^+ is ionized CO^{2+} is produced. In the LFI method these dications are captured in the Faraday cup together with the primary beam while the fragments from dissociative ionization are measured.

When CO^+ is singly ionized by the laser field, CO^{2+} is regarded as a non-dissociative ionization event and C^++O^+ and C^{2+}+O or C+O^{2+} as dissociative ionization. Among the dissociative ionization events, C^++O^+ is charge symmetric and the C^{2+}+O or C+O^{2+} are charge asymmetric. We will present the results of such non-dissociative and dissociative (mostly charge symmetric) ionization in Chapter 5.

We measure the TOF and the position of a dication hit on the detector following laser

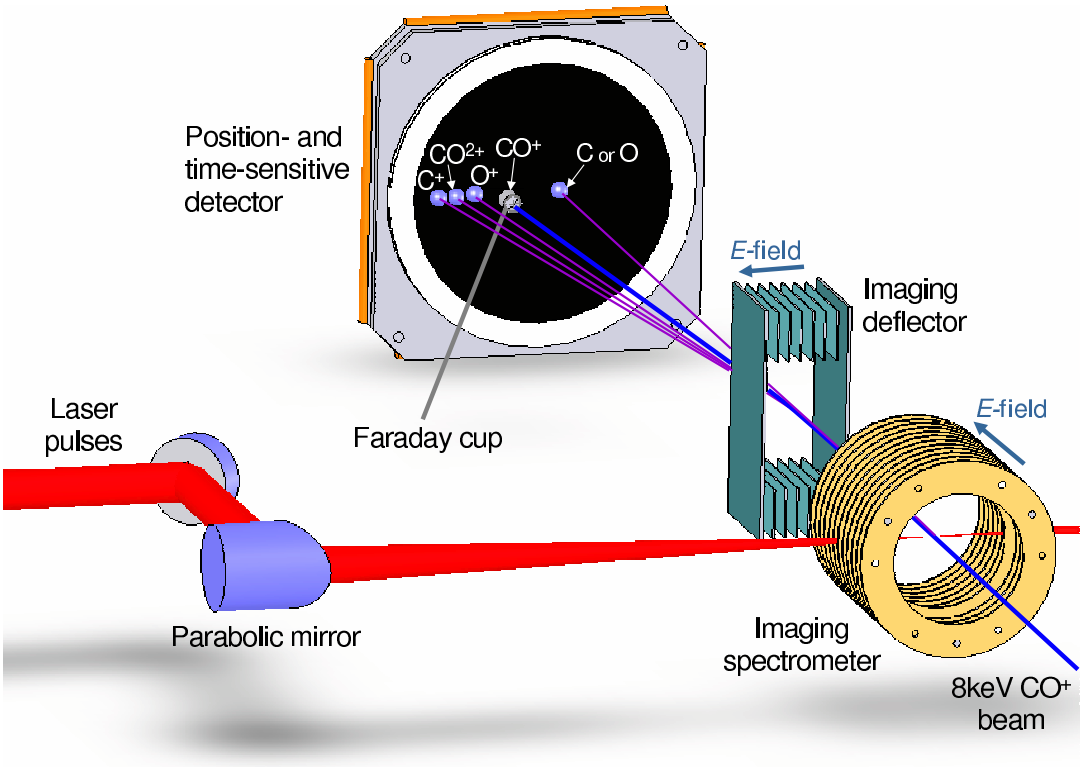

Figure 2.13: *Schematic view of the coincidence 3D momentum imaging setup with the LATFI method used for the measurement of doubly-charged ions. The neutrals hit the detector where the primary ion beam would hit in the absence of the transverse field. The deflected primary beam is captured in the Faraday cup. The doubly-charged molecule and the fragment ions are deflected further away from the primary ion beam.*

induced non-dissociative ionization of a cation molecular beam, e.g. CO^{2+} ions produced from the CO^+ ions in the presence of a laser field as shown schematically in Fig. 2.13. Here, due to the transverse static field of the deflector, the CO^{2+} ions are deflected twice the distance of the CO^+ beam, which is captured in the Faraday cup. The position distribution of the CO^{2+} lies in between the centers of the O^+ and C^+ position distributions (see Fig. 2.13). Since CO^{2+} is a molecule it is easily recognized in the TOF and position spectra by its very narrow distribution as compared to the distributions of the O^+ and C^+ fragments as shown in Fig. 2.14.

In the TOF spectrum, shown in Fig. 2.14(a), we see the forward and backward ion

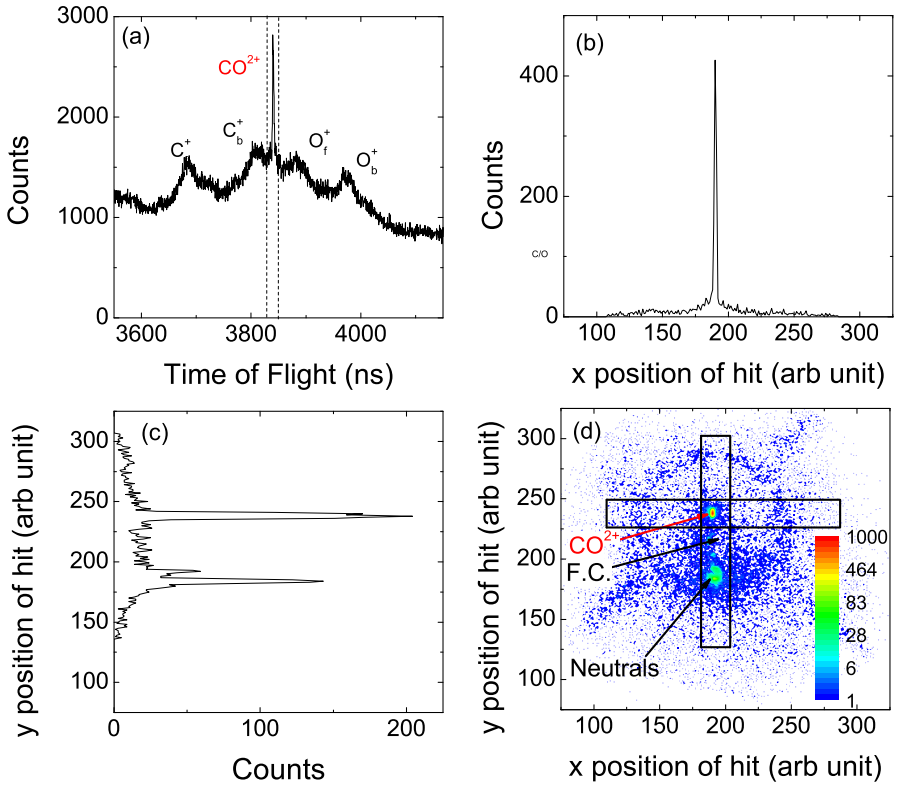

Figure 2.14: *(a) TOF spectrum of a CO^+ beam exposed to 30 fs, 790 nm laser pulses. The fragment ions have both forward and backward TOF peaks while the non-dissociative CO^{2+} ions have a single narrow peak. (b) The position spectrum gated on the CO^{2+} ion peak in panel a and projected along x. (c) Projection of the position spectrum along y, and (d) position spectrum.*

peaks, labeled C_f^+ and C_b^+, respectively as the laser polarization was set along the ion beam direction. Here forward refers to ions with their initial breakup velocity towards the detector while backward denotes ions moving away from the detector. The peak for the CO^{2+} is narrower compared to that of the fragment ions because the fragment ions have a range of energies from the breakup. By gating the CO^{2+} narrow TOF peak, we generate a position spectrum, shown in Fig. 2.14(d). We can further differentiate the metastable molecular ions CO^{2+} from the C^+ and O^+ fragment ions in the position spectra by using the fact that these fragment ions have a large spread on the detector surface due to the wide range of breakup energies. The CO^{2+} ion spot on the detector is expected to be similar to the beam spot (*i.e.* about 1 mm).

We also show the projection, within the area shown by the horizontal and vertical boxes on the position spectra in Fig. 2.14(d), along the x and y direction in Fig. 2.14(b) and (c),

respectively. The number of CO^{2+} dications is found by integrating the area under the peak in Fig. 2.14 panel(b) or (c) and subtracting the background. This method allows cleaning of the data and hence reduces the uncertainty in the measurements of the dications.

In Fig. 2.14(d), we see a spot marked as neutrals which is at the position of the primary CO^{+} beam in the absence of a static transverse electric field. These neutrals are generated mostly from the collision of the ion beam with the background gas therefore the need for better vacuum for this imaging method. The Faraday cup shadow is in the position of the deflected primary CO^{+} beam. The CO^{2+} spot is further out in the y direction. The particles scattered from the Faraday cup also contribute to the background counts, therefore the need for the background subtraction mentioned earlier.

Dissociative and non-dissociative ionization processes are discussed in Chapter 5. Below we discuss the other components of our experimental method. We begin with the laser beam and associated optics.

2.4 Laser beam and optics

The laser used in our measurements is a Ti:Sapphire system, named the Kansas Light Source (KLS), with an oscillator, stretcher, multipass amplifier, and a compressor. This combination provides linearly polarized short pulses (30 fs full width at half maximum (FWHM) in intensity), up to 2 mJ energy at a repetition rate of 2 kHz, with a fundamental wavelength of about 790 nm. Ultrashort pulses are generated when needed by compressing the regular amplified pulses using a neon-filled hollow-core fiber and chirped mirror arrangement to achieve $\leq$10 fs (FWHM) duration [80]. The laser beam is then transported to the ion beam setup. Here we use a couple of planar silver mirrors to adjust the alignment of the laser beam before it is focused onto the ion beam target using an f=203 mm off-axis parabolic mirror. The polarization axis of the laser can easily be changed to a desired angle using a half wave plate. In order to get circularly polarized light we use a quarter wave plate. The intensity of the laser at the interaction can be varied in two ways, either by using neutral

density filters [81] or by moving the position of the focus along the laser propagation direction with respect to the ion beam. The later method is called intensity difference scanning [82] and has an advantage of increased interaction volume for lower intensity measurements compared to the first method.

Once the laser beam is tuned we measure its parameters before crossing the laser and ion beams and starting to record data for experiments. Examples of such parameters include temporal width, spectral distribution, spatial profile, peak intensity, etc. Below we discuss the measurements of these parameters.

2.4.1 Temporal profile

The temporal pulse width, defined as full width at half maximum (FWHM) in intensity, of the laser pulse is measured using an autocorrelation method called Frequency Resolved Optical Gating (FROG) [90]. The laser pulse at the fundamental frequency is overlapped with a delayed replica pulse that has been frequency doubled (generated by using a second harmonic generation crystal, beta-barium-borate, known as BBO). The overlapped profile is then recorded as a function of delay using a spectrometer and analyzed using an algorithm to retrieve the information about the intensity and phase profile in the time and frequency domains.

For short pulses (30 fs), we first measure the width for the transform limited pulse and then add compensation glass to the FROG setup to account for the optical path from KLS to our ion beam setup and measure the width again. Finally, we move the compressor gratings to negatively chirp the pulses at the exit of the KLS system such that the pulses are transform limited in our ion beam setup.

For the ultrashort pulses (≤ 10 fs) generated from the hollow core fiber and chirped mirror arrangement, we measure the transform limited pulse width after adding the appropriate thickness of compensation glass. The thickness of the glass is recorded for the shortest pulse width. The intensity and phase information of a typical ultrashort pulse retrieved

from the FROG measurement are shown in Fig. 2.15(a) with intensity in arbitrary units. The temporal width of the pulse shown here is about 8 fs. The black curve represents the retrieved phase. The pulses will be positively or negatively chirped with slightly longer pulse duration if the compensation glass is thicker or thinner than the optimized glass thickness. For these ultrashort pulses we optimize the compensation glass in our setup by ionizing the background gas in our ultra high vacuum (UHV) interaction chamber. We choose to use the background gas for this purpose because the target density of our molecular ion beam is smaller by orders of magnitude than the density of background gas. We maximize the ionization yield of a particular ion (e.g. H^+ or H_2^+) by changing the thickness of the compensation glass in the optical path of the laser pulses, as the ionization is very sensitive (nonlinear) to the peak intensity of the laser. The thickness of compensation glass needed for the optimization at the ion beam setup is less than that at the FROG measurement in KLS, as the pulses travel an additional optical path of about 12 m in air to get to the ion beam. Sometimes we use a vacuum pipe in the section of the laser beam transport line, and it reduces the length of the optical path as there is no dispersion from vacuum. However, in that case the compensation glass should also account for the entrance and exit window of the vacuum pipe.

2.4.2 Spectral profile

We record the spectral profile of the pulses using a spectrometer. It gives the intensity profile of the pulse in the wavelength domain as shown in Fig. 2.15(b) by a black curve for the same ultrashort pulse (8 fs) shown in Fig. 2.15(a). In addition, we have also shown, for the same pulse, the distribution retrieved from the FROG measurement (red curve). The bandwidth of the spectrum for the two methods is similar, however there are some differences in the amplitudes of the individual peaks within the spectrum. Possible reasons for larger amplitude of the central peak in spectrometer are higher pressure in the fiber (producing white light from the interaction with ions) or amplified spontaneous emission (ASE) in

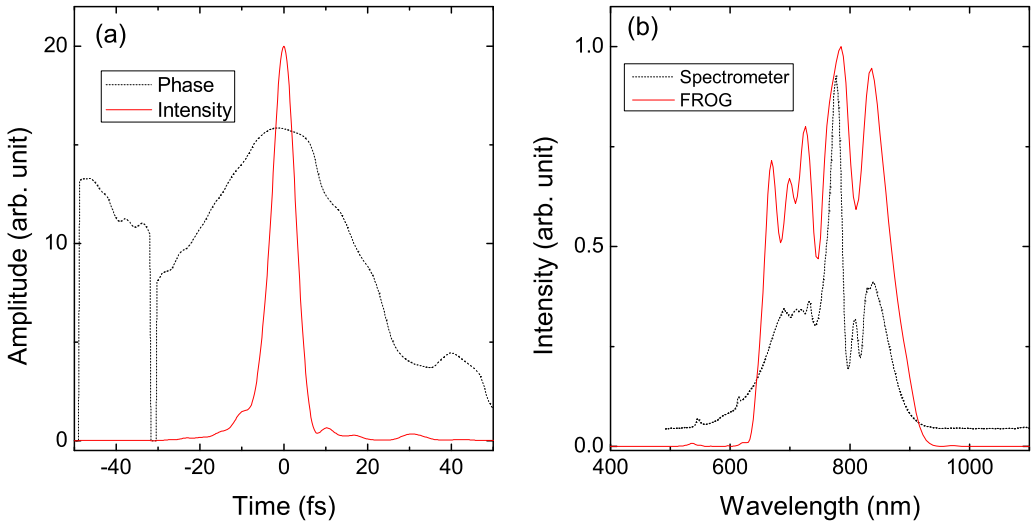

Figure 2.15: *(a) Intensity (red solid curve) and phase (black dotted curve) distribution of a typical ultrashort pulse in the time domain retrieved from the FROG measurements in KLS. (b) Intensity distribution in the wavelength (frequency) domain of the pulse in (a) measured using a spectrometer (black dotted curve) and retrieved from the FROG measurement (red solid curve).*

the output beam from the amplifier. These incoherent components can not generate the second harmonic when passed through BBO and hence no such peak appears in the FROG spectrum.

2.4.3 Spatial profile

As mentioned earlier, we focus the laser beam onto the ion beam target using an off-axis parabolic mirror. We use a beam splitter between the parabolic mirror and the entrance window of the UHV interaction chamber to generate a weak reflected replica of our laser beam. This reflected beam is directed toward a CCD camera to monitor the spatial profile of the focused laser beam. We move the parabolic mirror along the direction of the laser propagation using a translation stage. The images are recorded for a number of positions of the parabolic mirror in such a way that we scan through and cover both sides of the focus. The beam splitter is removed once we finish recording the images. We analyze the recorded

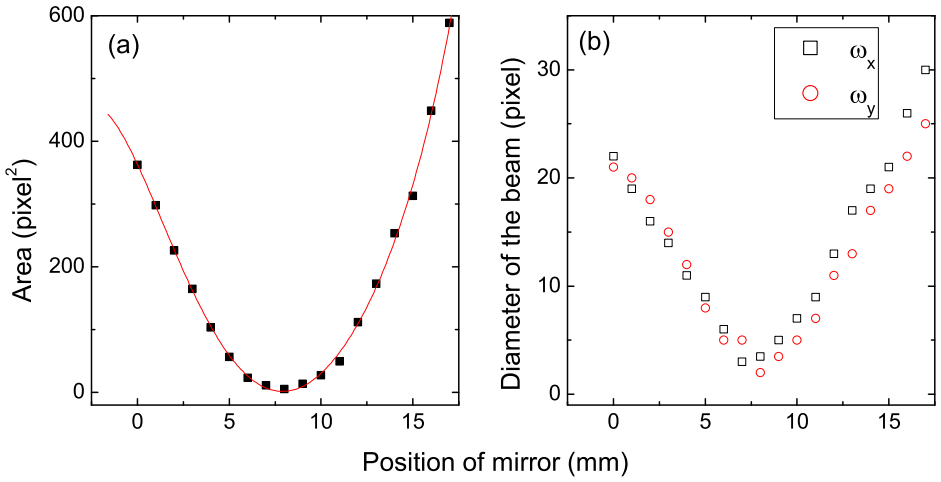

Figure 2.16: *Spatial profile of a typical laser pulse recorded by scanning the position of the focusing parabolic mirror and using a CCD camera. (a) Area of the beam. The solid red line is a fit to the data. The fit function is* $y = 363.33348 - 62.7755x - 5.33863x^2 + 1.57817x^3 - 0.0978x^4 + 0.00229x^5$. *(b) Diameter of the beam in the* x *and* y *directions (1pixel=7.5* μm*).*

images by fitting separate gaussian functions for the projection of the image along the x and y axes in order to find the beam waist along those directions. The focal spot profile as a function of mirror position for a typical laser beam is shown in Fig. 2.16. The minima of the distributions correspond to the area of the focal spot i.e $\pi \frac{\omega_x}{2} \frac{\omega_y}{2}$. The area increases symmetrically on either side of the focus. This method allows us to accurately determine the beam waist radius and the Rayleigh range, z_R, defined as the length where the intensity drops to half of the intensity at the focus.

2.4.4 Intensity calculation

The intensity of the laser in W/cm^2 is determined by

$$I = \frac{P}{f_{rep} \times A \times \Delta t} \tag{2.23}$$

where P is the measured power in watts, f_{rep} is the repetition rate of the laser in Hz, A is the area of the focal spot in cm^2 and Δt is the temporal width of the laser pulse in seconds

determined by the FROG measurement. In the experiments the laser intensity on the target ions is varied by: (i) Moving the focus of the laser with respect to the ion beam, *i.e.* the intensity difference scanning method described in Ref. [82]. In this case the interaction volume becomes larger as we move out from the center of the focus and hence the yield for low intensity processes increases improving the statistics. When we move significantly out of focus the size of the laser beam gets bigger and comparable to that of the ion beam and the condition of laser beam width smaller than ion beam width is no longer valid. Due to this the expected experimental resolution gets worse. In addition the increased interaction volume makes the comparison of the intensity averaged calculations from theory more difficult. (ii) Using neutral density filters to attenuate the pulse energy [81]. In this case the interaction volume is fixed, and hence we need to wait for a longer time for lower intensities to get similar statistics to those at higher intensities. In some lower intensity measurements we use a combination of both methods, *i.e.* move out of the focus to increase the interaction volume without losing the resolution and then add neutral density filters of desired value. However, a further drawback of neutral density filters is that they add additional positive dispersion, which is particularly important to avoid in the case of ultrashort pulses.

2.5 Ion beam

2.5.1 Ion beam production and tuning

The target molecular ions in our studies are produced in an ion source (electron cyclotron resonance — ECR source). The electron bombardment of the neutral molecules fed into the source produces a plasma in the source from which the ions are then extracted. These ions are (a) accelerated with a high voltage up to 30 kV (the source is floating relative to the rest of the beamline which is at ground potential), (b) analyzed according to their mass-to-charge ratio using a magnetic field, (c) focused using electrostatic ion optics, e.g. a pair of quadrupole lenses, (d) steered using static electric fields from deflectors and, (e) collimated using a couple of four-jaw slits. The result is that in the interaction region we have a

collimated ion beam (with a $\lesssim 1 \times 1\,\mathrm{mm}^2$ cross section) with the desired mass-to-charge ratio and beam energy. The focused laser beam crosses the ion beam at the interaction region such that the two beams are perpendicular to each other. A small Faraday cup (2 mm diameter) is used in front of the detector to collect the undissociated beam and to prevent the detector from being hit by the ion beam, which would cause permanent damage to the detector.

2.5.2 Ion beam chopping

To reduce the rate of the scattered particles from the ion beam on the detector, we chop the ion beam. We have synchronized a pulse generator that provides a static output voltage applied to a beamline deflector with the laser (photodiode) signal, *i.e.* we only allow the ion beam to be in the interaction region around the time of arrival of the laser pulse. We have recently developed a movable deflector attached to the two vertical jaws of a four-jaw slit. The advantage is a smaller potential difference is enough to deflect the primary ion beam as the electric field will be higher when the slits are closer to the ion beam.

2.5.3 Molecular ion and neutral molecule targets

There are some differences between the target ions produced in an ion source and the ions produced by ionizing the gas molecules in the same laser pulse [12, 65, 81]. For example, the vibrational population is different for H_2^+ produced in an ion source than it is for H_2^+ produced in a laser field from the neutral H_2 molecules [71]. The advantage of using molecular ions as targets is that we can study low intensity phenomena in benchmark systems like H_2^+, one of the preferred targets from a theoretical point of view because it is a less complicated problem. In the case when using neutral molecules and ionizing them with the same laser pulse, higher intensities are required to ionize the molecules. Additionally, we can use specific targets like H_3^+ that are otherwise not accessible since triatomic H_3 is not readily available like H_2 is in the diatomic case. However, the major disadvantage of the ion beam targets is the low target density compared to the neutral molecules.

2.6 Interaction region and beam crossings

As mentioned in Section 2.2, our experimental method requires crossing the laser and ion beam to create the interaction region. In the FFI and the TFI methods the interaction region is field free, but in the LFI and the LATFI methods this region is within a spectrometer and hence has a static longitudinal electric field.

To make sure the two beams overlap well in the interaction region, we measure the breakup signals on the detector and optimize the rate of a particular channel(s). We scan the position of the laser beam at the interaction region both in the horizontal (along the ion beam direction, to make sure we are not hitting the spectrometer rings) and vertical direction in the lab frame by using a translation stage on which the parabolic mirror is mounted. Then, we also scan the crossings of the two beams in the laser propagation direction such that the focus of the laser is in the center of the ion beam. From all these steps we know that the two beams are overlapped well.

2.7 Summary

In summary, we have presented the different imaging methods that can be used with our experimental apparatus for studies of laser induced molecular fragmentation, namely FFI, LFI, TFI, and LATFI . The problem associated with the FFI and LFI methods for the measurement of very low breakup energy is overcome by applying a transverse static field that allows the separation of fragments in position using the upgraded versions — TFI and LATFI. We have developed a way to distinguish the order of the hits and the breakup channels in the TFI measurements. The drawback of losing the timing signal of the second hit for very low energy breakup in TFI is resolved by using both the longitudinal and transverse static field together, *i.e.* the LATFI method.

We have demonstrated the capabilities of the LATFI method with different examples. For the low KER measurements we have shown O_2^+ and H_2^+ dissociation as evidence. In fact, these examples also show that we can measure low KER whether it is a strong or a weak

channel. We have also outlined a method, which is not simultaneous but a single channel measurement, to measure the low energy in the breakup of mass asymmetric molecules. One more capability of the TFI and LATFI methods is for the study of dissociative and non-dissociative ionization of molecular ions, which can be extended to the case of atomic ion targets. It has been demonstrated using the example of CO^+ ionization.

Chapter 3

Slow Dissociation of Molecular Ions

Molecular dissociation in intense laser field studies helps us to understand the interaction mechanisms of a strong laser field with molecules. It is natural to begin with simple systems and then apply that knowledge to more complex systems. One of the simplest systems preferred by theorists and experimentalists is H_2^+, e.g. reviews [9–12]. Though it is commonly believed that H_2^+ dynamics in an intense laser is well understood, there is still more to understand as new features are still emerging. For example, the mechanisms of laser-induced slow dissociation of benchmark molecules like H_2^+ is not well understood [7, 91]. Here the term slow dissociation means that the fragments have very low kinetic energy, almost zero eV. Previous reports on the mechanisms of such slow dissociation of H_2^+ are elusive. In the case of the simplest polyatomic molecule, H_3^+, there are not many studies in intense laser fields [83, 92], and hence H_3^+ slow dissociation requires more exploration. In this chapter we will focus on the laser-induced slow dissociation of these molecules.

In the present study we have used the LATFI method discussed in Section 2.2.4 for the measurements of low KER fragmentation. We begin this chapter with zero-photon dissociation of H_2^+ in intense ultrashort laser pulses. Experimental and theoretical results for 10 to 45 fs laser pulses at 790 nm are presented. This is then followed by measurements on the low-KER dissociation of H_3^+ (D_3^+) for different laser pulse durations and wavelengths and a discussion of the most probable pathways leading to such low KER dissociation.

3.1 Zero-photon dissociation of H_2^+

3.1.1 Introduction

Molecules are preferentially used in the study of intense laser-matter interactions as they lead to a better understanding of dynamics involved in intense laser fields. This knowledge is useful for manipulating the dynamics, for example, in laser control and time-resolved imaging of molecular reactions. In molecular dissociation, the electron cloud is localized at one of the atoms or a group of atoms while in ionization the ionized electron carries energy and also information on the dynamics. Even the dissociation of the commonly preferred target molecule, H_2, shows complex behavior in intense laser fields, such as dissociation with the absorption of less than the minimum number of required photons (see e.g. Refs. [10, 11]).

One example of nonlinear behavior in molecular dissociation is an intriguing zero-photon dissociation (ZPD), *i.e.* a molecule that dissociates by absorbing apparently no photons resulting in very low KER, KER<0.1 eV [7, 8, 11]. Of course, since H_2^+ requires at least one photon to dissociate, it is the net number of photons that is zero in ZPD.

In the literature, previous reports on the experimental evidence and the mechanisms of ZPD in H_2^+ have not been very convincing. Following early interest and excitement, a series of nice experiments were performed by Posthumus, Frasinski and co-workers [6–8] around the turn of this century. Results of those measurements had seemingly provided conclusive evidence of ZPD, where H_2^+ was formed by the ionization of an H_2 molecule with the same laser pulse and a very low-energy peak was observed in the spectrum. However, a recent Letter by Posthumus *et al.* [91] has retracted the interpretation of the earlier experiments on H_2 in which ZPD was proposed. Instead, the most recent interpretation indicates that the original data is more consistent with a resonant enhanced multiphoton ionization (REMPI)–like process [93], which is shown schematically in Fig. 3.1. Specifically, the H_2 molecule is excited to higher lying states by resonance three-photon absorption at 266 nm. Since the laser pulse used in the experiments was long the molecule can stretch to larger internuclear distance, $R > R_e$. This stretched molecule is then ionized to the H_2^+ continuum by one

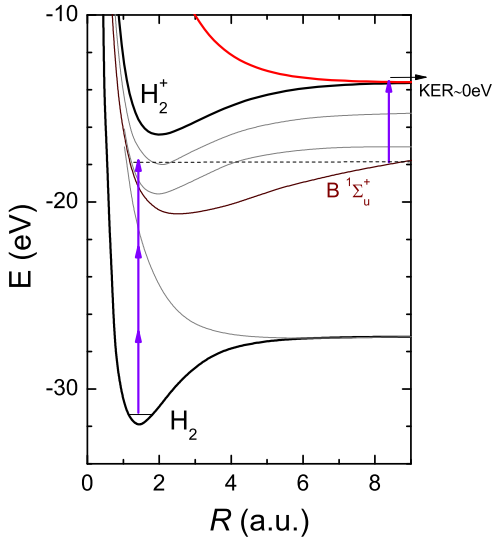

Figure 3.1: *Ground and a few relevant excited electronic states of H_2 (PECs adopted from Ref. [94]) and the two lowest electronic states of H_2^+ used to describe the REMPI process using 266 nm photons. Higher-lying excited states of H_2 can be populated with the absorption of three photons, indicated with vertical arrows, near the equilibrium internuclear distance (R_e). The molecule is then stretched and absorption of one additional photon at larger R may ionize it to H^++H. This results in very low energy breakup with KER of about 0 eV.*

additional photon and breaks into H^++H. The proton resulting from this process has very low energy, originally assigned to ZPD. On the other hand, in the earlier interpretation [7] vibrational trapping [15] was suggested to be the mechanism behind ZPD. However, the same Letter [91] shows that the angular distribution of H_2^+ dissociation that had been interpreted using vibrational trapping [15] does not need to invoke vibrational trapping at all, raising uncertainty about the existence of vibrational trapping. Furthermore, the vibrational trapping mechanism disappears when solving the time dependent Schrödinger equation for H_2^+ including nuclear rotation as discussed in Refs. [28, 29].

In view of this development, it is natural to look for evidence of ZPD using a molecular ion beam target of H_2^+. This is helpful in order to eliminate the REMPI step and to explore a lower intensity range, as there is no need to ionize the H_2 molecule by the laser pulse.

Zero-photon dissociation can be explained in terms of *vibrational trapping* [15], a mechanism already mentioned in Section 1.4, or *stimulated Raman scattering* [95]. Born-Oppenheimer PECs for the ground state ($1s\sigma_g$) and the first excited state ($2p\sigma_u$) of H_2^+ in the presence of

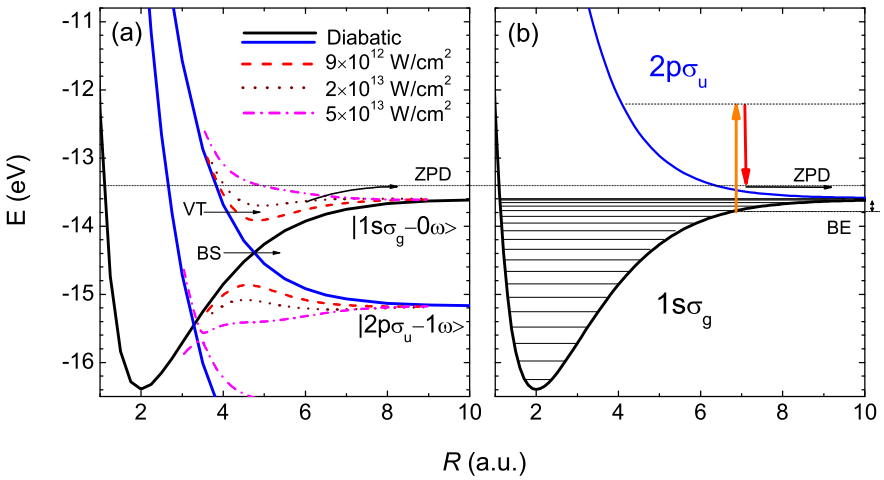

Figure 3.2: *Born-Oppenheimer PECs of the H_2^+ ground and first excited electronic states illustrating (a) vibrational trapping (VT), bond softening (BS), and zero-photon dissociation (ZPD) and (b) the stimulated Raman scattering description of ZPD, the absorption of the photon indicated by a vertical upward arrow and the emitted photon indicated by a downward arrow. BE is the binding energy of a specific vibrational level. The difference in the energy between the absorbed photon and the emitted photons is converted to kinetic energy release in ZPD after overcoming the binding energy.*

a laser field are shown in Fig. 3.2. As presented in Section 1.4, the PECs in the diabatic Floquet representation [10] are dressed up and down by n times the photon energy, $\pm n\omega$, for the emission or absorption of n photons, respectively, as shown in Fig. 3.2(a). Vibrational states near the diabatic crossing of $|1s\sigma_g\text{-}0\omega\rangle$ and $|2p\sigma_u\text{-}1\omega\rangle$ dissociate by bond softening [13, 15]. In experiments using H_2^+ molecular ion targets, dissociation by BS typically dominates and leads to a KER distribution centered around 0.8 eV.

In the adiabatic Floquet representation, mentioned in Section 1.4, a potential well is formed above the crossing of $|1s\sigma_g\text{-}0\omega\rangle$ and $|2p\sigma_u\text{-}1\omega\rangle$ that may trap part of the population of the high vibrational states ($v\gtrsim 10$), referred to in literature as vibrational trapping [15]. It was first envisioned [6, 7] that the trapped vibrational state gets pushed upward in energy above the 0ω dissociation limit with increasing laser intensity on the leading edge of the pulse. In the process the well changes shape from bound to dissociative, depositing some of the trapped population onto $|1s\sigma_g\text{-}0\omega\rangle$ which then dissociates, with overall net zero-photon

absorption. One can see that this leads to the low-KER dissociation fragments as the signature of ZPD, while the remaining population returns to the H_2^+ ground state as the laser pulse is over.

We prefer to interpret ZPD with an alternative description, *i.e.* in terms of stimulated Raman scattering illustrated in Fig. 3.2(b), because doubts have been raised about the validity of the vibrational trapping mechanism that only appears in aligned model calculations (that do not include nuclear rotation)[91, 96]. In order to overcome the binding energy of a vibrational level of the ground state with net zero photon absorption, it is required to have two photons with slightly different colors (energies). In the stimulated Raman scattering process the two driving colors are provided by the broad bandwidth of the short laser pulse. If H_2^+ absorbs a photon and later emits another one, the emitted photon may have a longer wavelength within the bandwidth of the laser pulse — a dynamic Raman effect [6, 97]. This is shown in Fig. 3.2(b) by the length of the arrow pointing down indicating the emission of a photon with less energy than the absorbed one, *i.e.* the arrow pointing up. So the energy difference between the absorbed and the emitted photon overcomes the binding energy and provides the kinetic energy of the nuclear fragments, as energy is strictly conserved. The KER due to ZPD can be evaluated from E_{abs}-E_{emit}=|BE|+KER, where E_{abs} and E_{emit} denote the energies of the absorbed and emitted photons, respectively, and BE is the binding energy of a specific vibrational level. Also, only higher vibrational states participate in ZPD, and hence the process is not very likely when starting from H_2 since ionization in the same laser pulse populates mostly the lower vibrational states [71]. Based on this picture one can predict that a shorter laser pulse (equivalently larger bandwidth) will result in more ZPD compared to a longer pulse whose narrow bandwidth does not efficiently support this mechanism. However, it should be possible in long pulses generated by chirping short pulses as they have a large bandwidth. These predictions are relatively straightforward in terms of the time-independent description based on Raman scattering compared to vibrational trapping, which is inherently time-dependent and requires non-adiabatic time evolution in

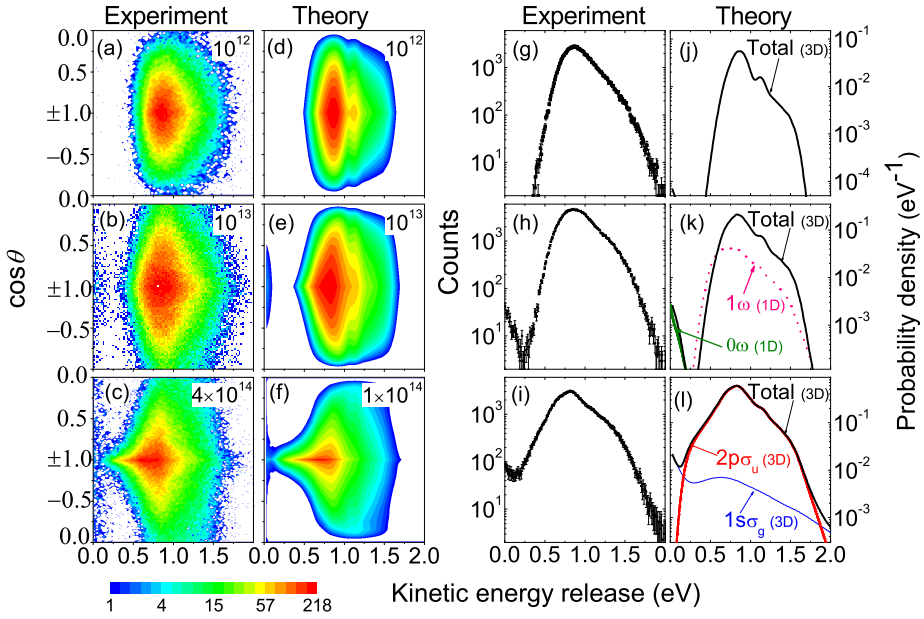

Figure 3.3: *(a–f) KER-*$\cos\theta$ *density plots for the dissociation of* H_2^+ *in 10 fs, 790 nm pulses at intensities indicated (in* W/cm^2*): (a–c) experiment, and (d–f) 3D time-dependent Schrödinger equation theory. (g–l) same as (a–f) but for KER distributions integrated over all angles. The additional lines in (k) are from our 1D Floquet-like theory method (scaled* $\times 0.25$*), see text. In (l) the total dissociation probability density is overlaid with the individual* $1s\sigma_g$ *and* $2p\sigma_u$ *contributions (3D theory). Error bars in (g–i) are the statistical uncertainty in the experimental data. The dynamic range of the false color in (a–f) is the same for all density plots.*

order to occur.

Below we present clear evidence of ZPD from both experiment and theory.

3.1.2 Clear evidence

We display KER and KER-$\cos\theta$ distributions for H_2^+ dissociation using ultrashort (10 fs), 790 nm pulses in Fig. 3.3, where θ is the angle between the molecular dissociation velocity and the laser polarization. Two distinct contributions to the spectra are visible — one main broad feature centered around a KER value of 0.8 eV and a secondary peak around 0 eV. At lower intensity (10^{12} W/cm^2, Fig. 3.3(a,g)) we observe only the main feature with a broad angular distribution. This peak is the commonly observed one-photon (1ω) dissociation by

the bond softening mechanism [13]. It progressively becomes more aligned and also extends to lower KER, with increasing intensity — in line with earlier measurements at longer pulse durations [81]. The peak at very low KER (around 0 eV) at 10^{13} W/cm^2 [Fig. 3.3(b,h)] and 4×10^{14} W/cm^2 [Fig. 3.3(c,i)] is the signature of ZPD that we are searching for, as confirmed below by our theoretical calculations.

In the calculations (Anis and Esry), the three-dimensional time-dependent Schrödinger equation is solved for H_2^+ in the Born-Oppenheimer representation including nuclear rotation, nuclear vibration and electronic excitation [28]. The Coriolis and all non-adiabatic couplings are neglected. Additionally, ionization is not included and tests show that it is negligible at the intensities used in this study. The results of these calculations, shown in Fig. 3.3, are focal-volume intensity-averaged and Franck-Condon averaged for proper comparison with our experimental results. The theory and experiment are under the same conditions except for the highest intensity where theory (10^{14} W/cm^2) is somewhat lower in intensity than experiment (4×10^{14} W/cm^2) to avoid any influence of ionization. This comparison shows a remarkable similarity between experiment and theory, except for small quantitative differences.

The obvious benefit of theory over experiment is that one can clearly assign the origin of the peaks. In theory it is possible to know on which final state of H_2^+ (the ground state $1s\sigma_g$ or the excited state $2p\sigma_u$) the population ends. Initially the system begins in the bound $1s\sigma_g$ state, and due to the interaction with the laser field it can end up in one of the two states ($1s\sigma_g$ or $2p\sigma_u$) depending on the number of photons absorbed. An odd number of photon absorption leads the population to end on the $2p\sigma_u$ state due to the dipole selection rules. On the other hand, if it is an even number of photon absorption, the population ends on the $1s\sigma_g$ state. Thus, by identifying the molecular state producing a given peak in energy, the number of photons involved can be determined with some confidence. In Fig. 3.3(l) we have overlaid the total dissociation probability density with the individual state contributions. The main peak at ∼0.8 eV is primarily from the $2p\sigma_u$ state by one-photon absorption from

$v\sim9$, *i.e.* the bond softening mechanism. Similarly, the peak at 0 eV is mostly from $1s\sigma_g$ and is thus due to absorption of an even number of photons, most likely zero (net zero to be more specific).

As confirmation of these assignments, additional calculations (Hua and Esry) have been done using a rotationless, two-channel model based on the Floquet-like representation. This method allows the separation and identification of contributions from individual photon channels [98, 99]. This representation is exact even for few-cycle pulses [98–100], despite the fact that it does share some similarities with the standard Floquet representation (and reduces to it in the continuous-wave limit). The results of this latter method at 10^{13} W/cm^2 are overlaid on the full 3D calculation in Fig. 3.3(k). They support the conclusion stated above that the low KER feature is indeed due to the absorption of a net zero number of photons (marked 0ω in Fig. 3.3(k)). Hence, the overall process related to the low KER is ZPD. In addition, the dominant contribution to the main peak around 0.8 eV is a one-photon process (marked 1ω). Therefore, we conclude from theory and experiment that we undoubtedly observe clear evidence for ZPD of H_2^+ in few-cycle 790 nm pulses.

We explore the intensity, pulse length, wavelength, and chirp dependencies of this nonlinear process next.

3.1.3 Intensity dependence

The ZPD dependence on intensity is shown in Fig. 3.3 for ultrashort pulses. There seems to be an intensity range where it is best to observe ZPD. At lower intensity, 10^{12} W/cm^2, the ZPD contribution is negligible. This makes sense as ZPD is a nonlinear two-photon process and requires a relatively higher intensity, *i.e.* the absorption of one photon followed by the stimulated emission of a second, leading to net zero photon absorption. On the other hand, at higher intensity, $\sim10^{14}$ W/cm^2, the one-photon bond softening dissociation extends to low KER and the two-photon above-threshold dissociation increases. As a result the spectrum is convoluted, and it is increasingly difficult to clearly distinguish the ZPD

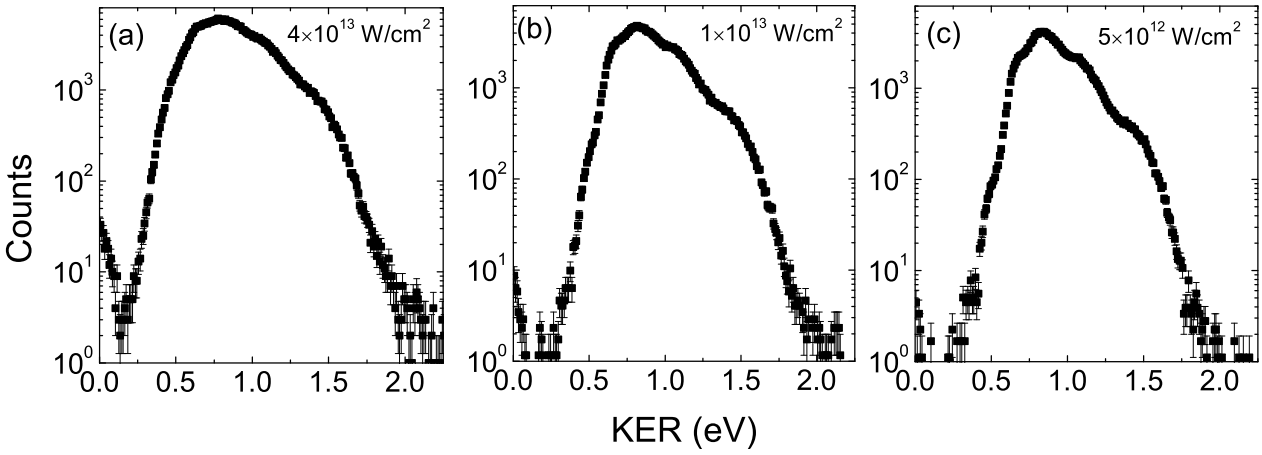

Figure 3.4: *Measured KER distributions for H_2^+ dissociation using 35 fs, 790 nm pulses with a peak intensity of (a) 4×10^{13} W/cm^2 (b) 1×10^{13} W/cm^2 and (c) 5×10^{12} W/cm^2 790 nm pulses.*

and BS contributions. In fact, even from the angular distributions we are not able to discern these different photon processes, since at low KER ($\lesssim$0.1 eV) the measured angles are not well defined. In experiments the proper measurement of angle is limited due to the finite position and time resolution of the detector. Thus, to unambiguously observe the ZPD process one must explore the $\sim10^{13}$ W/cm^2 intensity range.

Once we identify the intensity window for ZPD observation, we repeat measurements with the short 35 fs 790 nm pulses. The KER distributions for different intensities are shown in Fig. 3.4. The relative ZPD yield increases with increasing intensity from 5×10^{12} W/cm^2 to 4×10^{13} W/cm^2 while the depth of the gap between the ZPD and BS features is decreased. However, the intensity window is narrower and the relative yield of the ZPD is smaller than in the ultrashort pulses ($\sim$10 fs). Overall, the intensity dependence is very similar to that of the ultrashort pulse.

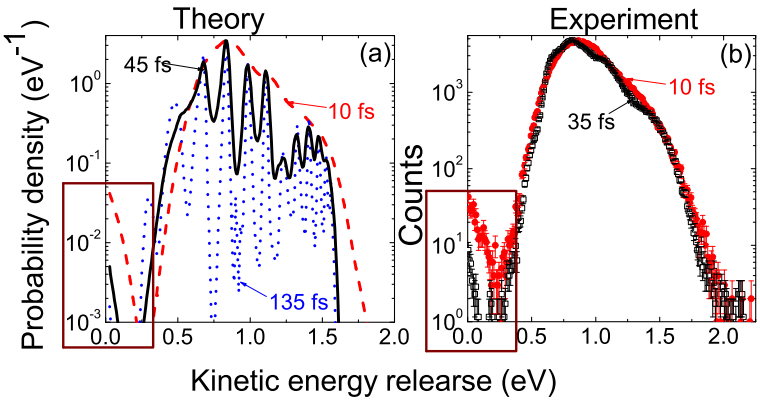

Figure 3.5: *(a) Dissociation probability density of H_2^+ as a function of KER calculated for 10, 45 and 135 fs, 790 nm pulses at 10^{13} W/cm^2. (b) Measured KER distribution for H_2^+ dissociation using 10 fs and 35 fs 10^{13} W/cm^2 pulses. Both sets of plots are normalized at their peak.*

3.1.4 Pulse length dependence

Results obtained from 3D calculations are displayed in Fig. 3.5(a) for different pulse lengths (*i.e.* 10, 45, and 135 fs) at 790 nm and 10^{13} W/cm^2 peak intensity. From Fig. 3.5(a) it is clear that the relative ZPD contribution near 0 eV reduces significantly as the pulse length increases. Based on interpretations of Raman scattering, the narrow bandwidth of long (transform-limited) pulses allows only for a small energy difference between the absorbed and emitted photons. So, for such narrow bandwidth pulses only a few highest lying vibrational levels of H_2^+ are accessible to undergo ZPD because the lower ones have a BE higher than the bandwidth. As the population of these highest lying vibrational levels is low, ZPD cannot occur effectively for longer pulses, *i.e.* narrow bandwidth pulses.

This effect is qualitatively verified by our measurements shown in Fig. 3.5(b). For short (35 fs) pulses at 10^{13} W/cm^2, the relative ZPD contribution near 0 eV is much smaller than for ultrashort (10 fs) pulses at similar intensity. This suggests that pulses with broader bandwidth are better at producing ZPD.

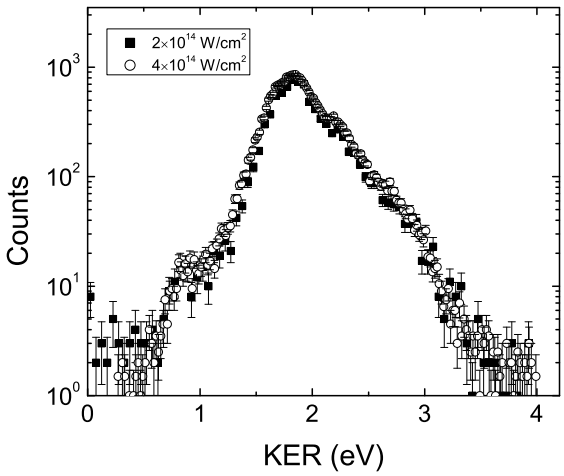

Figure 3.6: *Measured KER distributions for H_2^+ dissociation using 40 fs 2×10^{14} W/cm^2 and 4×10^{14} W/cm^2 395 nm pulses.*

3.1.5 Wavelength dependence

The measured KER distribution for the dissociation of H_2^+ using 40 fs 395 nm laser pulses for two different intensities is shown in Fig. 3.6. This KER distribution shows a broad peak around 1.8 eV. As mentioned earlier in Chapter 2, the second harmonic light at 395 nm is generated by passing the fundamental light at 790 nm through a frequency doubling crystal (BBO) and filtering out the fundamental. Since the photon energy is double that of the fundamental 795 nm light, we observed a higher KER in the dissociation by BS than in the case of 790 nm pulses.

We are looking for the very low KER feature that is the signature of ZPD. The KER distribution does not show any low KER feature suggesting no ZPD for 395 nm pulses. Very few counts at low energy in Fig. 3.6 are due to bigger bin size. One possible explanation is that the dissociation probability of the higher vibrational levels happens to be zero as shown in [96] for 395 nm pulses. The absorption of higher energy photons with the same bandwidth

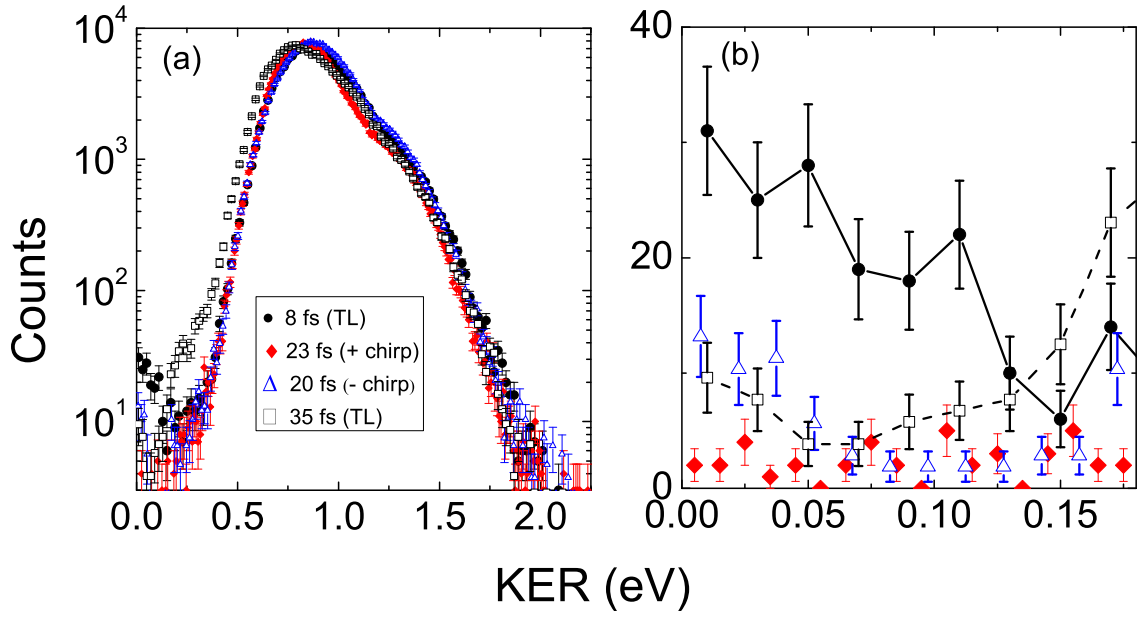

Figure 3.7: *Measured KER distributions for H_2^+ dissociation using transform limited and chirped pulses at 1×10^{13} W/cm^2, 790 nm. Error bars denote the statistical uncertainty in the data.*

leads to higher energy states in the continuum of the excited ion with lower probability to get back to the ground state in the emission. This also means that the ZPD contribution may be higher with photons at longer wavelength (smaller energy photons).

3.1.6 Effect of pulse chirp

The KER for H_2^+ dissociation using transform limited and chirped pulses at 790 nm is shown in Fig. 3.7. The positively chirped pulses are generated from the ultrashort pulses by overcompensating (*i.e.* adding more than the required thickness of the compensation glass, discussed in Section 2.4). In a similar way, the negatively chirped pulses are generated using less than the optimum thickness of the compensation glass. This method has the problem of having contributions from higher order dispersion, and the pulse profile is different than a Gaussian. For the transform limited ultrashort pulses the relative ZPD yield is higher than for the other cases considered. Between positive and negative chirped pulses the relative

yield at low KER is higher for negatively chirped pulses. For the positively chirped pulses the ZPD yield is very low, even smaller than that of the transform limited short pulse (35 fs) of longer duration.

For the negative chirp case the blue end of the spectrum leads the red end. If the absorbed photon is from the blue end and hence has higher energy than the emitted photon in the red, which is favorable for ZPD to occur, we expect to see more ZPD yield. For the same reason, the positive chirp pulses result in less ZPD. The results seemingly verify this effect, however clearer measurements are needed in which the higher order dispersion effect is eliminated.

Zero-photon dissociation in the case of the two dissociation channels of HD^+ is discussed next.

3.1.7 Channel asymmetry in ZPD of HD^+

The dissociation of HD^+ leads to two distinguishable channels, namely H^++D and H+D^+, that can be separated in our measurements. These two dissociation channels are very close in energy in their separated atom limit (the energy gap is only 3.7 meV) as shown in Fig. 3.8. Since we know the suitable intensity and the pulse duration for observing ZPD in H_2^+ measurements, we explore the ZPD of HD^+ in order to see if there is any difference between the two channels. Results from our measurements are presented in Fig. 3.9 which shows both features as in H_2^+, *i.e.* the main peak around 0.8 eV from BS and the secondary peak around 0 eV due to ZPD. It can be clearly seen that the ZPD yield for the H^++D channel is higher as shown in the zoomed-in version, Fig. 3.9(b). However, we also observe differences in the contributions from BS and the yield of H+D^+ is higher for this peak as is obvious from the difference between the two channels shown in Fig. 3.9(c).

With these observations it is not obvious what is responsible for the differences in the two channels and further exploration is required. One possibility is to do what we did for the ZPD of H_2^+, *i.e.* get help from the theory. If the results from theory suggest similar

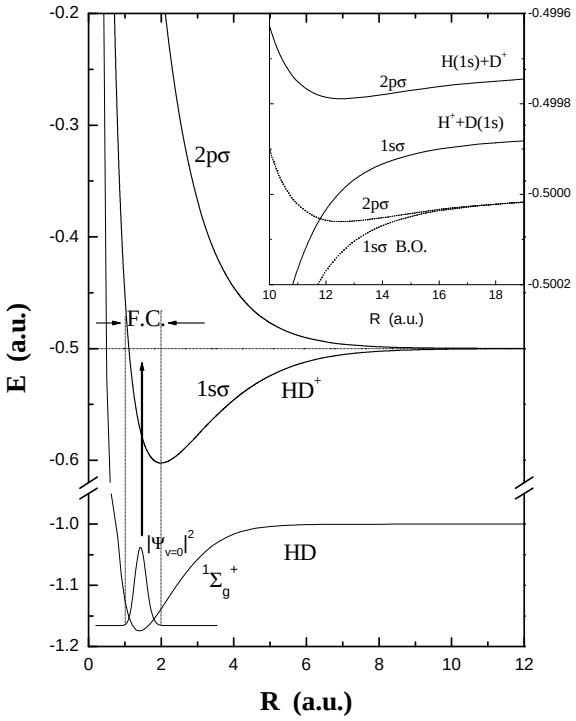

Figure 3.8: *Potential energy Curves of HD^+ adopted from Ref. [101]. The inset shows that the two dissociation limits, H^++D and H+D^+, are separated by a small energy difference.*

behavior we can try different laser parameters to find out more about these features. In the theory, some extensions in the method are required for HD^+ over the H_2^+, e.g. including the effect of the permanent dipole moment of HD^+.

3.1.8 Below threshold dissociation: BTD

In an intense laser field, molecules can dissociate by the absorption of less than the minimum number of required photons. This phenomenon is referred to as below threshold dissociation (BTD). In order to avoid REMPI process, it is natural to look for evidence of BTD using a molecular ion beam target of H_2^+. To this end, two separate experiments at about 790 nm by Pavičić *et al.* [68] and McKenna *et al.* [102] were performed using H_2^+ produced in an ion source and relatively long laser pulses, 130 fs and 50 fs, respectively. In their results, peaks in KER are briefly assigned to BTD by net one-photon absorption. It is not clear

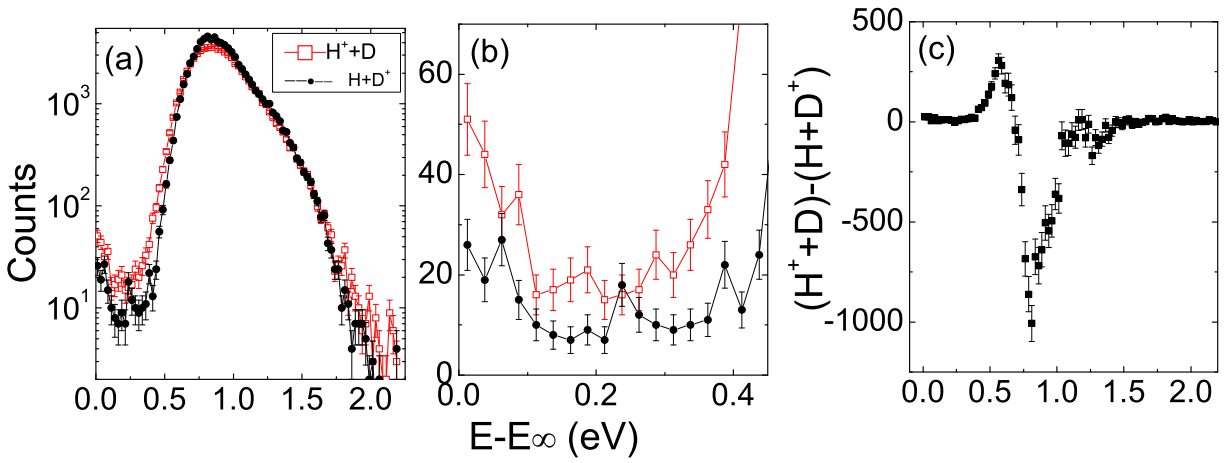

Figure 3.9: *(a) Measured KER distributions for HD^+ dissociation into $H^+ + D$ and $H + D^+$ using 8 fs 5×10^{13} W/cm^2 790 nm pulses. (b) Zoomed in for low KER feature (linear scale) (c) Difference between $H^+ + D$ and $H + D^+$ channels.*

that the assignments of BTD in these previous experiments are correct [68, 102]. The rapid drop-off of ZPD with increasing pulse duration as seen in the calculations and measurements presented in this work would suggest that the role of BTD at the pulse durations used in Ref. [102] (50 fs) and Ref. [68] (110 fs) should be minimal. In both cases a broadening of the angular distribution near 0 eV was taken as a trademark of BTD. However, at low KER the measured angular distribution is not well defined, as evidenced also in our measurements. Thus, at the intensities used in those experiments ($>10^{14}$ W/cm^2) it is plausible that the low KER comes instead from the one-photon bond softening dissociation of near threshold low vibrational states ($v\sim6$) or from two-photon above-threshold dissociation.

3.1.9 Zero-photon dissociation summary

We have presented clear evidence of very low-KER, down to almost 0 eV, in the dissociation of H_2^+ in an intense laser field using the LATFI method. This low KER feature is attributed to the mechanism called zero-photon dissociation as confirmed by the theoretical results. The intensity dependence suggests a narrow range for the best observation of the ZPD in H_2^+. On the other hand, the pulse length dependence shows that the ultrashort pulses are

very good for ZPD studies as they have a broader bandwidth.

These observations are explained with a simple time independent picture, *i.e.* the stimulated Raman scattering. In this two-photon process, the energy difference between the absorbed and emitted photons is imparted to the molecular dissociation.

In addition, we observed no ZPD using second harmonic pulses at 395 nm, due to the smaller dissociation probability of the higher vibrational levels of H_2^+ for 395 nm photons. The chirped pulse measurements indicated that the ZPD yield is higher for negatively chirped pulses compared to positively chirped pulses. In our measurements, we observed a channel asymmetry not only in ZPD but also in the BS/ATD of HD^+. This is indeed interesting and needs more detailed study (including theory) to confirm such differences and determine their source.

3.2 Low-KER dissociation of H_3^+

3.2.1 Introduction

The triatomic hydrogen molecular ion, H_3^+, is important on a fundamental level and is one of the major constituents of the universe. This species has been explored in the laboratory for years. Many of these studies have been limited to collision experiments, e.g. [103, 104], or weak-field spectroscopy [105, 106]. Exploring the non-linear behavior of H_3^+ (or its isotopes) in ultrashort intense laser fields is beneficial as it can lead to a better understanding of the laser-driven dynamics of complex polyatomic molecules — in a similar way that H_2^+ has been a benchmark system for studies of diatomic molecules [10, 11].

Until lately there were no published experimental studies on H_3^+ and its isotopes in intense ultrashort laser fields. Recently, we reported breakthrough measurements of D_3^+ dynamics in such laser fields measured by coincidence three-dimensional momentum imaging [83]. The focus of that work was on the ionization channels, namely the fragmentation of the transient D_3^{2+} and D_3^{3+} ions and the associated angular distributions. In parallel, Alexander *et al.* [92] reported photodissociation of D_3^+ that was allowed to vibrationally cool in an

electrostatic trap [107]. They found that the dissociation rate dropped as a function of the time the D_3^+ ions were allowed to cool. This suggests that dissociation is dominated by excited vibrational states under the laser conditions used.

The study of D_3^+ dissociation is important in many ways. By evading ionization, only the nuclear dynamics of D_3^+ need to be treated by theory, making it computationally more manageable but still challenging. The D_3^+ ion also has a rather unusual geometry forming an equilateral triangle in its unperturbed ground state which in turn might lead to an interesting angular distribution in the breakup. When dressed with an intense laser, the D_3^+ electronic ground state, $X\,^1A'$, is coupled with the first excited state, $2\,^1A'$, in C_s symmetry (isosceles triangle). These states lead to different two-body dissociation limits, D^++$D_2(X^1\Sigma_g^+)$ and $D_2^+(X^2\Sigma_g^+)$+D(1s), respectively. Alternatively, in D_{3h} symmetry (equilateral triangle) the coupling between the first excited state, $1^1E'$, and the ground state lead to the degenerate three-body dissociation limit forming D^++D(1s)+D(1s). These properties of the D_3^+ molecule raise many questions, for example, which way does the molecule prefer to break up, *i.e.* to the two- or the three-body dissociation limit? Does the breakup release high energy or not? What are the dissociation pathways involved? etc.

Here we attempt to answer some of these questions by exploring the dissociation of H_3^+ and D_3^+ in ultrashort (10–40 fs), 790 and 395 nm intense laser pulses. Using the dissociation kinetic energy release distributions, we determine the most likely dissociation pathways. We also reassess the dissociation pathway assignments of Alexander *et al.* [92], whose measurements were limited to time-of-flight of the neutral fragments without being able to distinguish different dissociation channels (namely D^++D_2, D+D_2^+ or D^++D+D). A better assignment of the dissociation path is made possible by the coincident nature of our measurement in which all the fragments are detected and all channels are clearly separated as shown in Fig. 3.10. Furthermore, we assert a form of control over dissociation by influencing the pathway using the pulse duration.

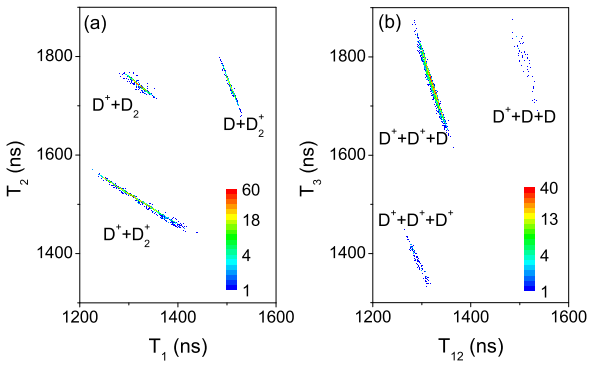

Figure 3.10: *Coincidence time of flight (TOF) spectra as a density plot for the fragmentation channels of D_3^+ using ultrashort 10 fs, 790 nm laser pulses at an intensity of 1×10^{16} W/cm^2. (a) A density plot as a function of the TOF of the first particle (T_1) and the second (T_2) for two-body break up. (b) A density plot as a function of the TOF of the center of mass of the first two particles (T_{12}) and the third particle (T_3).*

3.2.2 Results

Different fragmentation channels of D_3^+ induced by an intense laser are displayed as coincidence TOF spectra in Fig. 3.10. For the two-body breakup channels we present the data as a density plot as a function of the TOF of the first fragment (T_1) and second fragment (T_2). In the three-body breakup channels we have used the TOF of the center of mass of the first and second particle together (T_{12}) along the horizontal axis and that of the third particle (T_3) along the vertical axis. This makes the signals look like that of the two-body breakup, *i.e.* a narrow stripe in the coincidence map due to momentum conservation. One can see that each reaction channel is nicely separated from the other. In addition, the density of the points is an indication of the relative yield of the corresponding channel, e.g. the three-body dissociation into D^++D+D is the weakest channel in Fig. 3.10.

The target ions in our experiment, produced by D_2^++D_2→D_3^++D collisions in an ion source, are vibrationally excited. The vibrational population of H_3^+ and D_3^+, evaluated by Anicich and Futrell [108], are shown in Fig. 3.11. These distributions are peaked around 2 eV above the minimum of the ionic potential energy surface.

Fragmentation of D_3^+ in a strong laser field leads to two- and three-body breakup as

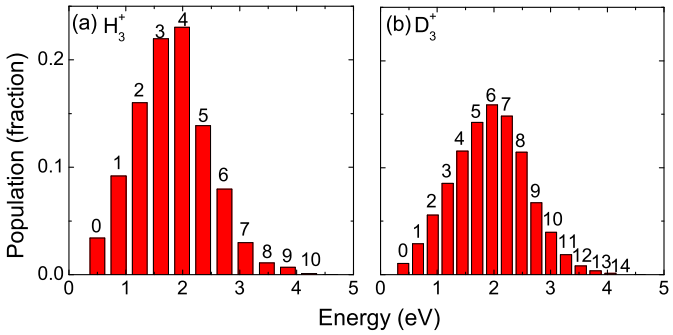

Figure 3.11: *Vibrational population as a function of energy from the minimum of the potential energy surface of (a) H_3^+ and (b) D_3^+ evaluated by Anicich and Futrell [108].*

shown in Fig. 3.10. The breakup channels of D_3^+ *dissociation* are:

$$\begin{aligned} D_3^+ + n\omega &\rightarrow D^+ + D_2 \\ &\rightarrow D_2^+ + D \\ &\rightarrow D^+ + D + D \end{aligned} \tag{3.1}$$

where $n\omega$ denotes the multiphoton interaction with the strong laser field. Another channel that has one neutral fragment as a final product is the (three-body breakup) *single ionization* reaction:

$$D_3^+ + n\omega \rightarrow D^+ + D^+ + D + e^- \tag{3.2}$$

If only neutral fragments are measured one can not discard the possibility of low KER from this channel too. Through our coincidence measurements, we find that the KER in this ionization channel (*i.e.* D^++D^++D) is about 10 eV [83]. This means that the neutral D atom from this channel has about 2 eV of energy (the D^+ ions share 4 eV each) and hence D does not contribute to the very low energy range.

The next possible candidate for low KER is the three-body breakup, (D^++D+D) dissociation channel. However, as is evident from Fig. 3.10, the yield of this channel is extremely

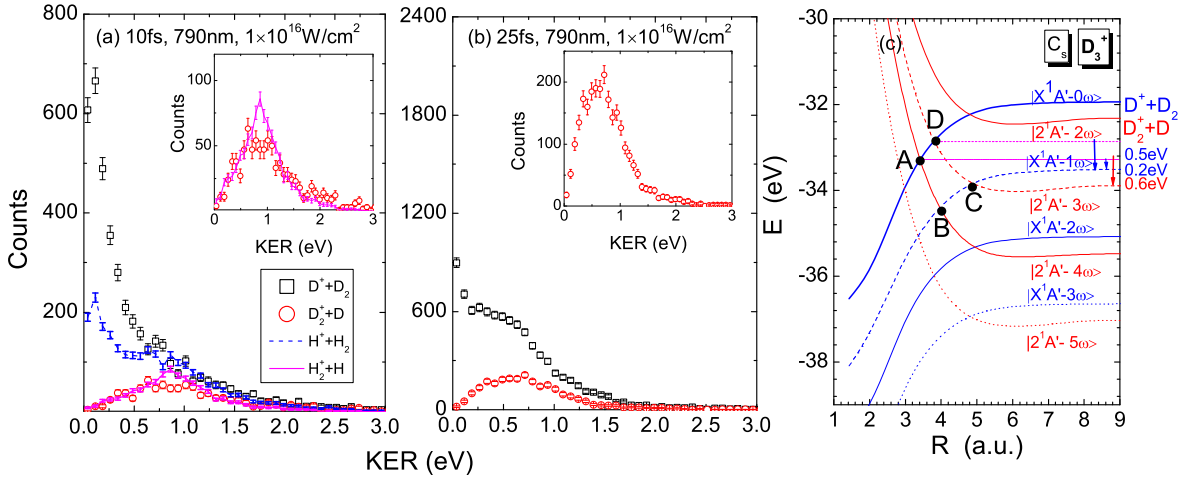

Figure 3.12: *KER distributions for the two-body dissociation of D_3^+ using (a) 10 and (b) 25 fs, 790 nm laser pulses at an intensity of 10^{16} W/cm^2. Open black squares are for the $D^+ + D_2$ channel and open red circles are for the $D_2^+ + D$ channel. The lines in (a) are the equivalent for H_3^+. The error bars indicate the statistical uncertainty in the experimental data. The vertical scales in (a) and (b) are arbitrary relative to one another. This is done in order to visually normalize the peaks of the $D_2^+ + D$ and $H_2^+ + H$ channels to aid comparison. The insets of (a) and (b) show an expanded view of the normalized $D_2^+ + D$ channel. (c) Light-dressed potential energy diagram of D_3^+ using the field-free potentials from Ref. [109] for the C_s symmetry (isosceles triangle configuration). For this isosceles geometry, R is the distance between the midpoint of two of the nuclei and that of the third nucleus (see text). The ground electronic state is X^1A' leading to the $D^+ + D_2$ limit at $R \to \infty$, and the first excited electronic state is $2^1A'$ leading to the $D_2^+ + D$ limit. In the dressed states ω refers to the energy of a 790 nm photon.*

low. One possible reason for this is that the D_3^+ well is deep in the D_{3h} symmetry and requires five or more 790 nm photons to make a dissociative transition. There are not enough events that satisfy the coincidence TOF gate and momentum conservation conditions to determine the energy and angular distributions for this three-body breakup channel.

Therefore, we can rule out the possibility of significant low KER contributions from three-body breakup and hence from now on focus on the two-body dissociation channels. We present in Fig. 3.12 the results of laser induced two-body dissociation of D_3^+ as KER distributions using ultrashort (10 fs) and short (25 fs) 790 nm laser pulses at 10^{16} W/cm^2.

From Fig. 3.12(a) one can see that the $D^+ + D_2$ channel dominates over the $D_2^+ + D$ channel

for an ultrashort 10 fs, 790 nm laser pulse at 10^{16} W/cm^2. This channel has a low KER peak and also has a KER tail extending from 0.25 eV to above 1.5 eV, which is indicative of more than one probable dissociation pathway contributing to this KER. In contrast, the D_2^++D channel shows little-to-no events near 0 eV and has instead a rather broad distribution (*inset*) peaked at about 0.8 eV but also extending to above 1.5 eV. The high energy tail (>1 eV) of both channels look similar to each other.

To determine which dissociation pathways can lead to these KER distributions we survey the light-dressed states [23, 25] (Floquet diagram discussed in Section 1.4) of D_3^+ plotted in Fig. 3.12(c). The potential curves, representing special symmetry cuts in the potential energy surfaces, are taken from the work by Talbi and Saxon [109]. For C_S symmetry (isosceles), the internuclear separation of two of the nuclei is fixed (r) while the distance between their mid-point and the third nucleus (R) is stretched. Talbi and Saxon calculated the R for fixed diatomic internuclear separation r that is at the minimum of the ground state energy surface. The dissociation limit of the ground state, $X\,^1A'$, is D^++D_2, while that of the excited state, $2\,^1A'$, is D_2^++D, thus, dissociating populations ending on the $X\,^1A'$ and $2\,^1A'$ states will lead to these respective fragmentation channels. As mentioned in Section 1.4, the KER value is easily found by evaluating the difference in energy between the starting point and the final dissociation limit. For example, a few energies (or KER) relevant to the current work are marked by the vertical arrows in Fig. 3.12(a). However, we do emphasize that these energies will only be approximate as bond softening [13, 14] can lead to dissociation of vibrational (v) states above and below the initial crossings which in turn leads to higher and lower KER values observed. Additionally, the diatomic fragment (D_2 or D_2^+) may end up vibrationally excited thereby lowering the KER measured. One can also think about the D atom being in an excited state, but the excited state of D is much higher than the photon energy and will lead to very different KER than what we have observed.

To explain the large peak at around 0.15 eV in the D^++D_2 KER distribution there is

only one apparent pathway available, $|X\,^1A'\text{–}0\omega\rangle \rightarrow |2\,^1A'\,\text{–}4\omega\rangle \rightarrow |X\,^1A'\text{–}1\omega\rangle$. This pathway is expected to lead to KER of around 0.2 eV in keeping with the measured value. The $D^+ + D_2$ channel can also be populated by the pathway $|X\,^1A'\text{–}0\omega\rangle \rightarrow |2\,^1A'\,\text{–}3\omega\rangle \rightarrow |X\,^1A'\text{–}1\omega\rangle$ which gives KER near 0.5 eV. Although the tail of the measured distribution extends substantially higher in energy than this value, dissociation of v states above the initial crossing (v=12–14) can result in higher KER. Indeed, the likely reason that the 0.2 eV peak dominates is because its crossing is accessing lower v states ($v\sim$10) that have higher populations (see Fig. 3.11).

By similar deduction the pathways that can account for the $D_2^+ + D$ distribution are $|X\,^1A'\text{–}0\omega\rangle \rightarrow |2\,^1A'\,\text{–}4\omega\rangle \rightarrow |X\,^1A'\text{–}1\omega\rangle \rightarrow |2\,^1A'\text{–}3\omega\rangle$ and $|X\,^1A'\text{–}0\omega\rangle \rightarrow |2\,^1A'\text{–}3\omega\rangle$, roughly giving KER values of 0.6 eV and 1.0 eV, respectively. While at first sight it may seem strange that the $D_2^+ + D$ channel does not have a sizeable feature near 0.1 eV arising from the two-photon pathway $|X\,^1A'\text{–}0\omega\rangle \rightarrow |2\,^1A'\text{–}2\omega\rangle$, it becomes more obvious once the vibrational population is considered. This crossing is about 4.3 eV above the bottom of the potential well and as shown by Fig. 3.11 there is very little population at this energy.

It is a good idea to further test the dissociation pathways proposed above. One approach to test the validity of the dissociation pathway mentioned earlier is to use a lighter nuclear mass keeping the same pulse duration and compare the dynamics, e.g. using H_3^+. As an example, a classical estimate indicates that, in the case of D_3^+, it takes the nuclear wavepacket about 14 fs to go from the crossing marked 'A' in Fig. 3.12(c) to the one marked 'C' (via 'B'). So, for an ultrashort pulse (10 fs), a nuclear wavepacket traveling between 'A' and 'C' will mostly stay on the $|X\,^1A'\text{–}1\omega\rangle$ curve rather than transit to the $|2\,^1A'\text{–}3\omega\rangle$ curve as the crossing at 'C' is likely to be closed when the wavepacket reaches there (note that the curve crossings are open only in the presence of a strong laser field). By this reckoning one would expect the low-KER peak in the $D^+ + D_2$ distribution to reduce in amplitude for longer pulse duration, since more population will spill onto the $|2\,^1A'\text{–}3\omega\rangle$ state due to the crossing 'C' being open longer. The results from our measurements are shown as lines in Fig. 3.12(a) for

H_3^+. Comparing the lines for the similar channels of D_3^+, one can see the equivalent behavior [30]. In this scenario, the lighter H_3^+ enables the nuclear wavepacket to travel $\sqrt{2}$ times faster than for D_3^+ thus reducing the travel time between crossings. As a result, for 10 fs laser pulses, more of the wavepacket traveling from 'A' to 'C' exits the $|X\,^1A'\text{–}1\omega\rangle$ state via crossing 'C' for H_3^+ than for D_3^+, resulting in the observed drop in the signal at low-KER for H_3^+ in Fig. 3.12(a).

Another method that proves useful is adjustment of the laser pulse duration [30]. Figure 3.12(b) shows the results from our measurements of D_3^+ dissociation using short pulses (25 fs). The low KER in the D^++D_2 channel is reduced in amplitude by comparison with the rest of the distribution, supporting the above argument because the pathway leading to 0.2 eV KER is now adiabatic at point C in Fig. 3.12(c). Naturally, one would expect a corresponding signal increase in the D_2^++D channel around 0.6 eV.

Another convenient way to check the pathways involved in our discussion is to use frequency doubled light (*i.e.* a 395 nm photon that is equivalent to 2ω of 790 nm). The results from this measurement are shown in Fig. 3.13(a). In this case one eliminates the dressed states involving an odd number of 790 nm photons shown in Fig. 3.12(c) leading to the potential energy curves presented in Fig. 3.13(b). It is clear that the pathways discussed for 790 nm which involved an odd number of photons are now absent altogether, and this results in the distinct reduction in the low-KER feature of the D^++D_2 channel at 395 nm. The new dominant pathways at 395 nm are most likely the $|X\,^1A'\text{–}0\omega\rangle\rightarrow|2\,^1A'\text{–}6\omega\ \rangle\rightarrow|X\,^1A'\text{–}2\omega\rangle$ and $|X\,^1A'\text{–}0\omega\rangle\rightarrow|2\,^1A'\text{–}6\omega\rangle\ \rightarrow|X\,^1A'\text{–}2\omega\rangle\rightarrow|2\,^1A'\text{–}4\omega\rangle$ giving estimated KER values of about 0.5 eV and 0.9 eV, respectively (recall that 2ω denotes one 395 nm photon). The actual KER distributions for the D^++D_2 and D_2^++D channels, shown in Fig. 3.13(a), consistently peak slightly higher than expected values. This deviation, as before, can arise from dissociation of v states above the $|X\,^1A'\text{–}0\omega\rangle$—$|2\,^1A'\text{–}6\omega\rangle$ crossing. In fact, our measurement of the relative dissociation rate, at similar peak intensities for both wavelengths, is substantially higher for 395 nm than for 790 nm (about a factor of 50). This

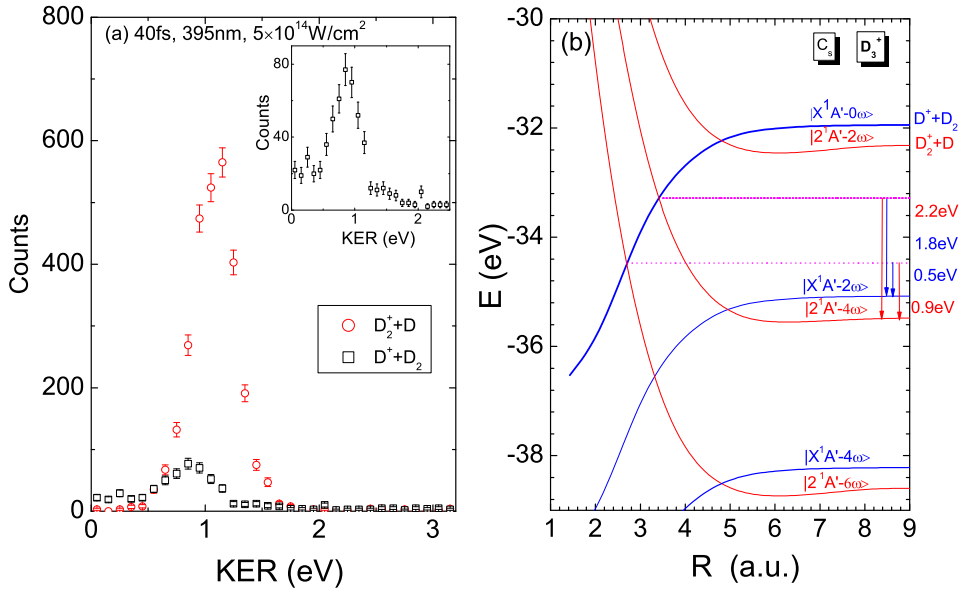

Figure 3.13: *(a)KER distributions for two-body dissociation of D_3^+ using 40 fs, 395 nm laser pulses at an intensity of 5×10^{14} W/cm^2. The inset shows an expanded view of the $D^+ + D_2$ channel. (b) Light-dressed potential energy diagram of D_3^+ where the potentials have been calculated in [109] for the C_s symmetry (isosceles triangle configuration). The dressed states are for the energies (ω) of the 790 nm photon (only even numbers, that are equivalent to 395 nm photons, are shown). The vertical arrows indicate the KER (in eV) for a selection of dissociation pathways.*

is consistent with the fact that the D_3^+ vibrational population (Fig. 3.11) peaks near the $|X\,^1A'\text{–}0\omega\rangle$—$|2\,^1A'\text{–}6\omega\rangle$ crossing, which lies ~2 eV above the minimum of the potential well (Fig. 3.13(b)).

Before summarizing, it is worth commenting on the recent D_3^+ photodissociation findings by Alexander *et al.*[92]. In their measurements, using 30 fs, 800 nm pulses, the vibrational population of D_3^+ was allowed to radiatively cool over tens of milliseconds [92], and the dissociation signal was measured as a function of the cooling time. Unfortunately, their time-of-flight detection scheme only allowed for the detection of neutral fragments with no information on the type of species involved (*i.e.* D or D_2 fragments were not distinguished). Alexander *et al.* found that their KER spectra were dominated by a very low energy peak

(near 0 eV), as in our present measurements, that diminished as the molecules cooled. From the limited information available at the time the authors attributed this KER feature to dissociation driven by a two-photon transition from the ground $X\,^1A'$ to the excited $2\,^1A'$ state (in C_s symmetry) leading to the D_2^++D channel. They also proposed that at higher intensities the ionization channel D^++D^++D may also contribute to the formation of low energy D fragments.

Based on our measurements, it seems that these earlier deductions may not be accurate. The low-KER dissociation instead comes from four-photon excitation (from $X\,^1A'$ to $2\,^1A'$) followed by three-photon emission (from $2\,^1A'$ back to $X\,^1A'$), with the final products being D^++D_2, rather than D_2^++D as suggested in [92]. This insight is strongly founded on the fact that we are able to clearly distinguish the D_2^++D and D^++D_2 channels (as well as all others) and observe that the D_2^++D channel has no peak near 0 eV (see Figs. 3.12(a) and 3.12(b)). We also find from our measurements of the D^++D^++D ionization channel that the neutral fragment from this channel does not contribute in the low energy range. While one cannot rule out that different ion source or experimental conditions lead to different behavior of D_3^+ in the two experiments, it does appear unlikely as the two-photon crossing suggested by Alexander *et al.* to explain dissociation is about 4.3 eV from the potential minimum with the population in these high states surely being extremely low (see Fig. 3.11).

3.2.3 Low-KER dissociation of D_3^+ summary

In summary, following the recent upgrade of our experimental method to be able to measure low (and high) KER fragments in coincidence, we have conducted a study of the dissociation dynamics of a D_3^+ molecular ion-beam in an intense ultrashort laser field. From the measured KER distributions and a light-dressed states picture of the D_3^+ potentials the relevant dissociation pathways at 790 nm and 395 nm have been deduced. Indeed, we have shown that there are important time-dependent dynamics involved that would need to be taken into account in any future calculations of the strong-field behavior of this molecule. Finally,

the low-KER feature is associated with the $D^+ + D_2$ channel and not the $D_2^+ + D$ as reported previously.

Chapter 4

Fast Dissociation and Ionization of N_2^+

4.1 Introduction

In Chapter 3 we discussed the slow dissociation of benchmark molecules H_2^+ and H_3^+ in an intense laser field. In this chapter we explore the dissociation and ionization of an N_2^+ beam in intense ultrashort 790 nm laser pulses. The single and multiple ionization of N_2 molecules in a strong ∼800 nm laser field has been studied experimentally by several groups (e.g. [33, 50, 72, 74, 78, 79, 110–112]) but never before starting from an N_2^+ beam target. In particular, we focus on an unusually high-KER feature in the dissociation of N_2^+ into N^++N. This high-KER peak is more than 5 eV higher than a low-KER peak that has commonly been observed for N_2^+ dissociation starting from an N_2 target. The separation of the low (0.6 eV) and high (6.1 eV) KER peaks is much larger than the photon energy (1.57 eV) for 790 nm wavelength. In addition, we show that the dissociation pathways responsible for this high-KER feature lead to KER values in ionization much higher than expected for Coulomb explosion into N^++N^+. Although the intensity range covered, up to 6×10^{15} W/cm^2, spans into the tunneling regime, we find it informative to interpret the results using the Floquet picture, exemplified in Fig. 1.1 for H_2^+ in Chapter 1. This is because the Floquet dressed-states picture allows for clear identification of both dissociation and ionization pathways using their KER and angular distributions, as well as their intensity dependence [34, 36, 37].

4.2 Experimental Method

For the measurements of N_2^+ we have applied a coincidence 3D-momentum imaging method (described in Section 2.2.2) and used previously for the study of the single electron systems, H_2^+, HD^+, and D_2^+ [64, 81], and other many-electron systems, e.g. O_2^+ [85] and ND^+ [86]. As in previous studies using the longitudinal field (Section 2.2.2), the fragment ions and neutrals are separated in time of flight and dissociation (N^++N) is clearly distinguished from ionization (N^++N^+), as illustrated using coincidence TOF spectra in Fig. 4.1. From the position and time information recorded for both fragments, the complete 3D kinematics of the breakup events are computed[3].

The laser used in the experiment is described in Section 2.4. The ultrashort pulses (linearly polarized 7 fs (FWHM)) are focused onto the ion beam target such that the peak intensity of 6.0×10^{15} W/cm^2 is achieved. Lower intensities (for example 6.5×10^{14} W/cm^2) are achieved by using the intensity selective scan [82, 113] technique, *i.e.* by moving the laser focus away from the ion beam center along the laser propagation direction.

The N_2^+ beam target used in these studies has some unique properties. The most important one is that it is predominantly in its electronic ground state and vibrationally cold. This follows since the ground state of N_2^+ (2.13 a.u. [118]) has a similar equilibrium distance as that of N_2 (2.08 a.u. [114]), hence there is a large Franck-Condon overlap of the ground vibrational state of N_2 with the low vibrational states of N_2^+. For the N_2^+ ions produced in an ion source by electron impact ionization of N_2 (*i.e.* a vertical transition), most of the population is distributed among the three lowest electronic states, namely, the ground state $X\,^2\Sigma_g^+$ and the metastable states $A\,^2\Pi_u$, and $B\,^2\Sigma_u^+$ [119–121]. These states are shown in Fig. 4.2(a) along with some additional relevant PECs of N_2^{q+} with $q\leq2$. The radiative lifetime of the different vibrational levels of the N_2^+ metastable states are a few tens of microseconds for the $A\,^2\Pi_u$ and a few nanoseconds for the $B\,^2\Sigma_u^+$ [122]. So, the electronic and vibrational population distributions change from when the ions are first produced in

[3]For ionization, information on the momentum of the ejected electron is lost.

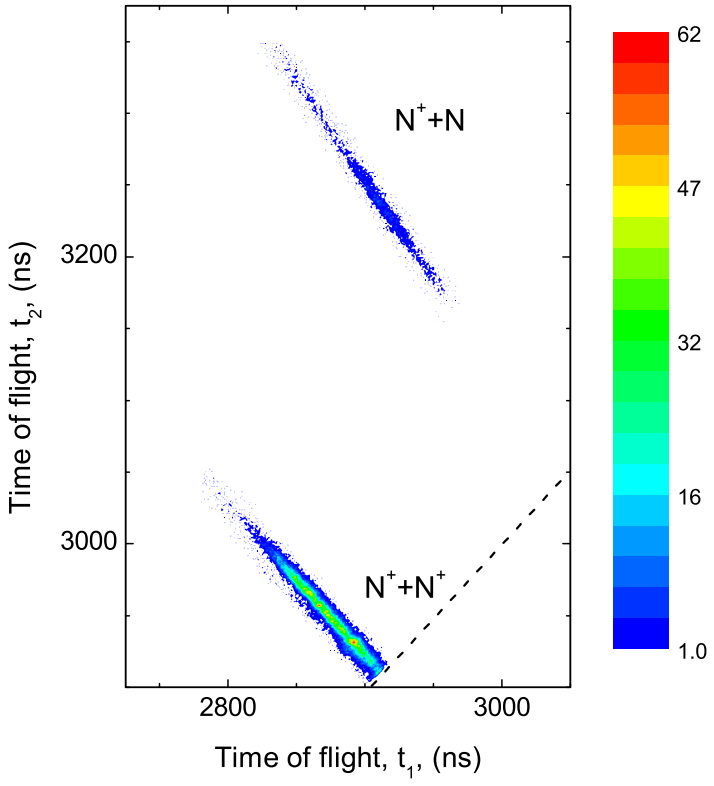

Figure 4.1: *A density plot of the time of flight of the first particle (t_1) to arrive at the detector against that of the second particle (t_2), to illustrate the separation of breakup channels in our coincidence measurement. The dashed line indicates the loci t_1=t_2. Figure adopted from Ref. [38].*

the ion source to when they reach the interaction region, *i.e.* after the transit time of about 20 μs in our set up. We have calculated the overall vibrational population distribution at the interaction region by applying the method described by Crandall *et al.* [120] and using the data from Refs. [120, 122]. The resulting electronic and vibrational populations of the ions in the interaction region are shown in Fig. 4.2(b). At the interaction time, the ground vibrational level (v=0) of the $X\,^2\Sigma_g^+$ state is most highly populated (>40%), with little population remaining in the $A\,^2\Pi_u$ state (total population <13%) and virtually no population in the $B\,^2\Sigma_u^+$ state. Furthermore, more than (83%) of the population is in v=0–7 of $X\,^2\Sigma_g^+$, *i.e.* within less than one photon energy from the bottom of the potential well.

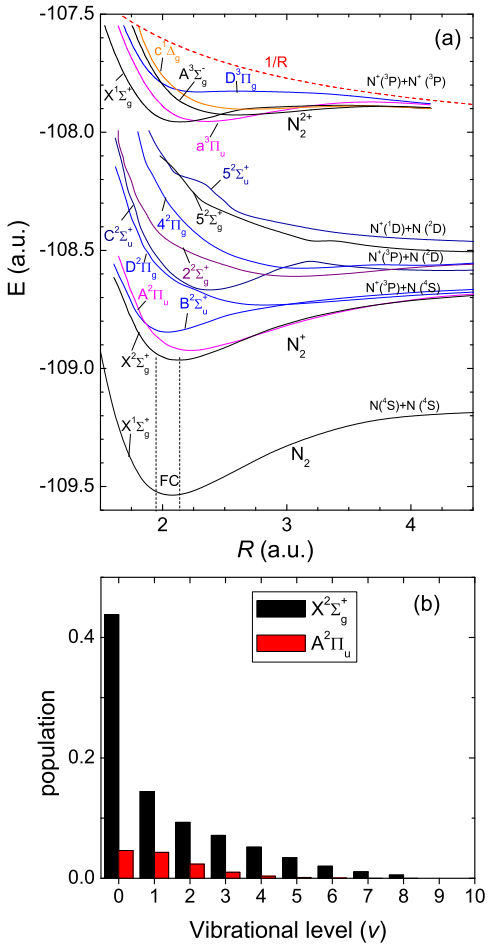

Figure 4.2: *(a) A simplified potential energy curve diagram of N_2^{q+} ($q \leq 2$) showing only a selection of the lowest-lying curves for each q. The PEC of N_2 is taken from Ref. [114], N_2^+ from Ref. [115, 116], and N_2^{2+} from Ref. [117]. The structure in some of these curves is due to avoided crossings with neighboring electronic states not shown. The dashed vertical lines represent the Franck-Condon (FC) transition region. The zero of the energy is for the fully stripped $N^{7+} + N^{7+} + 14e^-$ limit. (b) Calculated vibrational population distribution of N_2^+ in the interaction region following decay of metastable states from the source (see text). Figure adopted from Ref. [38].*

4.3 Dissociation

The KER distributions for the N_2^+ dissociation into the $N^+ + N$ channel (often referred to as the (1,0) channel) are displayed in Fig. 4.3. For the lower measured intensity of 6.5×10^{14} W/cm^2 (see panel (a)) the results display a sole low energy peak centered around 0.6 eV which extends up to ~2.5 eV. This peak is equivalent to that observed in other

studies of N_2^+ dissociation starting with an N_2 target [72, 74, 79, 111]. In contrast to our work, however, some of these papers report distributions peaked around 0.0 eV (for 25 fs, 10^{14} W/cm^2 pulses) [111], 1.2 eV (for 33 fs, 10^{15} W/cm^2 pulses) [74], 1.8 eV (for 55 fs, $\sim 10^{16}$ W/cm^2 pulses) [72], and 0.45 eV (for 70 fs, $\sim 10^{14}$ W/cm^2 pulses) [79]. The reason for these differences is unclear and further investigation is required.

By comparison, the KER spectrum measured under the same experimental conditions as Fig. 4.3(a) but for a higher intensity of 6.0×10^{15} W/cm^2, shown in panel (b), exhibits an additional KER peak around 6.1 eV. Such a high-KER feature is rather surprising for the dissociation of diatomic molecules like N_2^+ and, to the best of our knowledge, has not been reported previously. It is important to note that in many previous studies only charged fragments were detected so that the breakup channels (*i.e.* $N^+ + N$, $N^+ + N^+$, etc.) were identified only by the KER. Therefore, high KER in $N^+ + N$ dissociation could be masked by the energetic $N^+ + N^+$ breakup. This limitation is not a problem in our method because the different breakup channels are separated through detection of both the charged and neutral fragments in coincidence as shown in Fig. 4.1 and discussed in Section 2.2.2.

Additional information on dissociation is provided by the angular distribution of the fragments as displayed in the cosθ plots in the insets of Fig. 4.3 for the two different intensities discussed above. The type of the transition involved in a dissociation pathway can be found by the change in the projection of the angular momentum quantum number along the nuclear axis, $\Delta\Lambda$ [85, 86, 123]. A parallel transition is defined by $\Delta\Lambda=0$ (e.g. $\Sigma\leftrightarrow\Sigma$, $\Pi\leftrightarrow\Pi$) and depends on the laser field strength parallel to the molecular axis, while a perpendicular transition corresponds to $\Delta\Lambda=\pm1$ (e.g. $\Sigma\leftrightarrow\Pi$, $\Pi\leftrightarrow\Delta$) and depends on the laser field strength perpendicular to the molecular axis. To account for the volume element of the dissociation sphere, we bin the angular distributions as a function of cosθ rather than θ such that an isotropic angular distribution will appear flat on a cosθ plot. We see in the insets of Fig. 4.3 that the $|\cos\theta|$ distributions have significant counts along $|\cos\theta|=0$, in addition to the major contribution along $|\cos\theta|=1$. This implies that, in addition to the

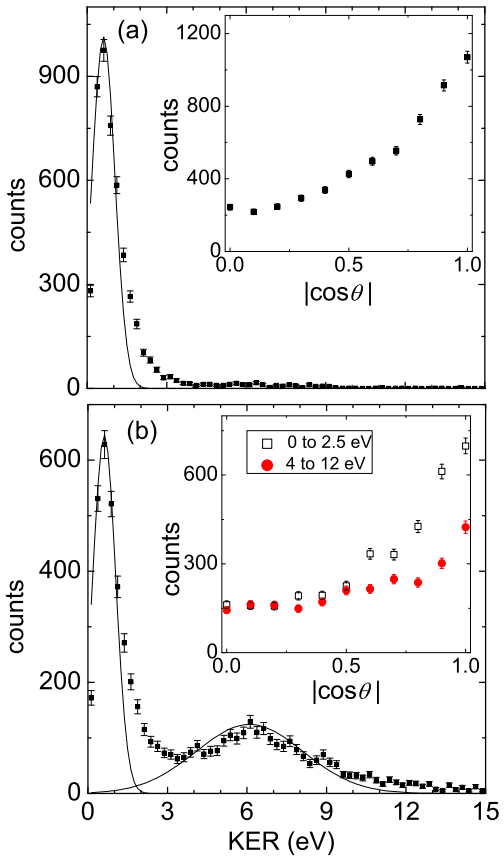

Figure 4.3: *(a-b) Measured KER distributions for dissociation of N_2^+ using 7fs pulses at intensities (a) 6.5×10^{14} W/cm^2, and (b) 6.0×10^{15} W/cm^2 with corresponding angular distributions (inset) plotted versus |cosθ|, where θ is the angle between the molecular breakup direction and the direction of the laser polarization. The error bars denote the statistical errors in the data. The fitted curves are Gaussian distributions centered at the peak of the measured KER distribution and are only used as a guide. Figure adopted from Ref. [38].*

dominant parallel transitions, perpendicular transitions also play an important role in the dissociation.

Below we discuss the most probable pathways leading to the low and high KER in the dissociation.

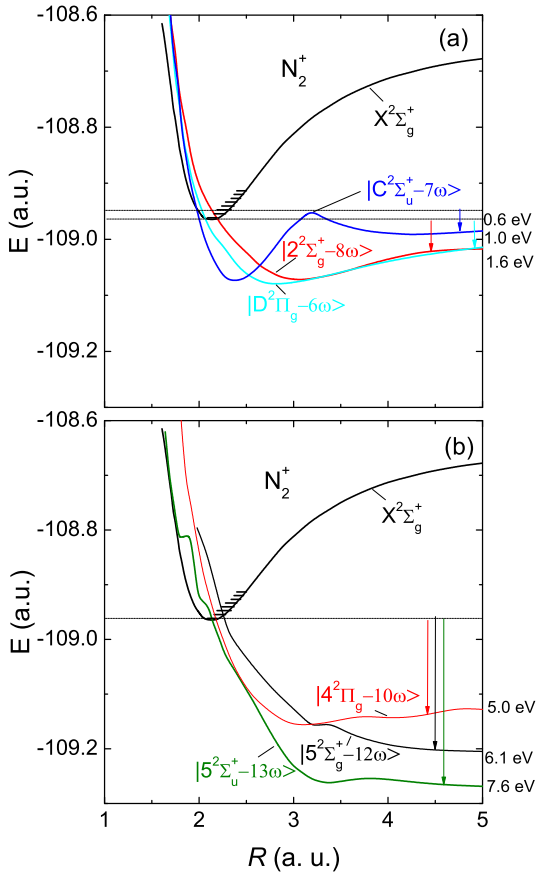

Figure 4.4: *Dressed-states diabatic picture of N_2^+ illustrating dissociation pathways that lead to (a) low- and (b) high-KER dissociation (see text). The short lines within the potential well represent the different vibrational levels and the horizontal lines near the bottom of the potential represent the initial energy of the dissociation wavepacket. Potential energy curves for N_2^+ have been reproduced from Ref. [116]. The structure in some of these curves is due to avoided crossings with neighboring electronic states not shown. Figure adopted from Ref. [38].*

4.3.1 Low-KER dissociation pathway

The mechanisms or pathways responsible for the KER and $|\cos\theta|$ features observed may be determined from close inspection of the PECs of N_2^+. We begin by focusing on the origin of the low-KER peak, which we identify as being produced by dissociation along one of the pathways shown in Fig. 4.4(a). By process of elimination of all other allowed dissociation paths based on the expected KER and angular distributions (see Ref. [85] for the method

used), we find the following pathways to be the important ones.

The ground vibrational level of the $|\mathrm{X}\,^2\Sigma_g^+ - 0\omega>$ state couples to the $|\mathrm{D}\,^2\Pi_g - 6\omega>$ state, dissociating to $\mathrm{N}^+(^3P)$+$\mathrm{N}(^4S)$. It is a valid even-photon gerade-gerade coupling resulting in a perpendicular transition ($\Sigma \rightarrow \Pi$) and is thus likely to be the source of the counts near $|\cos\theta|$=0 in the inset of Fig. 4.3(a). Dissociation along this path yields a KER of about 1 eV, estimated from the difference between the initial energy of the molecule and the asymptotic dissociation limit. Note, there may be a small deviation from this value due to possible Stark shifting of vibrational states, depending on the intensity. Since the main peak of the low-KER feature in Fig. 4.3(a) is at lower energy than that given by this pathway (*i.e.* this pathway contributes to the extended tail of the distribution), we look for other pathways for dissociation involving excited final products.

One strong possibility for a dissociation pathway is that the population of the N_2^+ $|\mathrm{X}\,^2\Sigma_g^+ - 0\omega>$ state near v=2 couples to the dressed $|\mathrm{C}\,^2\Sigma_u^+ - 7\omega>$ excited state, dissociating to the $\mathrm{N}^+(^3P)$+$\mathrm{N}(^2D)$ limit. This pathway involves a parallel transition with an odd number of photons absorbed, resulting from a gerade-ungerade coupling. One will notice that there is a barrier in this state at an internuclear distance, R, of about 3.2 a.u., but a wavepacket dissociating from the v=2 state should just have enough energy to overcome this barrier and will end up with dissociation energy of 0.6 eV in good agreement with the peak of the observed distribution. Note that approximately 10% of the total fraction of the beam is in the v=2 vibrational level.

One other state, namely $|2\,^2\Sigma_g^+ - 8\omega>$, dissociating to the same limit as the $\mathrm{C}\,^2\Sigma_u^+$ state, may also contribute in a similar way by accessing population in the v=0 level to yield a KER of about 1.6 eV. This pathway, like the $|\mathrm{D}\,^2\Pi_g - 6\omega>$ pathway, acts to extend the main KER peak to higher energies.

4.3.2 High-KER dissociation pathway

We now turn our attention to the unexpected high-KER feature in Fig. 4.3(b). This peak results from dissociation mechanisms similar to the low-KER peak but involving other pathways along which more photons are absorbed. As more photons are required, this peak is significant only at the higher intensity. Like the low-KER peak it involves electronic states leading to the $N^+(^3P)$+$N(^2D)$ dissociation limit. Additionally, it involves excited states from the next higher manifold leading to dissociation into $N^+(^1D)$+$N(^2D)$.

A few examples of such highly excited states that lead to high KER, namely the $|4\,^2\Pi_g - 10\omega>$, $|5\,^2\Sigma_g^+ - 12\omega>$ and $|5\,^2\Sigma_u^+ - 13\omega>$, are shown in Fig. 4.4(b). We note, however, that there are a number of other states that similarly can contribute to KER in the observed range but have been omitted from the figure for clarity. The combined contribution from all of these states will yield the broad measured peak centered around 6.1 eV, as shown in Fig. 4.3(b). Close inspection of Fig. 4.3(b) also reveals that there are hints of structure in the high-KER peak[4]. This would indeed suggest that more than one pathway is involved in this peak.

Considering the angular distribution (Fig. 4.3(b)), we again see contributions from both parallel and perpendicular transitions indicating that both ($\Sigma\rightarrow\Sigma$) and ($\Sigma\rightarrow\Pi$) transitions are involved. In this case, while the parallel transitions continue to dominate like for the low-KER peak, the relative contribution from perpendicular pathways is larger (see Fig. 4.3(b)) as the ratio of counts at $|\cos\theta|$=0 to $|\cos\theta|$=1 is larger for KER in the range 4–12 eV than for KER in the range 0–2.5 eV.

It is important to emphasize that the higher KER from dissociation along the pathways shown in Fig. 4.4(b) is due to the steep part of the repulsive potentials in the vicinity of their crossing with the ground state. Therefore, we find that there are two subsets of groups of PECs that lead to dissociation: low-lying shallow potentials that lead to low

[4]The structure in the high-KER dissociation peak [Fig. 4.3(b)] seems to be reproducible when the experiment is repeated under similar conditions.

KER, and higher-lying steep potentials that lead to high KER in dissociation. The low-lying potentials have a shallow potential well at an internuclear distance, R, slightly greater than the equilibrium distance (R_0) and cross the highly populated region of the N_2^+ potential well when dressed by 6–8 photons. A few examples of such shallow PECs are shown in Fig. 4.4(a). The higher-lying potentials are more repulsive and when dressed downwards require more photon absorption to reach the bottom of the N_2^+ potential well than the low-lying shallow potentials. We refer to these states as steeper PECs and a few of them are shown in Fig. 4.4(b).

The highly excited electronic states associated with the removal of an inner valence electron are steeper than the lower-lying electronic states because of the reduced screening of the nuclear potential. This is made clearer by considering the electronic configurations of N_2 and N_2^+. The ground state of N_2, $X\,^1\Sigma_g^+$, is $(1\sigma_g)^2\ (1\sigma_u)^2\ (2\sigma_g)^2\ (2\sigma_u)^2\ (1\pi_u)^4\ (3\sigma_g)^2$ and that of N_2^+, $X\,^2\Sigma_g^+$, is $[...(1\pi_u)^4\ (3\sigma_g)^1]$, *i.e.* to form N_2^+ one electron is removed from the $(3\sigma_g)$ orbital of N_2. When the laser excites a shallow PEC of N_2^+, it is the outer valence electron that is excited. For example, for excitation to the shallow $D\,^2\Pi_g$ state of N_2^+, the electron from the $(3\sigma_g)$ orbital is excited to the $(1\pi_g)$ orbital to result in $[...(1\pi_u)^4\ (3\sigma_g)^0\ (1\pi_g)^1]$. However, when the laser excites one of the steeper PECs, it is an inner valence electron that gets excited to an outer orbital, e.g. for excitation of the steep $5\,^2\Sigma_g^+$ state, predominantly a $(2\sigma_g)$ electron is excited to the $(1\pi_g)$ orbital [116, 124, 125].

Finally, before proceeding, it is interesting to note that the large number of photons required to dissociate N_2^+ (6–13 photons) is reflected in the measured dissociation rates. For example, at $6.0\times10^{15}\,\mathrm{W/cm^2}$ the dissociation rate of N_2^+ is about a factor of two lower than O_2^+ under similar ion and laser beam conditions, where for O_2^+ the dominant dissociation paths require 1–4 photons [85]. Likewise, the dissociation rate is approximately a factor of 20 lower than H_2^+ which requires only 1–2 photons to dissociate [30]. Hence, one observes directly a link between the large multiphoton nature of the dissociation pathways we have identified and the difficulty in dissociating N_2^+ in an intense laser field. We note, given the

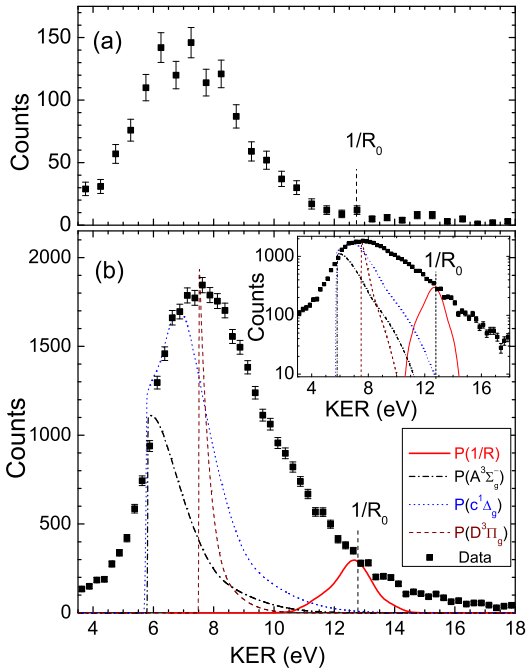

Figure 4.5: *Measured KER distributions for ionization of N_2^+ using 7fs pulses at intensities (a) 6.5×10^{14} W/cm^2 and (b) 6.0×10^{15} W/cm^2. Note that at higher intensity the KER has a high energy tail. The error bars denote the statistical error in the data. A sample of computed probability distributions (arbitrary yields) expected for direct ionization to the $c\,^1\Delta_g$ (dotted curve), $D^3\Pi_g$ (dashed curve), $A\,^3\Sigma_g^-$ (dash-dotted curve) states of N_2^{2+}, and the Coulomb curve 1/R (solid curve) are also shown. The dashed vertical lines (labeled 1/R$_0$) indicate the energy corresponding to "Coulomb explosion" of N_2^+ at R=R$_0$. Figure adopted from Ref. [38].*

large difference in the number of photons needed to dissociate, one may have expected an even larger difference in the dissociation rates, although this may be due to the onset of saturation of certain dissociation pathways at this high intensity.

4.4 Ionization

In addition to dissociation, we have also measured the (1,1) and (1,2) ionization channels of N_2^+. Here we focus on the (1,1) channel *i.e.* the $N^+ + N^+$ channel. For our measurement of KER at 6.5×10^{14} W/cm^2, shown in Fig. 4.5(a), we observe a KER peak centered around 7 eV with a width of about 4 eV. The peak of the distribution is comparable to the KER

value measured in the majority of studies starting with N_2, using both similar [78] and longer [33, 50, 72, 74, 79, 110–112] pulse durations.

4.4.1 Low-KER ionization pathway

There are two possible mechanisms that could lead to KER in the range of 6–11 eV. The first is what is commonly referred to as *direct* ionization, and is particularly amenable to the use of short intense pulses [60, 61]. Here a wavepacket from N_2^+ is launched directly onto the N_2^{2+} manifold of states from where it then dissociates. As a zeroth order approximation, one typically estimates the KER from such a process as given by $1/R_0$ arising from pure Coulomb explosion of the product fragments from the molecule's equilibrium internuclear separation. This energy in the case of N_2^+ is marked by the dashed vertical line labeled $1/R_0$ in Fig. 4.5(a). The spread of initial internuclear distance, $P(R)$, computed using the phase-amplitude method [126] for the vibrational population of the N_2^+ beam at the interaction point (see Fig. 4.2(b)), results in a KER spread around $1/R_0$ after reflection [127, 128] of $P(R)$ onto the $1/R$ Coulomb potential, as shown in Fig. 4.5(b) by a solid curve. However, in contrast to the transient H_2^{2+} where the $1/R$ Coulomb potential is accurate, the low-lying states of N_2^{2+} have mostly shallow bound-shaped potentials in the direct ionization region (as seen in Fig. 4.2(a)). They lie well below the $1/R$ Coulomb curve and would, therefore, yield lower KER than expected for Coulomb explosion.

We have projected the expected N_2^+ vibrational population for the $X\,^2\Sigma_g^+$ and $A\,^2\Pi_u$ initial electronic states (given in Fig. 4.2(b) for the interaction time) onto a few low-lying states of N_2^{2+}, one of which was found to be the most probable by Voss *et al.* [78]. The results of the reflection are shown in Fig. 4.5(b). It can be seen that this leads to KER values in the 6–11 eV range. One may expect the innermost turning point of the highly excited vibrational states to yield high KER values. However, even the highest vibrational level shown in Fig. 4.2(b) does not lead to energetic enough breakup. Furthermore, highly excited vibrational states represent a small fraction of the initial vibrational population. It is important to note

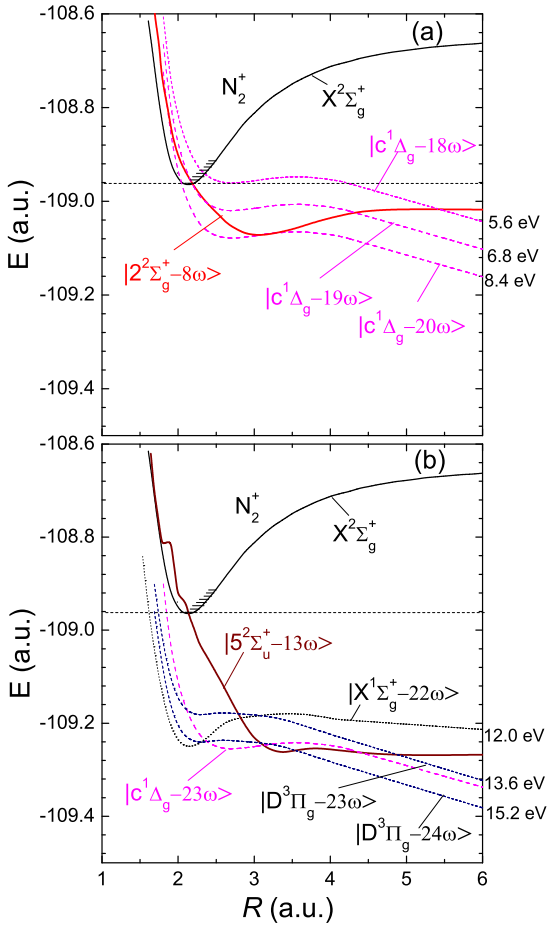

Figure 4.6: *Dressed-states picture of N_2^+ incorporating both dissociation (solid) and ionization (broken) curves that illustrate the dissociative ionization pathways that lead to (a) low- and (b) high-KER in ionization (see text). Potential energy curves for N_2^+ have been reproduced from Ref. [116]. The structure in some of these curves is due to avoided crossings with neighboring electronic states not shown. Figure adopted from Ref. [38].*

that the measured KER distribution at the higher intensity (6.0×10^{15} W/cm^2), shown in Fig. 4.5(b), extends to much higher values than expected for direct ionization.

In addition to direct ionization, however, there is also the possibility of *indirect* ionization. In this process the molecular wavepacket first begins to dissociate along one of the N_2^+ dissociation paths and is then ionized onto the N_2^{2+} states at internuclear distance R larger than R_0. Such a mechanism is usually invoked to explain KER lower than that expected for direct ionization as the ionization step occurs for stretched molecules experiencing a less repulsive potential. Below we will explain the mechanism of indirect ionization by choosing

one of the dissociation pathways described earlier.

As we have already identified the likely dissociation pathways, we select the $|2\,^2\Sigma_g^+ - 8\omega>$ state to illustrate one example of a possible indirect ionization pathway. Such a pathway is illustrated in Fig. 4.6(a) where, in addition to the relevant dressed dissociation states, we dress also the ionization states using the same representation introduced recently to discuss the above-threshold Coulomb explosion of H_2^+ [34]. In Fig. 4.6(a), a wavepacket dissociating on the $|2\,^2\Sigma_g^+ - 8\omega>$ curve may cross onto the dressed $|c\,^1\Delta_g - 19\omega>$ or $|c\,^1\Delta_g - 20\omega>$ states at R=2.4 a.u. or R=3 a.u., respectively, giving KER in the approximate range 6.5 – 8.5 eV. Here we have not included the $|c\,^1\Delta_g - 18\omega>$ state because the crossing between the $|c\,^1\Delta_g - 18\omega>$ and the $|2\,^2\Sigma_g^+ - 8\omega>$ state is at large R such that the electric field of the short laser pulse, used in this experiment, will be weak when the dissociating wavepacket reaches the crossing. Also, the $|c\,^1\Delta_g - 21\omega>$ state is not included because it does not cross the shallower PECs of N_2^+ that give the low KER, however, it crosses the steeper PECs of N_2^+ that result in high KER. As there is a large density of accessible N_2^{2+} states (see Fig. 4.2(a)) leading to the same $N^+(^3P)$+$N^+(^3P)$ dissociation limit as the $c\,^1\Delta_g$ state, each of these may contribute slightly different KER values resulting in a broadening of the observed KER distribution. In addition, as discussed in the introduction, the further the intensity is above the ionization appearance threshold, the more KER broadening incurred.

We have estimated classically the time it takes a dissociating N_2^+ wavepacket on the $|2\,^2\Sigma_g^+ - 8\omega>$ state to reach the crossing with the $|c\,^1\Delta_g - 20\omega>$ state of N_2^{2+} at R∼3.0 a.u. and found it to be around 7 fs, which for dissociation initiated on the leading edge of the laser pulse, is within the duration of the pulse. Similarly, the time that it takes for a dissociating wavepacket to reach the crossings between the $|2\,^2\Sigma_g^+ - 8\omega>$ state of N_2^+ and some other dressed states of N_2^{2+} at R∼(2.5–3.0) a.u. is about 5–7 fs. Thus, both of the aforementioned direct and indirect ionization pathways lead to KER in similar ranges and so we are not able to distinguish here between their contributions.

4.4.2 High-KER ionization pathway

In contrast to the low intensity measurement, the KER spectrum for the higher intensity of $6.0\times10^{15}\,\mathrm{W/cm^2}$ exhibits a much higher KER tail (see Fig. 4.5(b)). The fact that the KER distribution extends to higher values than that for low intensities and gets broader with increasing intensity is commonly observed [74]. However, it is surprising that the KER extends well beyond the purely Coulomb explosion energy of 12.8 eV (vertical dashed line, $1/R_0$) and even beyond the whole distribution resulting from the reflection of initial $P(R)$, shown by a solid curve centered around this line. Indeed, the N_2^{2+} states (mostly metastable) are less repulsive than the $1/R$ Coulomb curve for small R, predicting KER below 11 eV. In Fig. 4.5(b) we have shown a few possible distributions resulting from reflection of the N_2^+ vibrational population (as shown in Fig. 4.2(b)) onto the N_2^{2+} states, for states resulting in the extreme KER values. Clearly the high energy tail of the distribution extending beyond 11 eV can not be explained with direct ionization.

Further insight into the source of the high KER can be found by revisiting the indirect ionization concept. Although typically this has been used to explain lower KER than for direct ionization, as we found from the dissociation spectra, there is a group of extremely steep dissociation curves. Initiating dissociation onto these states, followed then by delayed ionization, can inject energy into the fragments in the first dissociation step. A few examples of such pathways are illustrated in Fig. 4.6(b). Here we consider dissociation on the steep $|5\,^2\Sigma_u^+ - 13\omega>$ curve. This state first forms a crossing with the dressed $|\mathrm{D}\,^3\Pi_g - 23\omega>$ state of N_2^{2+} at R=2.7 a.u., or alternatively with the $|\mathrm{D}\,^3\Pi_g - 24\omega>$ state at R=3.0 a.u.. The $|\mathrm{c}\,^1\Delta_g - 23\omega>$ state likewise forms a crossing at R=3.0 a.u. and the wavepacket can end up in the ionization curve by giving up an energy that contributes to the high-KER tail of the energy distribution.

The estimated time for a dissociating N_2^+ wavepacket on the $|5\,^2\Sigma_u^+ - 13\omega>$ state to reach the crossing with the $|\mathrm{c}\,^1\Delta_g - 23\omega>$ state of N_2^{2+} at R=3.0 a.u. is on the order of 6 fs, which can be considered accessible within the duration of the pulse. For the other crossings

around R=2.7–3.0 a.u. that are formed between the $|5\,^2\Sigma_u^+ - 13\omega>$ state of N_2^+ and some dressed states of N_2^{2+}, the estimated time is similarly about 5–6 fs.

Each of the pathways discussed above will lead to KER>12 eV, seemingly explaining the origin of the high-KER tail of the distribution in Fig. 4.5(b). We note that while we have chosen a few specific examples to demonstrate the mechanism responsible for the high-KER tail, there are a number of other similar routes giving a similar range of KER thus preventing the identification of the dominant one.

Finally, we remark on some similarities and differences observed between this experiment on N_2^+ and another recent momentum-imaging experiment on N_2 by Voss *et al.* [78]. At low intensity (10^{14} W/cm^2), notably below the lowest applied here, Voss *et al.* observed the dominant formation path of N_2^{2+} to involve: tunneling single ionization, followed by electron-rescattering excitation to highly-excited states of N_2^+, which rapidly tunnel ionize to excited N_2^{2+} prior to decaying. In our experiment such a pathway is immediately negated as, by starting from N_2^+, there is no recolliding electron to excite the N_2^+. In addition, at an intensity in the sequential ionization regime (1.2×10^{15} W/cm^2), Voss *et al.* found that the electron recollision step is replaced by a multiphoton process involving excitation of an inner shell electron, either of neutral N_2 or of the N_2^+ ion. In principle this excitation process appears similar to the one we observe leading directly to the high-KER peak in N_2^+ dissociation and also responsible for the high-KER in ionization. We note also the mixed use of terminology between the multiphoton and tunneling descriptions of Voss *et al.* [78]. It is generally accepted that neither regime should be strictly applied exclusively; the multiphoton picture works best for visualizing excitation steps [129] while tunneling is particularly useful to interpret electron-recollision processes [40] or field-enhanced ionization [62, 130].

4.5 Summary

We have presented the results of dissociation and ionization of N_2^+ in an intense ultrashort laser pulse using a coincidence 3D momentum imaging technique that has allowed us to completely separate the dissociation and ionization channels. We observe a surprising distinct peak in the dissociation with KER values larger than that typically expected for dissociation, which we have assigned to multiphoton excitation to a group of steep PECs from an excited N_2^+ manifold. In turn, indirect ionization following dissociation on these energetic states has led to large kinetic energy release in the $N^+ + N^+$ channel that exceeds the limit of pure Coulomb explosion and the KER expected from direct ionization. While the large density of excited N_2^+ and N_2^{2+} states has not allowed the exact assignment of dissociation pathways for these mechanisms, we wish to convey the counterintuitive concept that ionization of a stretched molecule (*i.e.* ionization along the dissociation path) can indeed increase the energy released from the system, rather than what is typically observed, to decrease it.

Chapter 5

Laser Induced Ionization of Molecules

In this chapter we discuss the dissociative and non-dissociative ionization of a few diatomic molecules (N_2^+, CO^+, NO^+, and O_2^+) in intense short and ultrashort laser pulses. For these multielectron molecules, when one of the electrons is ionized the molecule can either break into two pieces (referred to as dissociative ionization) or remain as a metastable dication (referred to as non-dissociative ionization).

We have studied dissociative ionization using the longitudinal field imaging (LFI) method discussed in Section 2.2.2. We find that multiple ionization states results in similar KER and angular distributions for all species under study. However, single ionization yields quite different energy distributions, except for the isoelectronic molecular ions N_2^+ and CO^+, which are similar in many respects. The measured multielectron dissociative ionization (MEDI) of these molecular ions suggests a fragmentation process that entails a stairstep mechanism which involves stretching the molecules prior to each sequential ionization step [84].

For non-dissociative ionization studies we have used the longitudinal and transverse field imaging (LATFI) method, discussed in Section 2.2.4, because the molecules of any energy-to-charge ratio other than the primary ion beam are pulled out of the Faraday cup with that method. This is an advantage over the LFI setup where all the molecular ions are collected in the Faraday cup. The non-dissociative ionization results also support the stairstep ionization mechanism as the ratio of the non-dissociative to dissociative ionization increases for shorter laser pulses.

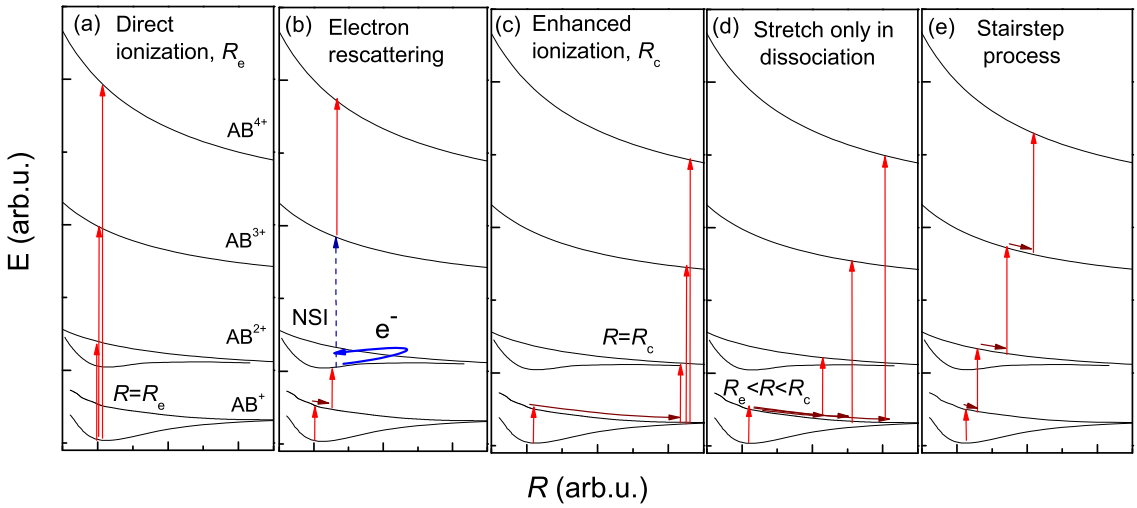

Figure 5.1: *Schematic diagrams illustrating the different mechanisms for the multiple ionization of a typical molecule, AB^+, in an intense laser field: (a) direct ionization, (b) electron rescattering (non-sequential ionization, NSI), (c) enhanced ionization, (d) stretch only in dissociation, and (e) stairstep process. For a discussion of the mechanisms refer to the text.*

5.1 Dissociative ionization

5.1.1 Introduction

The study of MEDI of diatomic molecules in ultrashort intense laser pulses enables us to better understand laser-driven molecular dynamics. Hence, it is an interesting area of research, as evidenced by the large number of studies, e.g. [9, 11, 33, 72, 79, 112, 131]. Various mechanisms including direct ionization [60, 61], electron-rescattering [40], and enhanced ionization [32, 62] have been introduced and established as possible explanations of multiple ionization and fragmentation pathways of molecules in strong fields. We have briefly introduced some of these mechanisms in Chapter 1 and they are also shown in Fig. 5.1.

MEDI of the ions used in the present study has been explored in the past by other groups using a number of experimental techniques and different forms of targets, mostly neutral gas molecules in an intense laser field. Common experimental methods in use by other groups are time-of-flight (TOF) mass spectrometry [53, 72–75], covariance mapping [76], mass-

resolved momentum imaging (MRMI) [77], cold-target recoil ion momentum spectroscopy (COLTRIMS) [78], and velocity-map imaging (VMI) [79]. As mentioned in Chapter 2, our experimental technique differs from the ones that use neutral gas targets. We use molecular ions produced in an ion source as targets and a coincidence 3D momentum imaging technique that allows us to detect both the neutral and ionic fragments. The detection of the neutrals is made possible by the initial beam velocity of the molecular ion targets. This is crucial for the coincidence measurements of dissociation ($AB^+ \rightarrow A^+ + B$ or $A + B^+$) and charge-asymmetric breakup of dications in single ionization (e.g. $AB^+ \rightarrow AB^{2+} + e^- \rightarrow A^{2+} + B + e^-$). In terms of laser parameters, the central wavelength used in our studies is similar to the other studies, however the pulse length differs slightly in some cases, e.g. for N_2^+ [50, 53, 72–74, 78, 79, 111, 112, 132, 133], for CO^+ [133–135], for NO^+ [75, 77, 134, 136–138], and for O_2^+ [73, 132, 133].

The general purpose of the MEDI studies is to use the variety of laser pulse parameters and find a way to manipulate the ionization of molecules.

5.1.2 Experimental method

We have used the LFI method (described in Section 2.2.2) with coincidence 3D-momentum imaging that allows the separation of neutral and ionic fragments with different mass-to-charge ratios (m/q) and, hence, allows us to distinguish dissociation from ionization and different ionization channels from each other. As an example, a coincidence time-of-flight map for the different breakup channels of CO^+ is shown in Fig. 5.2. Here all the fragmentation channels are cleanly separated. Fragmentation channels are referred to as (q_1,q_2). For homonuclear molecules, q_1 and q_2 are the charges of the fast and slow moving ions. For example, double ionization of N_2^+ leading to $N^{2+} + N^+$ is denoted as (2,1). However, for heteronuclear molecules q_1 and q_2 are the charges of the less and more massive fragments, respectively. The double ionization of CO^+ leading to $C^{2+} + O^+$ is referred to as the (2,1) channel and $C^+ + O^{2+}$ is referred to as the (1,2) channel.

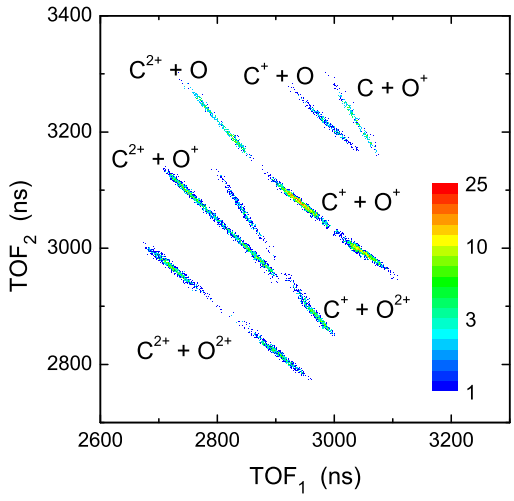

Figure 5.2: *Coincidence time-of-flight density plot showing the TOF of the particle with the smaller m/q value (TOF_1) plotted against that of the particle with the larger m/q value (TOF_2), from the fragmentation of CO^+ in 40 fs, 7×10^{15} W/cm^2 pulses. We plot the data after momentum conservation in order to present only true two-body breakup events. The plot shows that all the breakup channels observed in our measurement are clearly distinguished from each other, including those involving a neutral fragment. Figure taken from publication [84].*

5.1.3 Results and discussion

We have measured the KER and the angular distributions for the different breakup channels of N_2^+, CO^+, NO^+, and O_2^+ using short (40 fs) and ultrashort (7 fs), 790 nm laser pulses for several intensities up to 7×10^{15} W/cm^2. We have observed more breakup channels in the short pulse compared to the ultrashort pulse measurements, so we begin with the short pulse results.

Short pulse: 40 fs

The data for 40 fs at 7×10^{15} W/cm^2 is displayed in Fig. 5.3. We choose to present data as KER-cosθ density plots shown in the upper panels (a–d) so that we can compare one breakup channel with another and also compare different species. One dimensional KER distributions, obtained by integrating over all the angles, are shown in the lower panels (e). By surveying the spectra shown in Fig. 5.3 as a whole, we can make a few general

statements.

First, comparing dissociation (Fig. 5.3(i)) between the different molecules, there are features that look quite different for each of the species except for isoelectronic N_2^+ and CO^+. In other words, the dissociation is molecule specific. Second, in single ionization (Fig. 5.3(ii)) structures in KER are different for each species. Some aspects of the spectra are remarkably similar however, such as a narrowly aligned ridge with a broader base in the angular distribution. Finally, in multiple ionization (Fig. 5.3(iii) and (iv)), the structures in KER disappear and all species start to resemble one another more closely. So, from dissociation to multiple ionization the molecules gradually lose their structural identity. We will present an explanation for the features observed.

The dissociation of N_2^+ and O_2^+ is denoted as (1,0) while for CO^+ and NO^+ it is denoted as (1,0) and (0,1). The KER and the angular distributions of N_2^+ and CO^+ look qualitatively similar. There is a low-KER peak around 1 eV and a weaker high-KER peak around 6 eV (shown in the inset of Fig. 5.3 (i)(e)). This double peak behavior is reminiscent of our earlier measurements for N_2^+ with $\sim$7 fs pulses [38] and is also discussed in Chapter 4. There we identified the low-KER peak as arising from dissociation via low-lying electronic states that are shallow in potential energy (similar to observations by other groups [72, 74, 111]). They are shallow in the sense that the change in potential energy with respect to the internuclear distance R is small. In contrast, the high-KER peak was a newly observed feature coming from excitation of an inner-shell electron ($2\sigma_g$) leading to dissociation on steep high-lying electronic states, *i.e.* the change in potential energy with R is large. We believe the same mechanisms are valid for the 40 fs pulses used here. Since the N_2^+ and CO^+ ground states have the same electronic configurations, *i.e.* $1\sigma_g^2 1\sigma_u^2 2\sigma_g^2 2\sigma_u^2 1\pi_u^4 3\sigma_g^1$ for N_2^+, which is equivalent to $1\sigma^2 2\sigma^2 3\sigma^2 4\sigma^2 1\pi^4 5\sigma^1$ for CO^+, it is reasonable to expect that the equivalent inner-shell electron gets excited in CO^+ leading to its observed similarity to N_2^+.

The energy of the high-KER peak in the dissociation is in the range of KER from single ionization. This feature might be considered as coming from single ionization in

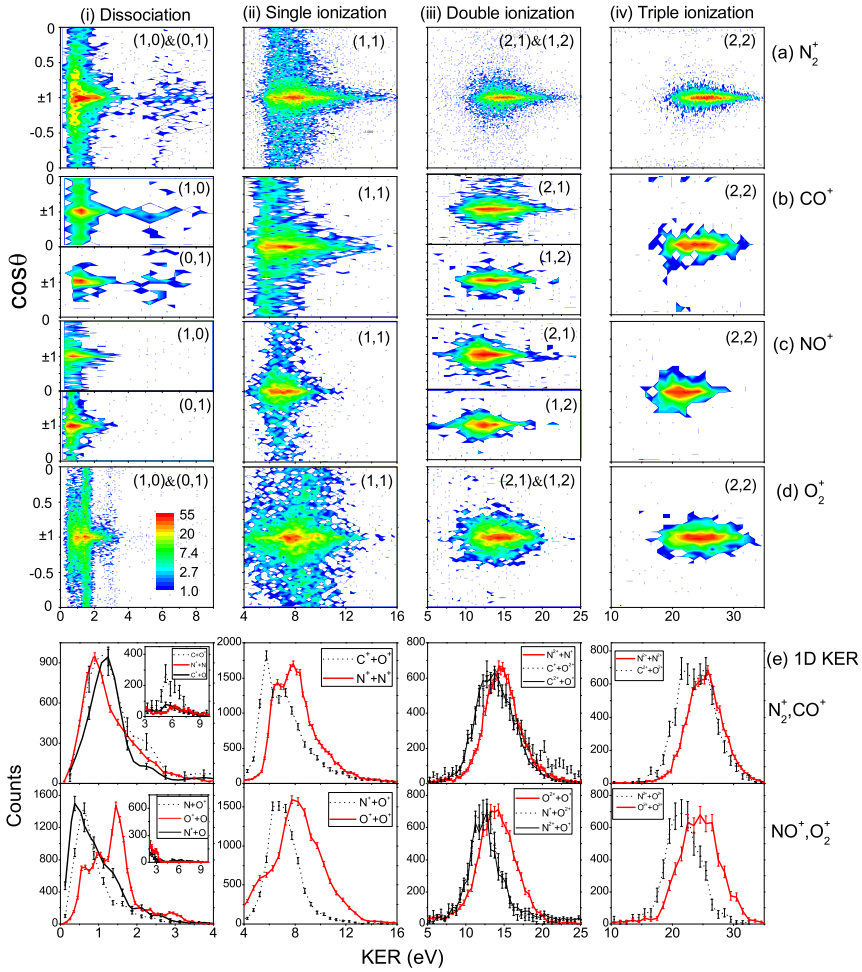

Figure 5.3: *The KER and angular distributions of the different fragmentation channels [(i) dissociation (1,0) and (0,1), (ii) single ionization (1,1), (iii) double ionization (2,1) and (1,2), and (iv) triple ionization (2,2)] of N_2^+, CO^+, NO^+, and O_2^+ for 40 fs, 7×10^{15} W/cm^2 pulses. The upper panels (a–d) are KER-cosθ plots with the same cosθ scale and the lower panels (e) are 1D KER plots, integrated for all angles. The error bars denote the statistical uncertainty in the data. The color scale is the same for all the density plots. Figure adopted from Ref. [84].*

the measurements that only detect ions and use the breakup energy for the identification of channels. That is why coincidence measurement of the fragments is important, as the channels are then separated clearly from each other.

O_2^+ and NO^+ dissociation are different from each other and also from N_2^+ and CO^+ dissociation. The KER and the angular distribution of the NO^+ dissociation have almost no structure. However, O_2^+ dissociation is rich in structure displaying multiple peaks below

$\sim$3 eV. This feature has also been observed in previous measurements using the LFI method [85] and in recent measurements using the LATFI method as briefly discussed in Chapter 2. The presence of structure in O_2^+ reflects the multitude of electronic states that can be accessed by the laser, giving many dissociation pathways. This observation emphasizes the fact that the dissociation is linked to the individual nature of the molecules' electronic potentials.

This assessment is supported by the angular distributions in Fig. 5.3(i). The transition between the electronic states of a molecule in the presence of a laser field provides some hints on the angular dependence of the breakup. Generally, the type of the dissociative transition is determined by the change in the projection along the molecular axis of the angular momentum quantum number $\Delta\Lambda$ of the states involved [85, 123]. A parallel transition corresponds to $\Delta\Lambda$=0 (e.g. $\Sigma\leftrightarrow\Sigma$, $\Pi\leftrightarrow\Pi$), leading to a $\cos^{2n}\theta$ distribution, where n is the number of photons involved. A perpendicular transition corresponds to $\Delta\Lambda=\pm1$ (e.g. $\Sigma\leftrightarrow\Pi$), giving a $\sin^{2n}\theta$ distribution. The plots in Fig. 5.3 show that, for all molecules, one observes counts for both $\cos\theta$=0 and $\cos\theta=\pm1$ indicating the presence of both perpendicular and parallel transitions, respectively, with the parallel transitions dominating. The fact that both types of transitions are observed (and for some peaks a combination of both) shows that the individual nature of the molecules' electronic states plays a role in the molecular dissociation.

The single ionization, *i.e.* (1,1), channel of each molecule displays about the same range of KER. Even the angular distributions appear similar to some extent. We can see in Fig. 5.3(ii) a feature with broad angular distribution and a narrow feature aligned along the laser polarization. The reason for the observed shape of these distributions, however, can be complicated by several factors. According to the predictions of MO-ADK theory in the tunneling region, the angular distribution for the (1,1) channel reflects the symmetry of the most loosely bound electron orbital of the molecule [54]. For example, for the N_2^+ $X\,^2\Sigma_g^+$ ground state ($\ldots 1\pi_u^4 3\sigma_g^1$) the outermost orbital is σ_g and hence the distribution is

peaked along the laser polarization. For the O_2^+ $X\,^2\Pi_g$ ground state ($\ldots 3\sigma_g^2 1\pi_u^4 1\pi_g^1$), the outer electron is in a π_g orbital, and ionization is predicted to peak at $\sim$40° to the laser polarization [78]. But this is not the case in our measurements. The possible reason is that MO-ADK predictions work well for relatively low intensities in the tunneling ionization region. As described by Voss *et al.* [78], at high intensities in the sequential ionization regime as used here ($7\times10^{15}\,\mathrm{W/cm^2}$), the angular distribution will be influenced by other effects such as intermediate excitation processes. Indeed, Voss *et al.* observe a transition in the angular distribution of the O_2^+ (1,1) channel changing from peaking near 40° at $10^{14}\,\mathrm{W/cm^2}$ to strongly peaking at 0° at $10^{15}\,\mathrm{W/cm^2}$ (for 7 fs pulses). So our data at $7\times10^{15}\,\mathrm{W/cm^2}$ in Fig. 5.3 agrees with this alignment effect, since the dominant contribution to single ionization is strongly aligned for all molecules, irrespective of the initial electron orbital. This may also, at least partly, be due to dynamic alignment [52], where molecules rotate their internuclear axis toward the laser polarization during the pulse or more likely after the pulse [56, 57]. This is supported by comparison with 7 fs pulses (that we discuss later), which display a lower degree of alignment because the shorter pulse width does not allow the time needed for alignment.

The angular distribution with a broad base suggests fragmentation into the (1,1) channel perpendicular to the laser polarization. This is an indication of the stepwise mechanism for ionization. In other words, it is an effect that reflects some of the features of the dissociation, (1,0) and (0,1), channel. The molecular ion is excited to the dissociation state and then ionized. This is reflected in the angular distribution of the ionization, because both dissociation and ionization have a broad base and a narrower aligned feature.

The stepwise mechanism is further supported by the KER distribution. The N_2^+ and CO^+ ionization KER has a double peak structure because these ions have both low and high KER in dissociation. However, the energy separation of the peaks in ionization is smaller because only a fraction of the dissociation KER is imparted to fragments before ionization. In the case of NO^+ ionization only a single peak is observed, as in dissociation.

Likewise, the O_2^+ ionization (1,1) channel has a structured KER distribution, although it is not well resolved, as the dissociation (1,0) has multiple peaks. This could be explained by the presence of several peaks arising from the dissociation step. Viewed overall, we see some remarkable similarities between the (1,1) and the (1,0) and (0,1) channels. Hence we can link the KER peaks in the (1,1) channels qualitatively to the peaks in the (1,0) and (0,1) dissociation channels.

Multiple ionization, referring to double and triple ionization, of all these molecular ions shows similar behavior as displayed in Fig. 5.3 with double ionization in column (iii) and triple ionization in column (iv). The angular distribution is mostly peaked along the laser polarization with the exception of the N_2^+ and CO^+ (2,2) channels, which have a weak perpendicular component (see Fig. 5.4, to be discussed later). One can see the broad single peak in the KER distributions for all species. There are slight differences in the peak values which differ from molecule-to-molecule by up to 3 eV and 5 eV for double and triple ionization, respectively, and the KER widths which vary by a few eV. The similarity of the features for all species indicate that the electronic structure is less important. More specifically, the transient multiply-charged molecular states, e.g. CO^{3+}, become Coulomb-like ($q_1 q_2/R$) for stretched R [139], giving a first indication that the molecules stretch enroute to ionization in these channels.

With the features observed in our experimental results, we believe that multiple ionization can be explained using a stairstep mechanism, shown schematically in Fig. 5.1(e), that is similar to the mechanism used in some earlier studies to explain MEDI of neutral molecules [9]. Below we exclude other possible mechanisms.

Previously, one of the mechanisms suggested for multiple ionization was electron rescattering [40, 61, 140]. That is, an electron is ionized in a linearly polarized laser field and is driven back to collide with its parent molecular ion causing ionization, or excitation followed by field-ionization, of a secondary (or more) electron(s). A commonly used test to check if this process occurs is to compare linearly and circularly polarized light. In the latter case,

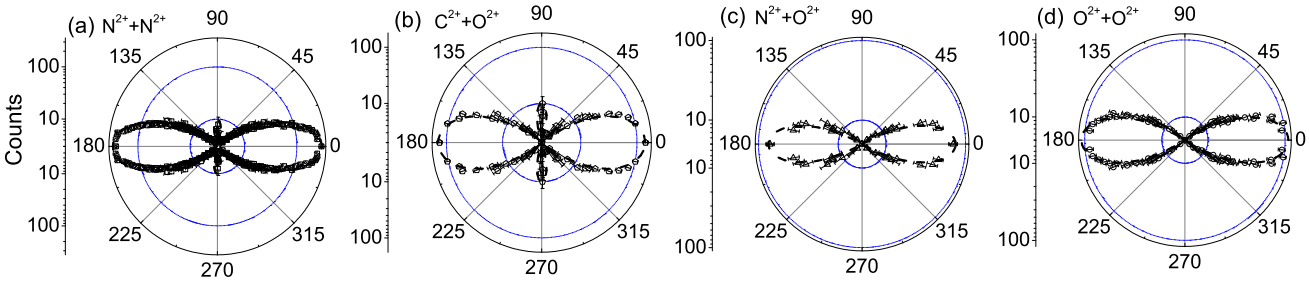

Figure 5.4: *Measured angular distributions (plotted on a log scale) for triple ionization (2,2) of (a) N_2^+ (fitted function $a{\cdot}\cos^{24}\theta{+}b{\cdot}\sin^{24}\theta$), (b) CO^+ (fitted function $a{\cdot}\cos^{18}\theta{+}b{\cdot}\sin^{30}\theta$), (c) NO^+ (fitted function $a{\cdot}\cos^{18}\theta$), and (d) O_2^+ (fitted function $a{\cdot}\cos^{18}\theta$), using 40 fs, $7{\times}10^{15}$ W/cm^2 pulses, integrated for all KER. The dotted lines are fitted functions. The error bars denote the statistical uncertainty in the data. The lower half of the data is mirrored from the upper half. Figure adapted from Ref. [84].*

the returning electron misses the parent ion due to a large transverse spread in momentum [40]. It is the electric field strength that matters for the comparison of the two polarization cases, so one must use linearly polarized light at half the power of the circularly polarized light. Therefore we have compared the multiple ionization yield using linearly polarized pulses at $3.5{\times}10^{15}$ W/cm^2 with circularly polarized pulses at $7{\times}10^{15}$ W/cm^2 and find no significant reduction in the yield for the circular polarization. Since electron rescattering becomes an even smaller effect at higher intensity (because higher intensity is further into the sequential ionization regime), we conclude that rescattering plays no major role for the spectra shown in Fig. 5.3 at $7{\times}10^{15}$ W/cm^2.

Another possible mechanism is "direct" ionization, *i.e.* the ionization happening at the equilibrium internuclear distance (R_e) of the molecule. When we use sufficiently short pulses, multiple ionization will occur rapidly such that the molecule does not have enough time to stretch between ionization stages, thus ionization is "direct". That is approximately a vertical transition for which $R{\sim}R_e$, shown schematically in Fig. 5.1(a). Since the multiply-charged molecular states are almost Coulomb-like, ionization at R_e will lead to

large KER from the Coulomb explosion of the fragments. For example, for double ionization of N_2^+ into N^{2+}+N^+, *i.e.* the (2,1) channel, direct ionization from R_e=2.13 a.u. would give KER=25.5 eV, but the observed KER is centered at 14 eV, which is much lower than the expected value from direct ionization. This suggests that direct ionization does not occur for these 40 fs pulses. Even using 7 fs pulses (see Fig. 5.5) the measured KER is peaked around 17 eV which is still much lower than the expected KER for direct ionization.

In contrast to the direct ionization mechanism, it has been suggested that molecules stretch on their dissociation potentials before ionizing [32, 62]. The signature of this mechanism would be a low KER compared to direct ionization. In particular, there is a predicted critical internuclear distance R_c, where the electron is localized on one of the two charged centers prior to being ionized and hence the ionization is enhanced. This mechanism is referred to as enhanced ionization. We have calculated R_c for all the species used in the current study using a classical model outlined in Ref. [33]. With the given ionization potential of the atoms for different levels of ionization, we find the appearance intensity for the ionization when the potential barrier is lowered for the stretched molecule. We denote this R as R_c. We find that the R_c value for the lowest ionization channels of N_2^+ is roughly ∼7.0 a.u., in agreement with the values in Refs. [33, 72, 141]. For CO^+ it is about 6.5–8.2 a.u., for NO^+ it is about 6.1–7.3 a.u., and for O_2^+ it is about 5.8–7.5 a.u.. Using the least extreme case, *i.e.* the smallest R_c value from the multiple ionization of the molecules considered in the present study, O_2^+, as an example, ionization on the (2,1) channel at R=5.8 a.u. would give an energy release of ∼9.4 eV, assuming a Coulomb potential. This, added to about 2 eV or less from dissociation, would give a KER value of just over 11 eV which is lower that the observed KER value, *i.e.* 14 eV for the O_2^+ (2,1) channel. This in turn suggests that the molecules do not stretch on the dissociation curve or on the parent molecular ion PEC as far as R_c before ionizing. The other molecular ions follow a similar trend.

So far we have ruled out electron rescattering, direct ionization at R_e, and enhanced multiple ionization at R_c, as mechanisms to explain multiple ionization. There remain only

a couple of options: (i) stretching only on the dissociation curve followed by ionization at $R_e < R < R_c$ (Fig. 5.1(d)) to the multiple charged states, or (ii) stretch and ionize, sequentially, a stairstep mechanism as illustrated in Fig. 5.1(e).

Option (i) seems unlikely on several grounds. First, one might expect the dissociation structures to be reflected in multiple ionization if multiple ionization steps were preceded directly by dissociation. However, the multiple ionization spectra (*i.e.* both KER and angular distributions) in Figure 5.3 do not resemble dissociation. But it is only the (1,1) channel that has some link to the dissociation structures. Second, stretching of molecules only on the dissociation PECs would require higher intensity to multiply ionize by stripping off one electron at a time, as the energy gap between the two PECs is large.

Considering these findings we are left with the stairstep mechanism where the molecule first stretches on the PECs leading to the (1,0) channel (or (0,1)), then ionizes, followed by stretching on the (1,1) PECs, then ionizing again, and so on, *i.e.* sequential ionization with molecular stretching in between. The data in Fig. 5.3 appear consistent with this mechanism. Since each subsequent ionization step occurs later in the pulse, the laser field has more time (and intensity) to populate a broad range of higher rotational J states which leads to the angular distributions gradually becoming more aligned for the higher ionization stages. Also, any structure in the KER that was present in the initial dissociative step gradually gets washed out over the course of the later ionization steps.

Using the change in KER from one ionization stage to the next we can get an estimate of the R values at which the ionization steps occur by using an expression

$$\mathrm{KER}_{(q_1,q_2)} = \mathrm{KER}_{(q_1,q_2-1)} + \frac{q_1 q_2}{R_{(q_1,q_2)}} - \frac{q_1(q_2-1)}{R_{(q_1,q_2)}},$$

where $R_{(q_1,q_2)}$ is the internuclear separation for the channel (q_1, q_2). For example, for N_2^+ multiple ionization we find that ionization to (2,2) occurs at R∼4.9 a.u. while for (2,1) it occurs at R∼3.9 a.u. Our previous study [38] of N_2^+ showed that single ionization to (1,1) occurs for R=2.5-3.0 a.u., while dissociation begins near R=2.0 a.u. This is the value of R where most of the likely dissociation PECs cross with the electronic ground state. Thus,

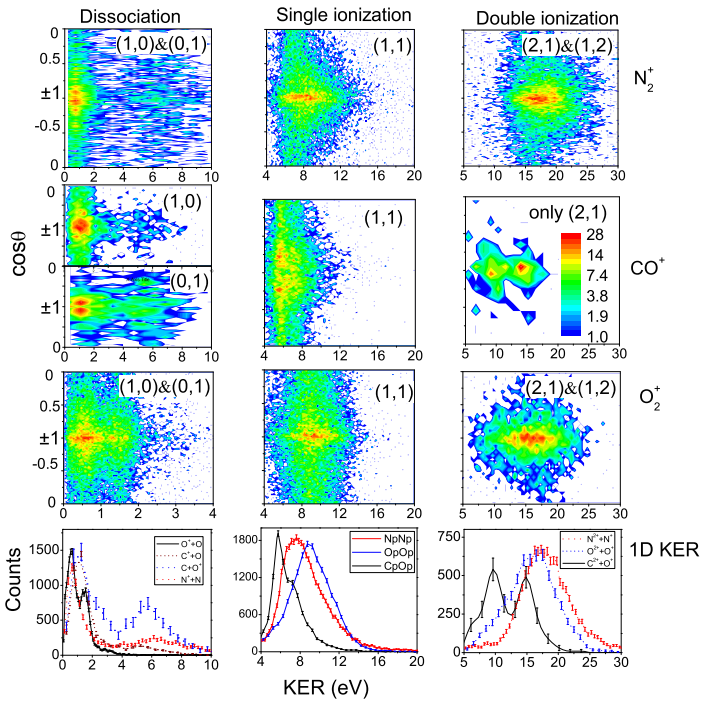

Figure 5.5: *Same as Fig. 5.3 for N_2^+, CO^+ and O_2^+ but for 7fs, 7×10^{15} W/cm^2 pulses. Note that (2,1) was the highest fragmentation channel observed for 7fs. The error bars denote the statistical uncertainty in the data. The color scale is the same for all the density plots.*

overall we can build up a picture of the time evolution of the fragmentation process.

Briefly, we return to discuss the angular distributions of the (2,2) channels, shown in Fig. 5.4 as polar plots. The dominant (2,2) contribution is strongly peaked along the laser polarization ($\sim\cos^{18}\theta$—$\cos^{24}\theta$). Intriguingly, for N_2^+ and CO^+ we observe weak side lobes showing perpendicular contributions that are absent for O_2^+ and NO^+. This suggests that some specific molecular orbital transitions (e.g. $\pi\rightarrow\sigma$) are involved, a similar phenomenon to that observed for the (3,1) and (3,2) channels starting from N_2 [79]. The presence of similar side lobes for N_2^+ and CO^+ is understandable as these molecules are electron similar, while they differ from O_2^+ and NO^+.

Ultrashort pulse: 7 fs

In order to test some of the conclusions we draw from short pulse (40 fs) results we repeat the measurements for ultrashort pulses (7 fs). The trend of the molecular fragmentation is similar in both cases. We have shown the KER and angular distributions from our 7 fs measurements as KER-cosθ density plots and 1D KER plots in Fig. 5.5.

One interesting point is that we have observed fewer breakup channels for 7 fs compared to the 40 fs pulses at the similar intensity, *i.e.* the double ionization (2,1) channel is the highest fragmentation channel for ultrashort measurements. In CO^+, we do not observe the (1,2) for this case). In ultrashort pulses, molecules have less time to stretch in between ionization steps and the ionization has to happen at smaller R where the energy gap between ionization steps is large. So, it is difficult to ionize by multiphoton absorption. In addition, as the ionization is occurring at smaller R, the wavepacket is projected to the higher lying part of the final electronic potential such that the breakup is expected to release higher KER fragments than for the short pulse.

Another point to note is that O_2^+ dissociation, *i.e.* the (1,0) channel, shows significant differences for the two cases. This is consistent with the conviction that the features of dissociation are mostly determined by the electronic potentials that are specific to each molecular ion. For 40 fs there is ample time for the O_2^+ molecule to stretch between crossings of different dissociation PECs, while for 7 fs the stretching is limited to the initially excited dissociation state. Therefore the differences in the two cases are observed as anticipated.

The angular distribution of the N_2^+ and O_2^+ double ionization (2,1) channel for 7 fs and 40 fs are shown in Fig. 5.6 using polar plots. For both molecules, these distributions at 7 fs are broader than at 40 fs. This behavior suggests that dynamic alignment has a strong influence on the angular distribution, as in 40 fs pulses the molecules have more time to align within the laser pulse compared to the 7 fs pulses. In between N_2^+ and O_2^+, we see that for 7 fs pulses the N_2^+ angular distribution is broader than O_2^+, and for 40 fs the O_2^+ distribution is broader than N_2^+. Since N_2^+ is less massive than O_2^+, it shows a larger propensity to align.

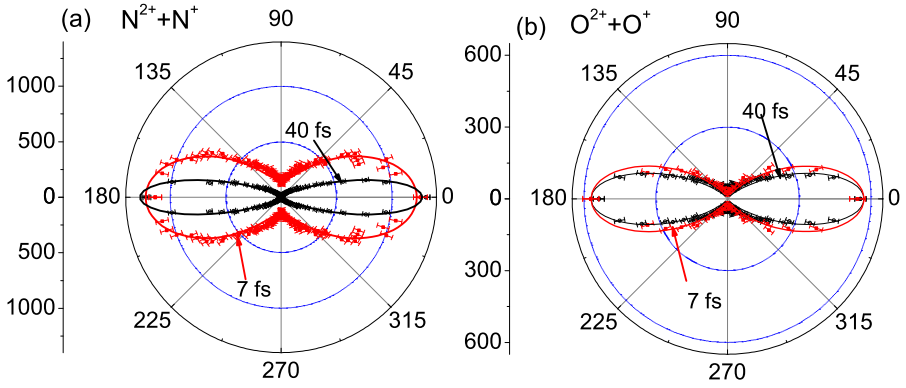

Figure 5.6: *Angular distributions for the double ionization (channel (2,1)) of (a) N_2^+ (fitted functions $a{\cdot}\cos^4\theta + b{\cdot}\sin^2\theta$ for 7 fs and $a{\cdot}\cos^{24}\theta$ for 40 fs are denoted by lines) and (b) O_2^+ (fitted functions $a{\cdot}\cos^6\theta + b{\cdot}\sin^2\theta$ for 7 fs and $a{\cdot}\cos^{10}\theta + b{\cdot}\sin^2\theta$ for 40 fs are denoted by lines) $7{\times}10^{15}$ W/cm^2 pulses. The error bars denote the statistical uncertainty in the data. The lower half of the distribution is mirrored from the upper half. Figure taken from Ref.[84].*

5.1.4 Dissociative ionization summary

We have presented the results for the multiple ionization and fragmentation of the diatomic molecular ion beams N_2^+, CO^+, NO^+, and O_2^+, in intense laser pulses (7 to 40 fs) by applying a LFI method. Using this method we detect and distinguish the neutral from the ion fragments and hence clearly separate all breakup channels. In general, we find that in dissociation the KER and angular distributions are unique to a specific molecular ion and for higher ionization channels the spectra of all molecular ions under study start to resemble one another. That is, the molecular ions seemingly lose their identity. We explain our observations on multiple ionization using a stairstep ionization mechanism that seems to be valid for both 40 fs and 7 fs pulses. Molecules stretch more in between ionization steps for 40 fs while for 7 fs they are not afforded this opportunity. So, we expect this stretching in between ionization steps to be close to $R{=}R_c$ for long pulses ($\gtrsim$100 fs) and become more direct occurring near $R{=}R_e$ in the limit of very short pulses ($\sim$3 fs or driven by electron rescattering).

5.2 Non-dissociative ionization

5.2.1 Introduction

In intense field ionization of multielectron systems, some fraction of the ionized molecules may remain as metastable dications, referred to as non-dissociative ionization. In order to be able to detect these dications their lifetimes should be long enough such that they reach the detector before dissociating and are separated from the primary beam. To the best of our knowledge, the study of laser induced non-dissociative ionization of molecular-ion targets has not been reported previously in the literature. We explore the non-dissociative ionization of CO^+ molecular ions in intense short and ultrashort laser pulses and compare it with the related dissociative ionization process. A few of the relevant PECs of CO^+ and CO^{2+} are shown in Fig. 5.7. One can see that some of the CO^{2+} states that connect to the C^++O^+ dissociation limit have a bound potential well at R smaller than about 3 a.u.. Possible ionization mechanisms for producing long lived CO^{2+} or C^++O^+ from CO^+ beam, in interactions with an intense laser field, are discussed next.

As stated above the CO^{2+} ions can be detected if their lifetime is longer than their TOF, *i.e.* a couple of microseconds (about 4 μs for the example shown in Fig. 2.14(a) in Section 2.3.5). For these ions to live long enough the CO^+ ionization should occur at the internuclear distance $R{\sim}R_e$ such that there is a good overlap between the CO^+ and CO^{2+} bound electronic states (Fig. 5.7). In other words, the ionization should be direct because there are no bound electronic states of CO^{2+} at larger internuclear distances above $R \sim 3.5$ a.u., as shown in Fig. 5.7. Both singlet and triplet electronic states of CO^{2+} are populated as a result of ionization, but only the lowest vibrational levels have long enough lifetimes to survive as dications all the way to the detector. Specifically, the states that can survive according to the lifetimes reported in literature [143, 144] are the v=0 level of the $X\,^3\Pi$, $a\,^1\Sigma^+$, and $b\,^1\Pi$ states and maybe also the v=1 level of the ground state $X\,^3\Pi$. Any population in the higher vibrational levels of these electronic states will dissociate to C^++O^+ by spin-orbit coupling to states of similar multiplicity. For example, the higher

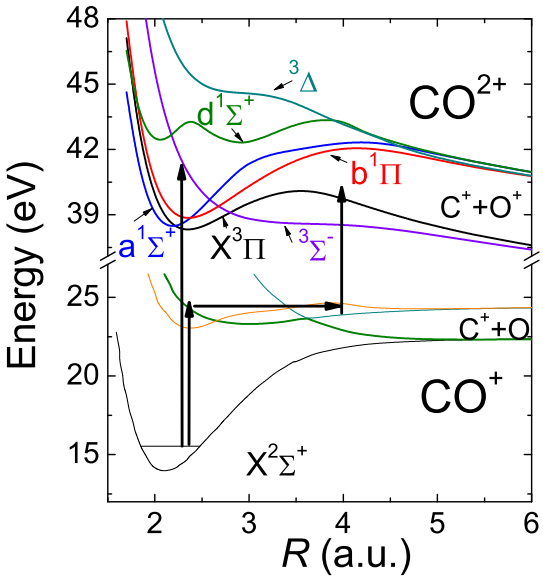

Figure 5.7: *Schematic view of possible mechanisms of dissociative and non-dissociative ionization of CO^+. Non-dissociative ionization has to be direct to populate the lowest vibrational levels, which are the only dication states that have long enough lifetimes to reach the detector (see text). Dissociative ionization in contrast can be either "direct" or "indirect". The PECs are adopted from Ref. [142] for CO^+ and Ref. [143] for CO^{2+}.*

vibrational levels of the ground state $X\,^3\Pi$ can predissociate through the $^3\Sigma^-$ state.

Dissociative ionization can occur by a few mechanisms. First, the molecule can ionize directly from CO^+ into repulsive electronic states of CO^{2+} such that it falls apart rapidly into C^+ and O^+ fragments. The signature of this mechanism is the higher KER. Second, the higher vibrational levels of the metastable electronic states of CO^{2+}, with lifetimes shorter than the TOF, will also dissociate into C^++O^+ as discussed above, and the signature is very narrow peaks in KER, e.g Ref. [70]. Third, the laser field can induce CO^+ dissociation to either C^++O or C+O^+ through the excited states of CO^+, and then the stretched CO^+ molecule can ionize at large R, *i.e.* at $R > R_e$, referred to as "indirect" ionization (sometimes referred to as enhanced ionization). This will result in a lower KER than that caused by the direct ionization mechanism discussed above. As discussed in the previous section on dissociative ionization, (*i.e.* Section 5.1) we have seen KER features produced by all these mechanisms.

5.2.2 Experimental Method

We have used the LATFI method, described in Section 2.2.4, in order to study non-dissociative ionization, as the LFI experimental method (discussed in Section 2.2.2) is not suitable because the dications are not separated from the primary ion beam. We basically identify non-dissociative ionization by using the TOF of dications and the position of their hits on the detector. The dications are separated from the primary ion beam by the static transverse field of a deflector as described in Section 2.3.5.

The number of non-dissociative ionization events is determined from the position spectrum obtained by selecting dications within the TOF peak, e.g. CO^{2+} in this case. The number of dissociative ionization events, on the other hand, is evaluated from the ion pairs within their coincidence TOF gate after imposing momentum conservation. This has been done by integrating the 1D KER spectrum (or can equivalently be done using the KER-cosθ density plots) shown in Fig. 5.3. We present these numbers as a yield of the ionization process, *i.e.* Y(CO^{2+}) is the yield for non-dissociative and Y(C^++O^+) is the yield for dissociative ionization.

In order to have a proper comparison between the yields of the two ionization processes, one has to consider the detection efficiency. For dissociative ionization it is required to detect both the fragments in coincidence. However, for non-dissociative ionization only a single hit needs to be detected, *i.e.* the CO^{2+}. We can write the measured coincidence and single particle yields as a function of efficiency and the total number of events that occurred in the laser pulses (details are given in Appendix E). The ratio of non-dissociative to dissociative ionization of CO^+, $\frac{Y(CO^{2+})}{Y(C^+ + O^+)}$, becomes $\frac{Y(CO^{2+})/\varepsilon_{CO^{2+}}}{Y(C^+ + O^+)/\varepsilon_{C^+}\varepsilon_{O^+}}$ after including the detection efficiency, where $\varepsilon_{CO^{2+}}$, ε_{C^+}, and ε_{O^+} are the efficiencies of detecting CO^{2+}, C^+ and O^+, respectively. The detection efficiency of these ions can be evaluated directly from our measurements by implementing the method discussed in detail in Appendix E (also in Ref. [145]), and hence there is no need for separate measurements.

5.2.3 Results and discussion

We have measured the dissociative and non-dissociative ionization for CO^+ molecules using short (30 fs) and ultrashort (10 fs) pulses at around 790 nm for a number of different intensities from about 10^{14} to just above 10^{16} W/cm^2. We begin with the short pulse measurements, as we did for the dissociative ionization studies presented in the previous section.

Short pulse: 30 fs

The yields for non-dissociative ionization, *i.e.* Y(CO^{2+}), and dissociative ionization, *i.e.* Y(C^++O^+), of CO^+ as a function of the laser intensity for 30 fs, 790 nm pulses are shown in Fig. 5.8(a). Both these yields increase with increasing laser intensity. For intensities above about 10^{15} W/cm^2 these yields saturate. The yield of the non-dissociative ionization is lower in comparison to the dissociative ionization at the same laser intensity, *i.e.* more fragment ions are generated than the long lived metastable dications. This is not surprising as only a few vibrational states are long lived while the majority of vibrational states break rapidly to C^++O^+.

As mentioned earlier, non-dissociative ionization has to be direct such that the long-lived lower vibrational states of metastable CO^{2+} ions are populated. On the other hand, dissociative ionization can occur by a few mechanisms leading to a broad range of KER, e.g Fig. 5.3(ii). A closer look at Fig. 5.8(a) reveals that the dissociative ionization occurs at somewhat lower intensities than non-dissociative ionization for these short pulses. This can be an indication that the CO^+ molecule first stretches to large R and then ionizes, *i.e.* indirect ionization is the dominant mechanism. This is made possible by the decrease in ionization potential for larger R. Non-dissociative ionization, in contrast, can not occur at such large R, as the electronic states of CO^{2+} are not bound there.

The ratio of non-dissociative to dissociative ionization, $\frac{Y(CO^{2+})}{Y(C^+ + O^+)}$, of CO^+ is shown in Fig. 5.8(b) (triangles). Also the ratio accounting for the detection efficiencies, $\frac{Y(CO^{2+})/\varepsilon_{CO^{2+}}}{Y(C^+ + O^+)/\varepsilon_{C^+}\varepsilon_{O^+}}$, is shown (inverted triangles) and is smaller. This ratio is smaller and has larger error bars

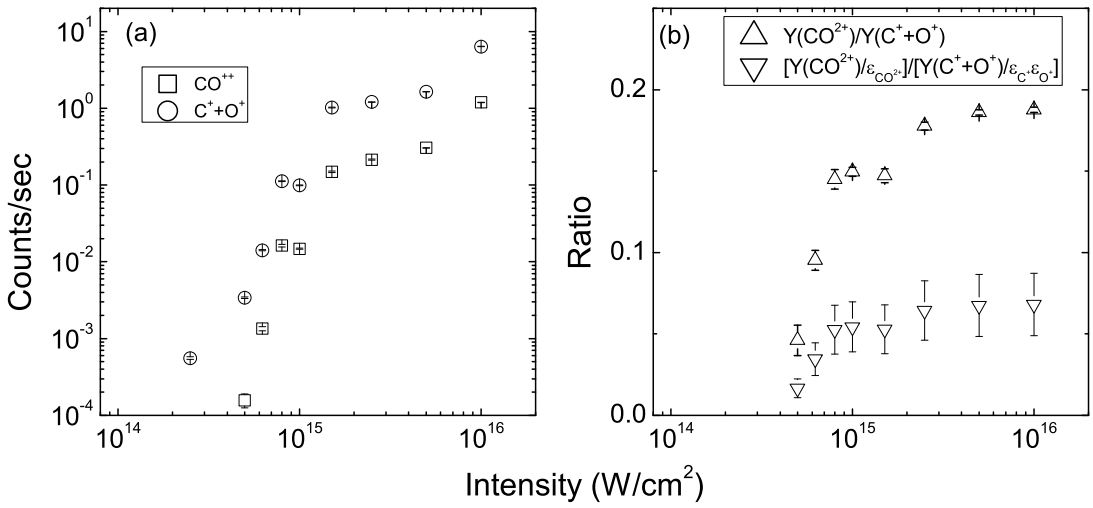

Figure 5.8: *(a) The yield of non-dissociative and dissociative ionization of CO^+ as a function of laser intensity for 30 fs laser pulses. Both ionization channels display similar behavior with the laser intensity even though the yield of the non-dissociative ionization is smaller compared to the dissociative ionization. (b) Ratio (triangles) of non-dissociative to dissociative ionization from panel (a). The ratio corrected for detection efficiency (inverted triangles) is also shown. It differs from uncorrected ratio by only a scaling factor and hence there is no change in the behavior with intensity. The error bars denote the statistical uncertainty in the data for the yield and the ratio. For the efficiency corrected ratio it also includes the errors from the uncertainty in the measured efficiencies.*

due to the additional uncertainty in the measured detection efficiencies. As mentioned before, these efficiencies are evaluated directly from the same data set (see Appendix E and Ref. [145]). The efficiency correction gives a scaling of the ratio and does not change the shape of the distribution. Both of these ratios first increase with intensity and then saturate. The ratio also indicates that the non-dissociative ionization is a little less than 10% of the dissociative ionization at the saturation level for these short pulse measurements. The reason for this saturation and the saturation level needs further exploration.

To test the importance of the indirect ionization mechanism proposed above for dissociative ionization, we repeated the measurements using ultrashort pulses ($\leq$10fs). In such ultrashort pulses there is not enough time for the molecule to stretch before ionization, and as a result dissociative ionization should reduce significantly if our suggested interpretation

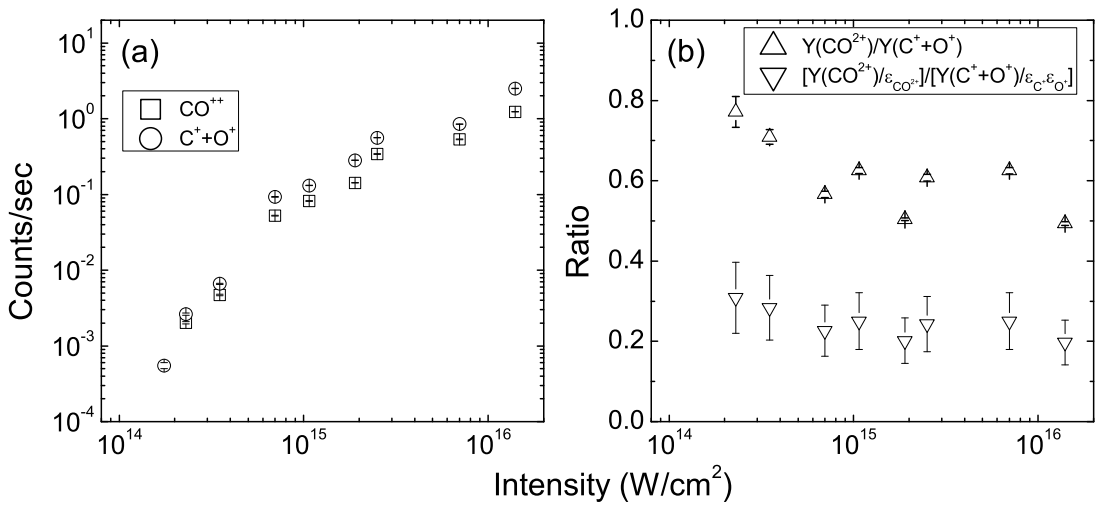

Figure 5.9: *Similar to Fig. 5.8, but for ultrashort (10 fs) pulses.*

is valid. We report on these measurements next.

Ultrashort pulse: 10 fs

We display the results of CO^+ ionization measurements with ultrashort laser pulses for different laser intensities in Fig. 5.9(a). The interesting features of the ionization of the CO^+ molecules in this ultrashort pulse are:

(i) The non-dissociative ionization yield is observed to be smaller than the dissociative ionization yield as for the short pulse measurements.

(ii) Non-dissociative ionization extends to slightly lower intensities than for the short pulses.

(iii) The yield of non-dissociative ionization by an ultrashort pulse for the highest intensity measured is almost the same as that of the short pulse measurements (*i.e.* just above 1). That is, the non-dissociative ionization rate is the same even though the pulse duration is shorter by a factor of three.

(iv) The non-dissociative to dissociative ionization ratio, as shown in Fig. 5.9(b), is much higher (almost by a factor of three) than for short pulses.

For the measurements using ultrashort pulses we have seen differences compared to those of short pulses, mainly the reduction in dissociative ionization yield.

The ratio of non-dissociative to dissociative ionization for both 10 and 35 fs pulses are compared in Fig. 5.10. This ratio is significantly higher (almost by a factor of three for the saturation regime) for ultrashort pulses. The intensity dependence of this ratio is also different. In short pulse measurements the ratio first increases with increasing intensity and then saturates. But for the ultrashort pulse measurements the ratio slightly decreases with increasing laser intensity toward saturation and it is not clear if saturation is reached. The reason for this different behavior is not obvious and requires further study. Based on the ratio near the saturation level we can say that the contribution from indirect ionization at large R is reduced significantly, for ultrashort pulses, as predicted above. This is because the molecule does not have enough time to stretch before ionization, therefore the reduction of dissociative ionization leads to an increase in the non-dissociative to dissociative ionization ratio.

Based on the observed results we believe that both ionization mechanisms (direct and indirect) are responsible for dissociative ionization in short pulse (30fs) measurements, while for the ultrashort pulse measurements we managed to suppress the dissociative ionization at large R.

5.2.4 Non-dissociative ionization summary

We have demonstrated the ability to simultaneously measure non-dissociative and dissociative ionization of molecular-ion beams using the LATFI method. We have done that specifically using CO^+ as an example, however, the method can be easily extended to other species. We find that the ratio of the non-dissociative to dissociative ionization increases significantly when reducing the pulse duration, *i.e.* for ultrashort pulses (10 fs) compared to the short pulses (30 fs), mainly by suppressing the dissociative ionization for ultrashort pulses. This supports the interpretation that dissociative ionization has two possible mech-

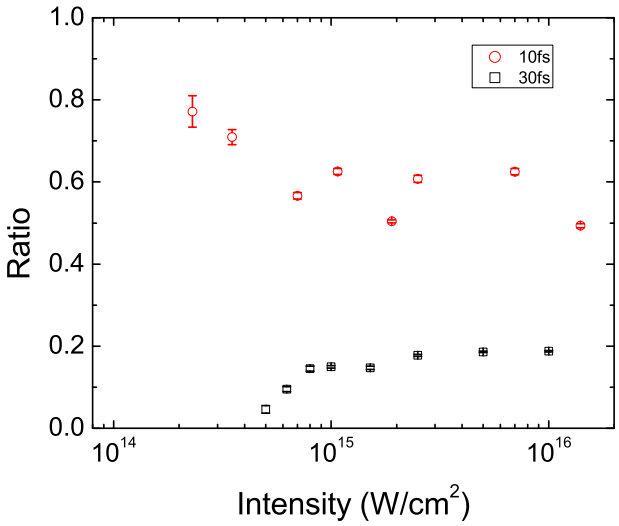

Figure 5.10: *Ratio of the non-dissociative to dissociative ionization of CO^+ using short (30 fs) — open squares and ultrashort (10 fs) pulses — open circles at about 790 nm. The ratio is larger by almost a factor of three for ultrashort pulses. Since the ratio corrected for detection efficiencies has the similar trend with intensity (except the larger error bars), we show the ratio without correction. The error bars denote the statistical uncertainty in the data.*

anisms – direct ionization followed by dissociation or indirect ionization – and demonstrates control over the latter mechanism. In general, this is consistent with the stairstep ionization mechanism discussed in Section 5.1.

5.3 Conclusions

We have presented the ionization studies of multielectron systems in this chapter. To summarize, we have studied dissociative ionization in detail choosing the family of molecules N_2^+, CO^+, NO^+, and O_2^+ while demonstrating measurements on non-dissociative ionization using CO^+ as an example. From the observed results we conclude that the dissociative ionization of the molecules used in this study follows a stairstep mechanism while the non-dissociative ionization is governed by the direct ionization mechanism. In both cases, the laser pulse duration acts as a control knob for manipulating the dissociative ionization yield by reducing the indirect path.

Chapter 6

Summary and future directions

6.1 Summary

Using a coincidence three-dimensional momentum imaging method we have explored the molecular fragmentation dynamics for a variety of molecules, *i.e.* from benchmark diatomic and polyatomic molecules — H_2^+ and H_3^+ — to multielectron diatomic molecules like N_2^+, CO^+, NO^+, and O_2^+.

Upgraded versions of our experimental method have been developed in order to explore regions that are not possible with the longitudinal field imaging (LFI) method, e.g. measurements of very low kinetic energy fragments and non-dissociative ionization of multielectron systems. The transverse field imaging (TFI) method allows the separation of fragments solely by their position on the detector and has a field-free interaction region, which is a necessary step towards building a setup for electron detection. On the other hand, the longitudinal and transverse field imaging (LATFI) method we developed allows the measurement of very low energy fragments in coincidence, including mass asymmetric molecules of mass ratio up to about 7 for an individual dissociation channel (but not both channels simultaneously), and non-dissociative ionization.

Very slow dissociation of H_2^+ induced by an intense laser is explored. We have presented clear experimental evidence of very low kinetic energy release (down to almost 0 eV) as a signature of the zero-photon dissociation (ZPD) phenomenon. The interpretation of our data

is supported by the theoretical results obtained by solving the time-dependent Schrödinger equation for H_2^+ in the Born-Oppenheimer representation including nuclear rotation, nuclear vibration and electronic excitation. This ZPD mechanism is explained as a two-photon process, *i.e.* absorption of one photon and stimulated emission of a slightly lower energy photon within the bandwidth of the laser pulse. That is why the ultrashort transform limited pulses are better for ZPD observation as they have a larger bandwidth. We have explored the intensity dependence of ZPD to identify the best condition for observing this phenomenon and found it to be at intermediate intensities ($\sim 10^{13}\,\mathrm{W/cm^2}$). At lower intensities the nonlinear two-photon process does not occur and at higher intensities the ZPD feature is convoluted with the low KER contribution from the bond softening mechanism. We have also searched for the wavelength dependence using a shorter wavelength (395 nm) produced by second harmonic generation from the fundamental light (790 nm), and found that the ZPD yield was reduced significantly to almost nothing. In a way, we need to explore the longer wavelength regime as there is a higher probability for a transition from the electronic ground state to the continuum of the first excited state in that case.

We have demonstrated the capability of the LATFI method for the measurement of polyatomic systems by using the benchmark H_3^+ targets. This polyatomic molecule preferentially dissociates in strong laser fields into two-body final products, *i.e.* $H^+ + H_2$ and $H_2^+ + H$. The $H^+ + H_2$ channel is found to have a very low breakup energy. We have outlined the dissociation pathways and verified their validity using laser pulses of different wavelengths and pulse durations.

In the dissociative ionization studies we find that the multielectron dissociative ionization (MEDI) of a family of molecules (specifically, N_2^+, CO^+, NO^+, and O_2^+) follows a very general mechanism, *i.e.* a stairstep ionization mechanism. The non-dissociative ionization study of CO^+ is presented mainly to demonstrate this additional capability of the LATFI method. The results show that dissociative ionization can be manipulated with laser pulse duration.

In order to conclude, a few experiments that are possible with these upgraded methods

are discussed next.

6.2 Future directions

Some interesting experiments are possible with further upgrades of the TFI and LATFI methods. One example would be the detection of electrons in coincidence with the ionic fragments by taking advantage of the field free interaction region of the TFI method. To accomplish this one additional detector has to be added to detect these electrons. This will make the ionization studies kinematically complete like our dissociation measurements. Another direction would be to add a second ion detector, off axis, for the detection of the lighter ionic fragments from the break up of mass asymmetric molecules like OH^+ or HDO^+. In OH^+ the energy difference between the two lowest dissociation limits is small (about 20 meV) and hence it would be interesting to explore any differences between the two dissociation channels. In the case of HDO^+, it is interesting to control which bond (OH or OD) we can break using the laser pulses.

The yield of low energy breakup in H_2^+ is very low. Such measurements will be easier in the near future with the addition of a new high repetition rate laser system in JRML. One can explore the ZPD of H_2^+ in the longer wavelength regime using an optical parametric amplifier.

The slow dissociation studies of H_3^+ can be extended to the next level by using isotopes like HD_2^+ or H_2D^+, where some isotopic effects are observed in ionization at high KER.

The slow dissociation studies can be performed in multielectron systems. As we have already observed in the case of O_2^+, one can explore the dissociation of diatomic species, e.g. ND^+, N_2^+, CO^+, NO^+ and others, for possible low energy breakup.

The non-dissociative ionization studies of CO^+ presented in this work can be extended to other multielectron systems. This project has already been adopted by a fellow graduate student in our group as a beginning project. It is also possible to extend these studies to atomic-ion targets, like Ar^+.

From all these projects there is already a good start for future experiments, and the new laser in the lab will definitely help in exploring these and other interesting projects.

Bibliography

[1] A. T. Le and C. D. Lin, Nature Photonics **4**, 671 (2010).

[2] M. F. Kling, C. Siedschlag, A. J. Verhoef, J. I. Khan, M. Schultze, T. Uphues, Y. Ni, M. Uiberacker, M. Drescher, F. Krausz, et al., Science **312**, 246 (2006).

[3] P. B. Corkum and F. Krausz, Nature Phys. **3**, 381 (2007).

[4] F. Krausz and M. Ivanov, Rev. Mod. Phys. **81**, 163 (2009).

[5] E. Gagnon, P. Ranitovic, X.-M. Tong, C. L. Cocke, M. M. Murnane, H. C. Kapteyn, and A. S. Sandhu, Science **317**, 1374 (2007).

[6] L. J. Frasinski, J. H. Posthumus, J. Plumridge, K. Codling, P. F. Taday, and A. J. Langley, Phys. Rev. Lett. **83**, 3625 (1999).

[7] J. H. Posthumus, J. Plumridge, L. J. Frasinski, K. Codling, E. J. Divall, A. J. Langley, and P. F. Taday, J. Phys. B: At. Mol. Opt. Phys. **33**, L563 (2000).

[8] L. J. Frasinski, J. Plumridge, J. H. Posthumus, K. Codling, P. F. Taday, E. J. Divall, and A. J. Langley, Phys. Rev. Lett. **86**, 2541 (2001).

[9] K. Codling and L. J. Frasinski, J. Phys. B: At. Mol. Opt. Phys. **26**, 783 (1993).

[10] A. Giusti-Suzor, F. H. Mies, L. F. DiMauro, E. Charron, and B. Yang, J. Phys. B: At. Mol. Opt. Phys. **28**, 309 (1995).

[11] J. H. Posthumus, Rep. Prog. Phys. **67**, 623 (2004).

[12] I. Ben-Itzhak, in *Progress in Ultrafast Intense Laser Science IV*, edited by K. Yamanouchi, A. Becker, R. Li, and S. L. Chin (Springer, New York, 2009), vol. **91** of *Springer Series in Chemical Physics*, p. 67.

[13] P. H. Bucksbaum, A. Zavriyev, H. G. Muller, and D. W. Schumacher, Phys. Rev. Lett. **64**, 1883 (1990).

[14] A. Zavriyev, P. H. Bucksbaum, H. G. Muller, and D. W. Schumacher, Phys. Rev. A: Atomic, Molecular, and Optical Physics **42**, 5500 (1990).

[15] A. Giusti-Suzor and F. H. Mies, Phys. Rev. Lett. **68**, 3869 (1992).

[16] A. Giusti-Suzor, X. He, O. Atabek, and F. H. Mies, Phys. Rev. Lett. **64**, 515 (1990).

[17] A. Zavriyev, P. H. Bucksbaum, J. Squier, and F. Saline, Phys. Rev. Lett. **70**, 1077 (1993).

[18] S. Chelkowski, A. Conjusteau, T. Zuo, and A. D. Bandrauk, Phys. Rev. A: Atomic, Molecular, and Optical Physics **54**, 3235 (1996).

[19] K. Codling, L. J. Frasinski, and P. A. Hatherly, J. Phys. B: At. Mol. Opt. Phys. **21**, L433 (1998).

[20] H. Stapelfeldt, E. Constant, and P. B. Corkum, Phys. Rev. Lett. **74**, 3780 (1995).

[21] A. D. Bandrauk and M. L. Sink, J. Chem. Phys. **74**, 1110 (1981).

[22] J. H. Shirley, Phys. Rev. **138**, B979 (1965).

[23] S.-I. Chu, J. Chem. Phys. **75**, 2215 (1981).

[24] T. F. George, J. Phys. Chem. **86**, 10 (1982).

[25] X. He, O. Atabek, and A. Giusti-Suzor, Phys. Rev. A: Atomic, Molecular, and Optical Physics **38**, 5586 (1988).

[26] A. Keller, C. M. Dion, and O. Atabek, Phys. Rev. A: Atomic, Molecular, and Optical Physics **61**, 023409 (2000).

[27] G. N. Gibson, L. Fang, and B. Moser, Phys. Rev. A: Atomic, Molecular, and Optical Physics **74**, 041401 (2006).

[28] F. Anis and B. D. Esry, Phys. Rev. A: Atomic, Molecular, and Optical Physics **77**, 033416 (2008).

[29] F. Anis, Ph.D. thesis, Kansas State University, Manhattan, Kansas, U.S.A. (2009).

[30] J. McKenna, A. M. Sayler, F. Anis, B. Gaire, N. G. Johnson, E. Parke, J. J. Hua, H. Mashiko, C. M. Nakamura, E. Moon, et al., Phys. Rev. Lett. **100**, 133001 (2008).

[31] P. Agostini, F. Fabre, G. Mainfray, G. Petite, and N. K. Rahman, Phys. Rev. Lett. **42**, 1127 (1979).

[32] J. H. Posthumus, L. J. Frasinski, A. J. Giles, and K. Codling, J. Phys. B: At. Mol. Opt. Phys. **28**, L349 (1995).

[33] J. H. Posthumus, A. J. Giles, M. R. Thompson, and K. Codling, J. Phys. B: At. Mol. Opt. Phys. **29**, 5811 (1996).

[34] B. D. Esry, A. M. Sayler, P. Q. Wang, K. D. Carnes, and I. Ben-Itzhak, Phys. Rev. Lett. **97**, 013003 (2006).

[35] A. Staudte, D. Pavičić, S. Chelkowski, D. Zeidler, M. Meckel, H. Niikura, M. Schöffler, S. Schössler, B. Ulrich, P. P. Rajeev, et al., Phys. Rev. Lett. **98**, 073003 (2007).

[36] B. D. Esry and I. Ben-Itzhak, Phys. Rev. A: Atomic, Molecular, and Optical Physics **82**, 043409 (2010).

[37] J. McKenna, A. M. Sayler, B. Gaire, N. G. Johnson, E. Parke, K. D. Carnes, B. D. Esry, and I. Ben-Itzhak, Phys. Rev. A: Atomic, Molecular, and Optical Physics **80**, 023421 (2009).

[38] B. Gaire, J. McKenna, A. M. Sayler, N. G. Johnson, E. Parke, K. D. Carnes, B. D. Esry, and I. Ben-Itzhak, Phys. Rev. A: Atomic, Molecular, and Optical Physics **78**, 033430 (2008).

[39] L. V. Keldysh, Sov. Phys. JETP **20**, 1307 (1965).

[40] P. B. Corkum, Phys. Rev. Lett. **71**, 1994 (1993).

[41] J. L. Krause, K. J. Schafer, and K. C. Kulander, Phys. Rev. Lett. **68**, 3535 (1992).

[42] M. Nisoli, G. Sansone, S. Stagira, S. De Silvestri, C. Vozzi, M. Pascolini, L. Poletto, P. Villoresi, and G. Tondello, Phys. Rev. Lett. **91**, 213905 (2003).

[43] A. D. Bandrauk, S. Barmaki, and G. L. Kamta, Phys. Rev. Lett. **98**, 013001 (2007).

[44] X. Feng, S. Gilbertson, H. Mashiko, H. Wang, S. D. Khan, M. Chini, Y. Wu, K. Zhao, and Z. Chang, Phys. Rev. Lett. **103**, 183901 (2009).

[45] T. Nubbemeyer, K. Gorling, A. Saenz, U. Eichmann, and W. Sandner, Phys. Rev. Lett. **101**, 233001 (2008).

[46] B. Manschwetus, T. Nubbemeyer, K. Gorling, G. Steinmeyer, U. Eichmann, H. Rottke, and W. Sandner, Phys. Rev. Lett. **102**, 113002 (2009).

[47] Z. Vager, R. Naaman, and E. P. Kanter, Science **244**, 426 (1989).

[48] D. Zajfman, T. Graber, E. P. Kanter, and Z. Vager, Phys. Rev. A: Atomic, Molecular, and Optical Physics **46**, 194 (1992).

[49] A. Belkacem, E. P. Kanter, R. E. Mitchell, Z. Vager, and B. J. Zabransky, Phys. Rev. Lett. **63**, 2555 (1989).

[50] E. Baldit, S. Saugout, and C. Cornaggia, Phys. Rev. A: Atomic, Molecular, and Optical Physics **71**, 021403 (2005).

[51] H. Stapelfeldt and T. Seideman, Rev. Mod. Phys. **75**, 543 (2003).

[52] J. H. Posthumus, J. Plumridge, M. K. Thomas, K. Codling, L. J. Frasinski, A. J. Langley, and P. F. Taday, J. Phys. B: At. Mol. Opt. Phys. **31**, L553 (1998).

[53] K. Miyazaki, T. Shimizu, and D. Normand, J. Phys. B: At. Mol. Opt. Phys. **37**, 753 (2004).

[54] X. M. Tong, Z. X. Zhao, and C. D. Lin, Phys. Rev. A: Atomic, Molecular, and Optical Physics **66**, 033402 (2002).

[55] E. Wells, M. J. DeWitt, and R. R. Jones, Phys. Rev. A: Atomic, Molecular, and Optical Physics **66**, 013409 (2002).

[56] X. M. Tong, Z. X. Zhao, A. S. Alnaser, S. Voss, C. L. Cocke, and C. D. Lin, J. Phys. B: At. Mol. Opt. Phys. **38**, 333 (2005).

[57] F. Anis, T. Cackowski, and B. D. Esry, J. Phys. B: At. Mol. Opt. Phys. **42**, 091001 (2009).

[58] A. S. Alnaser, C. M. Maharjan, X. M. Tong, B. Ulrich, P. Ranitovic, B. Shan, Z. Chang, C. D. Lin, C. L. Cocke, and I. V. Litvinyuk, Phys. Rev. A: Atomic, Molecular, and Optical Physics **71**, 031403 (2005).

[59] R. Torres, R. de Nalda, and J. P. Marangos, Phys. Rev. A: Atomic, Molecular, and Optical Physics **72**, 023420 (2005).

[60] F. Légaré, I. V. Litvinyuk, P. W. Dooley, F. Quéré, A. D. Bandrauk, D. M. Villeneuve, and P. B. Corkum, Phys. Rev. Lett. **91**, 093002 (2003).

[61] A. S. Alnaser, X. M. Tong, T. Osipov, S. Voss, C. M. Maharjan, P. Ranitovic, B. Ulrich, B. Shan, Z. Chang, C. D. Lin, et al., Phys. Rev. Lett. **93**, 183202 (2004).

[62] T. Zuo and A. D. Bandrauk, Phys. Rev. A: Atomic, Molecular, and Optical Physics **52**, R2511 (1995).

[63] I. Ben-Itzhak, P. Q. Wang, J. F. Xia, A. M. Sayler, M. A. Smith, K. D. Carnes, and B. D. Esry, Phys. Rev. Lett. **95**, 073002 (2005).

[64] I. Ben-Itzhak, P. Q. Wang, J. F. Xia, A. M. Sayler, M. A. Smith, J. W. Maseberg, K. D. Carnes, and B. D. Esry, Nucl. Instrum. and Methods in Phys. Res. B **233**, 56 (2005).

[65] A. M. Sayler, Ph.D. thesis, Kansas State University, Manhattan, Kansas, U.S.A. (2008).

[66] L.-Y. Peng, D. Dundas, J. F. McCann, K. T. Taylor, and I. D. Williams, J. Phys. B: At. Mol. Opt. Phys. **36**, L295 (2003).

[67] J. B. Greenwood, I. M. G. Johnston, P. McKenna, I. D. Williams, T. R. J. Goodworth, J. H. Sanderson, W. A. Bryan, A. A. A. El-Zein, W. R. Newell, A. J. Langley, et al., Phys. Rev. Lett. **88**, 233001 (2002).

[68] D. Pavičić, T. W. Hänsch, and H. Figger, Phys. Rev. A: Atomic, Molecular, and Optical Physics **72**, 053413 (2005).

[69] D. Pavičić, A. Kiess, T. W. Hänsch, and H. Figger, Phys. Rev. Lett. **94**, 163002 (2005).

[70] M. Lundqvist, P. Baltzer, D. Edvardsson, L. Karlsson, and B. Wannberg, Phys. Rev. Lett. **75**, 1058 (1995).

[71] X. Urbain, B. Fabre, E. M. Staicu-Casagrande, N. de Ruette, V. M. Andrianarijaona, J. Jureta, J. H. Posthumus, A. Saenz, E. Baldit, and C. Cornaggia, Phys. Rev. Lett. **92**, 163004 (2004).

[72] J. McKenna, M. Suresh, B. Srigengan, I. D. Williams, W. A. Bryan, E. M. L. English, S. L. Stebbings, W. R. Newell, I. C. E. Turcu, J. M. Smith, et al., Phys. Rev. A: Atomic, Molecular, and Optical Physics **73**, 043401 (2006).

[73] J. Wu, H. Zeng, J. Wang, and C. Guo, Phys. Rev. A: Atomic, Molecular, and Optical Physics **73**, 051402 (2006).

[74] J. P. Nibarger, S. V. Menon, and G. N. Gibson, Phys. Rev. A: Atomic, Molecular, and Optical Physics **63**, 053406 (2001).

[75] A. Talebpour, S. Larochelle, and S. L. Chin, J. Phys. B: At. Mol. Opt. Phys. **30**, L245 (1997).

[76] L. J. Frasinski, K. Codling, and P. A. Hatherly, Science **246**, 1029 (1989).

[77] A. Iwamae, A. Hishikawa, and K. Yamanouchi, J. Phys. B: At. Mol. Opt. Phys. **33**, 223 (2000).

[78] S. Voss, A. S. Alnaser, X. M. Tong, C. Maharjan, P. Ranitovic, B. Ulrich, B. Shan, Z. Chang, C. D. Lin, and C. L. Cocke, J. Phys. B: At. Mol. Opt. Phys. **37**, 4239 (2004).

[79] W. Guo, J. Zhu, B. Wang, Y. Wang, and L. Wang, Phys. Rev. A: Atomic, Molecular, and Optical Physics **77**, 033415 (2008).

[80] H. Mashiko, C. M. Nakamura, C. Li, E. Moon, H. Wang, J. Tackett, and Z. Chang, Appl. Phys. Lett. **90**, 161114 (2007).

[81] P. Q. Wang, A. M. Sayler, K. D. Carnes, J. F. Xia, M. A. Smith, B. D. Esry, and I. Ben-Itzhak, Phys. Rev. A: Atomic, Molecular, and Optical Physics **74**, 043411 (2006).

[82] A. M. Sayler, P. Q. Wang, K. D. Carnes, B. D. Esry, and I. Ben-Itzhak, J. Phys. B: At. Mol. Opt. Phys. **40**, 4367 (2007).

[83] J. McKenna, A. M. Sayler, B. Gaire, N. G. Johnson, K. D. Carnes, B. D. Esry, and I. Ben-Itzhak, Phys. Rev. Lett. **103**, 103004 (2009).

[84] B. Gaire, J. McKenna, N. G. Johnson, A. M. Sayler, E. Parke, K. D. Carnes, and I. Ben-Itzhak, Phys. Rev. A: Atomic, Molecular, and Optical Physics **79**, 063414 (2009).

[85] A. M. Sayler, P. Q. Wang, K. D. Carnes, B. D. Esry, and I. Ben-Itzhak, Phys. Rev. A: Atomic, Molecular, and Optical Physics **75**, 063420 (2007).

[86] J. McKenna, A. M. Sayler, B. Gaire, N. G. Johnson, E. Parke, K. D. Carnes, B. D. Esry, and I. Ben-Itzhak, Phys. Rev. A **77**, 063422 (2008).

[87] J. McKenna, A. M. Sayler, F. Anis, N. G. Johnson, B. Gaire, U. Lev, M. A. Zohrabi, K. D. Carnes, B. D. Esry, and I. Ben-Itzhak, Phys. Rev. A: Atomic, Molecular, and Optical Physics **81**, 061401 (2010).

[88] B. Gaire, J. McKenna, A. M. Sayler, F. Anis, M. Zohrabi, N. G. Johnson, J. J. Hua, K. D. Carnes, B. D. Esry, and I. Ben-Itzhak, in preparation (2011).

[89] M. Zohrabi, J. McKenna, B. Gaire, N. G. Johnson, K. D. Carnes, S. De, I. A. Bocharova, M. Magrakvelidze, D. Ray, I. V. Litvinyuk, et al., Phys. Rev. A: Atomic, Molecular, and Optical Physics **83**, 053405 (2011).

[90] D. J. Kane and R. Trebino, IEEE J. Quant. Electron. **29**, 571 (1993).

[91] J. H. Posthumus, B. Fabre, C. Cornaggia, N. de Ruette, and X. Urbain, Phys. Rev. Lett. **101**, 233004 (2008).

[92] J. D. Alexander, C. R. Calvert, R. B. King, O. Kelly, L. Graham, W. A. Bryan, G. R. A. J. Nemeth, W. R. Newell, C. A. Froud, I. C. E. Turcu, et al., J. Phys. B: At. Mol. Opt. Phys. **42**, 141004 (2009).

[93] S. W. Allendorf and A. Szöke, Phys. Rev. A: Atomic, Molecular, and Optical Physics **44**, 518 (1991).

[94] T. E. Sharp, Atomic Data **2**, 119 (1971).

[95] D. A. Long, *The Raman Effect: A Unified Treatment of the Theory of Raman Scattering by Molecules* (John Wiley and Sons, Ltd, London, 2002).

[96] J. McKenna, F. Anis, B. Gaire, N. G. Johnson, M. Zohrabi, K. D. Carnes, B. D. Esry, and I. Ben-Itzhak, Phys. Rev. Lett. **103**, 103006 (2009).

[97] L. J. Frasinski, C. R. Courtney, and C. Codling, Laser Phys. **12**, 463 (2002).

[98] J. J. Hua and B. D. Esry, J. Phys. B: At. Mol. Opt. Phys. **42**, 085601 (2009).

[99] J. J. Hua and B. D. Esry, Phys. Rev. A: Atomic, Molecular, and Optical Physics **80**, 013413 (2009).

[100] V. Roudnev and B. D. Esry, Phys. Rev. Lett. **99**, 220406 (2007).

[101] B. D. Esry and H. R. Sadeghpour, Phys. Rev. A: Atomic, Molecular, and Optical Physics **60**, 3604 (1999).

[102] J. McKenna, M. Suresh, D. S. Murphy, W. Bryan, L.-Y. Peng, S. Stebbings, E. M. L. English, J. Wood, B. Srigengan, I. E. Turcu, et al., J. Phys. B: At. Mol. Opt. Phys. **40**, 2607 (2007).

[103] S. Datz, G. Sundström, C. Biedermann, L. Broström, H. Danared, S. Mannervik, J. R. Mowat, and M. Larsson, Phys. Rev. Lett. **74**, 896 (1995).

[104] J. E. Mann, C. M. Laperle, J. D. Savee, and R. E. Continetti, Chem. Phys. Lett. **473**, 34 (2009).

[105] U. Galster, P. Kaminski, M. Beckert, H. Helm, and U. Muller, Euro. Phys. J. D: Atomic, Molecular, Optical and Plasma Physics **17**, 307 (2001).

[106] A. Carrington and R. A. Kennedy, J. Chem. Phys. **81**, 91 (1984).

[107] D. Zajfman, O. Heber, L. Vejby-Christensen, I. Ben-Itzhak, M. Rappaport, R. Fishman, and M. Dahan, Phys. Rev. A: Atomic, Molecular, and Optical Physics **55**, R1577 (1997).

[108] V. G. Anicich and J. H. Futrell, International Journal of Mass Spectrometry and Ion Processes **55**, 189 (1984).

[109] D. Talbi and R. P. Saxon, J. Chem. Phys. **89**, 2235 (1988).

[110] C. Beylerian and C. Cornaggia, J. Phys. B: At. Mol. Opt. Phys. **37**, L259 (2004).

[111] R. N. Coffee, L. Fang, and G. N. Gibson, Phys. Rev. A: Atomic, Molecular, and Optical Physics **73**, 043417 (2006).

[112] S. Banerjee, G. Ravindra Kumar, and D. Mathur, Phys. Rev. A: Atomic, Molecular, and Optical Physics **60**, R25 (1999).

[113] P. Hansch and L. D. V. Woerkom, Opt. Lett. **21**, 1286 (1996).

[114] R. J. Gdanitz, Chem. Phys. Lett. **283**, 253 (1998).

[115] A. Ehresmann, L. Werner, S. Klumpp, S. Lucht, H. Schmoranzer, S. Mickat, R. Schill, K.-H. Schartner, P. V. Demekhin, M. P. Lemeshko, et al., J. Phys. B: At. Mol. Opt. Phys. **39**, 283 (2006).

[116] T. Aoto, K. Ito, Y. Hikosaka, A. Shibasaki, R. Hirayama, N. Yamamono, and E. Miyoshi, J. Chem. Phys. **124**, 234306 (2006).

[117] M. Lundqvist, D. Edvardsson, P. Baltzer, and B. Wannberg, J. Phys. B: At. Mol. Opt. Phys. **29**, 1489 (1996).

[118] M. Hochlaf, G. Chambaud, and P. Rosmus, J. Phys. B: At. Mol. Opt. Phys. **30**, 4509 (1997).

[119] N. Abramzon, R. B. Siegel, and K. Becker, J. Phys. B: At. Mol. Opt. Phys. **32**, L247 (1999).

[120] D. H. Crandall, W. E. Kauppila, R. A. Phaneuf, P. O. Taylor, and G. H. Dunn, Phys. Rev. A: Atomic, Molecular, and Optical Physics **9**, 2545 (1974).

[121] P. C. Cosby, J. Chem. Phys. **98**, 9544 (1993).

[122] F. R. Gilmore, R. R. Laher, and P. J. Espy, J. Phys. Chem. Ref. Data **21**, 1005 (1992).

[123] A. Hishikawa, S. Liu, A. Iwasaki, and K. Yamanouchi, J. Chem. Phys. **114**, 9856 (2001).

[124] R. E. Stratmann, G. Bandarage, and R. R. Lucchese, Phys. Rev. A: Atomic, Molecular, and Optical Physics **51**, 3756 (1995).

[125] J. A. Nichols, D. L. Yeager, and P. Jørgensen, J. Chem. Phys. **80**, 293 (1984).

[126] E. Y. Sidky and I. Ben-Itzhak, Phys. Rev. A: Atomic, Molecular, and Optical Physics **60**, 3586 (1999).

[127] H. D. Hagstrum and J. T. Tate, Phys. Rev. **59**, 354 (1941).

[128] C. J. Latimer, Adv. At. Mol. Opt. Phys **30**, 105 (1992).

[129] J. Rudati, J. L. Chaloupka, P. Agostini, K. C. Kulander, and L. F. DiMauro, Phys. Rev. Lett. **92**, 203001 (2004).

[130] T. Seideman, M. Y. Ivanov, and P. B. Corkum, Phys. Rev. Lett. **75**, 2819 (1995).

[131] C. Cornaggia, J. Lavancier, D. Normand, J. Morellec, P. Agostini, J. P. Chambaret, and A. Antonetti, Phys. Rev. A: Atomic, Molecular, and Optical Physics **44**, 4499 (1991).

[132] C. Cornaggia and L. Quaglia, Phys. Rev. A: Atomic, Molecular, and Optical Physics **63**, 030702 (2001).

[133] P. Hering and C. Cornaggia, Phys. Rev. A: Atomic, Molecular, and Optical Physics **57**, 4572 (1998).

[134] J. Wu, H. Zeng, and C. Guo, J. Phys. B: At. Mol. Opt. Phys. **40**, 1095 (2007).

[135] H. Ren, R. Ma, J. Chen, X. Li, H. Yang, and Q. Gong, J. Phys. B: At. Mol. Opt. Phys. **36**, 2179 (2007).

[136] C. Guo, Phys. Rev. A: Atomic, Molecular, and Optical Physics **71**, 021405 (2005).

[137] A. Talebpour, S. Larochelle, and S. L. Chin, J. Phys. B: At. Mol. Opt. Phys. **30**, 1927 (1997).

[138] J. Wu, H. Zeng, and C. Guo, Phys. Rev. A: Atomic, Molecular, and Optical Physics **74**, 031404 (2006).

[139] G. Handke, F. Tarantelli, and L. S. Cederbaum, Phys. Rev. Lett. **76**, 896 (1996).

[140] H. Niikura, F. Légaré, R. Hasbani, A. D. Bandrauk, M. Y. Ivanov, D. M. Villeneuve, and P. B. Corkum, Nature **417**, 917 (2002).

[141] C. Jian-Xin and G. Qi-Huang, Chinese Phys. **14**, 1960 (2005).

[142] K. Okada and S. Iwata, J. Chem. Phys. **112**, 1804 (2000).

[143] T. Šedivcová, P. R. Ždánská, V. Špirko, and J. Fišer, J. Chem. Phys. **124**, 214303 (2006).

[144] J. P. Bouhnik, I. Gertner, B. Rosner, Z. Amitay, O. Heber, D. Zajfman, E. Y. Sidky, and I. Ben-Itzhak, Phys. Rev. A: Atomic, Molecular, and Optical Physics **63**, 032509 (2001).

[145] B. Gaire, A. M. Sayler, P. Q. Wang, N. G. Johnson, M. Leonard, E. Parke, K. D. Carnes, and I. Ben-Itzhak, Rev. Sci. Inst. **78**, 024503 (2007).

[146] E. Liénard, M. Herbane, G. Ban, G. Darius, P. Delahaye, D. Durand, X. Fléchard, M. Labalme, F. Mauger, A. Mery, et al., Nucl. Instrum. and Methods in Phys. Res. A **551**, 375 (2005).

Appendix A

Calculation of Momentum and Error Estimation

Our experimental method for the study of laser-molecule interactions is based on coincidence three-dimensional momentum imaging. We record information on positions (x and y) and TOF (t) of each of the particles that reach the detector. We calculate velocity and hence momentum of the dissociating fragments using measured positions and time. In addition, we also calculate kinetic energy release (KER) and angular distributions usually expressed in terms of $cos\theta$, where θ is the angle between the molecular dissociation velocity and the laser polarization. Uncertainty in these quantities is related to the position and time resolution of our detector (microchannel plate and delay line hex anode).

As mentioned in Chapter 2 we can use our experimental set up under different conditions depending on the system under study, namely FFI, LFI, TFI, and LATFI. For the purpose of error estimation, we begin with the FFI.

A.1 Field free imaging (FFI)

In this method there is no external field applied, so we can write the field free equations in each direction. We begin with quantities along the x direction.

A.1.1 x direction

The displacement equation along the x direction for the first particle to hit the detector is

$$x_1 - x_{0_i} = (v_{0x_i} + v_{1x})t_1, \tag{A.1}$$

where x_1 is the measured position, t_1 is the measured time, v_{1x} is the dissociation velocity along x, v_{0x_i} is the velocity of a specific molecular ion at the dissociation point in the x direction, and x_{0_i} is the dissociation point of a specific molecular ion. In a similar way, for the second fragment we can write

$$x_2 - x_{0_i} = (v_{0x_i} + v_{2x})t_2, \tag{A.2}$$

where the parameters have similar meaning as in equation (A.1) except they are for the second particle. In addition, momentum conservation in the center of mass (CM) system allows us to write $m_1 v_{1x} + m_2 v_{2x} = 0$, where m_1 and m_2 are the masses of the first and second fragments, respectively. This implies

$$v_{2x} = -\frac{m_1}{m_2} v_{1x} = -\beta v_{1x}, \tag{A.3}$$

where $\beta \equiv \beta_{12} = \frac{m_1}{m_2}$ is the mass ratio of the fragments. Now solving these equations for v_{1x} gives

$$v_{1x} = \frac{x_1 - x_2 + v_{0x_i}(t_2 - t_1)}{t_1 + \beta t_2} = f(x_1, x_2, v_{0x_i}, t_1, t_2). \tag{A.4}$$

Here v_{1x} is a function of x_1, x_2, v_{0x_i}, t_1, t_2, and the constant β (constant in the sense that we know the mass ratio pretty well). So, we can write the uncertainty in the measurement of v_{1x} as

$$(\Delta v_{1x})^2 = \left(\frac{\partial v_{1x}}{\partial x_1}\Delta x_1\right)^2 + \left(\frac{\partial v_{1x}}{\partial x_2}\Delta x_2\right)^2 + \left(\frac{\partial v_{1x}}{\partial v_{0x_i}}\Delta v_{0x_i}\right)^2 + \left(\frac{\partial v_{1x}}{\partial t_1}\Delta t_1\right)^2 + \left(\frac{\partial v_{1x}}{\partial t_2}\Delta t_2\right)^2,$$

where Δx_1 and Δx_2 are the uncertainties in the measurement of position x_1 and x_2, respectively. These are expressed as the full width at half maximum (FWHM) of the position resolution of our delay line anode along x. Similarly, Δt_1 and Δt_2 are uncertainties in

the measurement of time and are given by the FWHM of the timing resolution of our micro-channel plate (MCP) detector. Δv_{0x_i} is the uncertainty in the calculated value of the velocity along the x direction of a molecular ion at the interaction point and is also related to the position and timing resolution as will be discussed below. We can write the partial differential as $\frac{\partial v_{1x}}{\partial x_1} = \frac{1}{t_1+\beta t_2}$, $\frac{\partial v_{1x}}{\partial x_2} = -\frac{1}{t_1+\beta t_2}$, $\frac{\partial v_{1x}}{\partial v_{0x_i}} = \frac{t_2-t_1}{t_1+\beta t_2}$, $\frac{\partial v_{1x}}{\partial t_1} = -\frac{v_{0x_i}}{t_1+\beta t_2} - \frac{x_1-x_2+v_{0x_i}(t_2-t_1)}{(t_1+\beta t_2)^2}$, $\frac{\partial v_{1x}}{\partial t_2} = \frac{v_{0x_i}}{t_1+\beta t_2} - \frac{x_1-x_2+v_{0x_i}(t_2-t_1)}{(t_1+\beta t_2)^2} \times \beta$. Substituting these parameters for uncertainty in v_{1x} and also setting $\Delta x_1{=}\Delta x_2{=}\Delta x$ and $\Delta t_1{=}\Delta t_2{=}\Delta t$, we have

$$(\Delta v_{1x})^2 = 2\left(\frac{\Delta x}{t_1+\beta t_2}\right)^2 + \left(\frac{(t_2-t_1)\Delta v_{0x_i}}{t_1+\beta t_2}\right)^2 + \left(\left(\frac{-v_{0x_i}}{t_1+\beta t_2} - \frac{x_1-x_2+v_{0x_i}(t_2-t_1)}{(t_1+\beta t_2)^2}\right)\Delta t\right)^2 + \left(\left(\frac{v_{0x_i}}{t_1+\beta t_2} - \frac{x_1-x_2+v_{0x_i}(t_2-t_1)}{(t_1+\beta t_2)^2}\beta\right)\Delta t\right)^2.$$

Before looking into the details of Δv_{1x}, let's look for v_{0x_i} and its uncertainty Δv_{0x_i}. Using equations (A.1), (A.2), and (A.3) we can write

$$v_{0x_i} = \frac{1}{1+\beta}\left[\beta\frac{x_1-x_{0_i}}{t_1} + \frac{x_2-x_{0_i}}{t_2}\right] = f(x_1, x_2, x_{0_i}, t_1, t_2), \tag{A.5}$$

and Δv_{0x_i} is given by

$$(\Delta v_{0x_i})^2 = \left(\frac{\partial v_{0x_i}}{\partial x_1}\Delta x_1\right)^2 + \left(\frac{\partial v_{0x_i}}{\partial x_2}\Delta x_2\right)^2 + \left(\frac{\partial v_{0x_i}}{\partial x_{0_i}}\Delta x_{0_i}\right)^2 + \left(\frac{\partial v_{0x_i}}{\partial t_1}\Delta t_1\right)^2 + \left(\frac{\partial v_{0x_i}}{\partial t_2}\Delta t_2\right)^2$$

where the partial derivatives are given as $\frac{\partial v_{0x_i}}{\partial x_1} = \frac{\beta}{1+\beta}\frac{1}{t_1}$, $\frac{\partial v_{0x_i}}{\partial x_2} = \frac{1}{1+\beta}\frac{1}{t_2}$, $\frac{\partial v_{0x_i}}{\partial x_{0_i}} = \frac{1}{1+\beta}(-\frac{\beta}{t_1} - \frac{1}{t_2})$, $\frac{\partial v_{0x_i}}{\partial t_1} = \frac{-\beta}{1+\beta}\frac{x_1-x_{0_i}}{t_1^2}$, $\frac{\partial v_{0x_i}}{\partial t_2} = \frac{-1}{1+\beta}\frac{x_2-x_{0_i}}{t_2^2}$.

Once the measured parameters are available we can compute the uncertainties in v_{0x_i} and then v_{1x}. The momentum component along the x direction is $p_{1x} = m_1 v_{1x}$ and the uncertainty in its measurement is given by

$$\Delta p_{1x} = \sqrt{\left(\frac{\partial p_{1x}}{\partial v_{1x}}\Delta v_{1x}\right)^2} = \sqrt{(m_1\Delta v_{1x})^2} = m_1\Delta v_{1x}. \tag{A.6}$$

Let us look at the uncertainty in KER. The KER due to the dissociation velocity along the x direction, denoted by (KER_x), is given by

$$\mathrm{KER_x} = \frac{1}{2}m_1 v_{1x}^2 + \frac{1}{2}m_2 v_{2x}^2 = \frac{1}{2}m_1 v_{1x}^2\left(1+\frac{m_1}{m_2}\right). \tag{A.7}$$

The uncertainty in $\mathrm{KER_x}$, denoted by $\Delta\mathrm{KER_x}$, is given by $\Delta\mathrm{KER_x} = \sqrt{\left(\frac{\partial \mathrm{KER_x}}{\partial v_{1x}}\Delta v_{1x}\right)^2} = m_1 v_{1x}\left(1+\frac{m_1}{m_2}\right)\Delta v_{1x}$.

A.1.2 y direction

For the FFI case the expression for the parameters along y direction are similar to those along x, however we have to use the values of these parameters along y direction. As a result the magnitudes of the parameters may vary. For example, there is a difference in the terms containing Δy_1 and Δy_2 such that we have to use the position resolution of the detector along y instead of those along x. But the position resolution of our detector is almost the same in both the x and y directions. This means we have similar uncertainty in the measured parameters along x and y direction.

For now let's continue with momentum along the z direction.

A.1.3 z direction

The components of the dissociation velocity along the z direction are calculated using the time of flight of the fragments. The TOF of the first and the second particle to reach the detector is given by

$$t_1 = \frac{d - z_i}{v_{0z_i} + v_{1z}} = \frac{d(1 - z_i'')}{v_{0z_i} + v_{1z}}, \tag{A.8}$$

$$t_2 = \frac{d - z_i}{v_{0z_i} + v_{2z}} = \frac{d(1 - z_i'')}{v_{0z_i} + v_{2z}}, \tag{A.9}$$

where d is the distance from the interaction to the detector, z_i is the initial point of the dissociation, $z_i'' = \frac{z_i}{d}$ is the scaled initial point of dissociation, v_{0z_i} is the velocity of a specific molecular ion at the dissociation point in the z direction, and v_{1z} and v_{2z} are the dissociation velocities of the first and the second fragments along the z direction, respectively. Conservation of momentum implies $m_1 v_{1z} + m_2 v_{2z} = 0$. Solving for v_{1z}, we can write $v_{1z} = \frac{1}{1+\beta_{12}}\left(\frac{d(1-z_i'')}{t_1} - \frac{d(1-z_i'')}{t_2}\right)$. For $z_i'' \ll 1$, it reduces to the form

$$v_{1z} = \frac{1}{1+\beta_{12}}\left(\frac{d}{t_1} - \frac{d}{t_2}\right) = f(t_1, t_2, d). \tag{A.10}$$

Hence, the uncertainty in v_{1z} will be

$$(\Delta v_{1z})^2 = \left(\frac{\partial v_{1z}}{\partial t_1}\Delta t_1\right)^2 + \left(\frac{\partial v_{1z}}{\partial t_2}\Delta t_2\right)^2 + \left(\frac{\partial v_{1z}}{\partial d}\Delta d\right)^2$$
$$= \left(\frac{-d}{1+\beta_{12}}\frac{\Delta t_1}{t_1^2}\right)^2 + \left(\frac{d}{1+\beta_{12}}\frac{\Delta t_2}{t_2^2}\right)^2 + \left(\frac{\Delta d}{1+\beta_{12}}\left(\frac{1}{t_1}-\frac{1}{t_2}\right)\right)^2,$$

where Δt_1 and Δt_2 are the uncertainties in the measurements of t_1 and t_2, respectively, and are given by the timing resolution of the detector as mentioned in the previous sections. Δd is the uncertainty in the measurement of the distance d. After simplifying for Δv_{1z} we can write

$$\Delta v_{1z} = \frac{d}{1+\beta_{12}}\sqrt{\left(\frac{\Delta t_1}{t_1^2}\right)^2 + \left(\frac{\Delta t_2}{t_2^2}\right)^2 + \left(\left(\frac{1}{t_1}-\frac{1}{t_2}\right)\frac{\Delta d}{d}\right)^2}. \tag{A.11}$$

Next we look for the momentum along the z direction *i.e.* $p_{1z} = m_1 v_{1z}$. So the uncertainty in p_{1z} is

$$\Delta p_{1z} = m_1 \Delta v_{1z} = m_1 \frac{d}{1+\beta_{12}}\sqrt{\left(\frac{\Delta t_1}{t_1^2}\right)^2 + \left(\frac{\Delta t_2}{t_2^2}\right)^2 + \left(\left(\frac{1}{t_1}-\frac{1}{t_2}\right)\frac{\Delta d}{d}\right)^2}. \tag{A.12}$$

The scaled velocity is defined by $u_{1z} = \frac{v_{1z}}{v_{0z_i}}$ and in general $u_{1z} \ll 1$. Let us write the expression for these variables and their uncertainties. We can solve equations (A.8) and (A.9) and use $m_1 v_{1z} + m_2 v_{2z} = 0$ for the center of mass momentum along the z direction, *i.e.* $P_{CMz_i} = M v_{0z_i} = m_1 \frac{d(1-z_i'')}{t_1} + m_2 \frac{d(1-z_i'')}{t_2}$. From this we can write, $v_{0z_i} = \frac{m_1}{M}\frac{d(1-z_i'')}{t_1} + \frac{m_2}{M}\frac{d(1-z_i'')}{t_2}$. And for $z_i'' \ll 1$,

$$v_{0z_i} \cong \frac{m_1}{M}\frac{d}{t_1} + \frac{m_2}{M}\frac{d}{t_2} = f(t_1, t_2, d) \tag{A.13}$$

The uncertainty in v_{0z_i} can be expressed as $(\Delta v_{0z_i})^2 = \left(\frac{\partial v_{0z_i}}{\partial t_1}\Delta t_1\right)^2 + \left(\frac{\partial v_{0z_i}}{\partial t_2}\Delta t_2\right)^2 + \left(\frac{\partial v_{0z_i}}{\partial d}\Delta d\right)^2$. The partial derivative terms are given by $\frac{\partial v_{0z_i}}{\partial t_1} = \frac{-m_1 d}{M t_1^2}$, $\frac{\partial v_{0z_i}}{\partial t_2} = \frac{-m_2 d}{M t_2^2}$, and $\frac{\partial v_{0z_i}}{\partial d} = \frac{m_1}{M t_1} + \frac{m_2}{M t_2}$. So, we can write

$$\Delta v_{0z_i} = \sqrt{\left(\frac{m_1}{M}\frac{d}{t_1^2}\Delta t_1\right)^2 + \left(\frac{m_2}{M}\frac{d}{t_2^2}\Delta t_2\right)^2 + \left(\left(\frac{m_1}{M}\frac{1}{t_1} + \frac{m_2}{M}\frac{1}{t_2}\right)\Delta d\right)^2} \tag{A.14}$$

The uncertainty in the scaled velocity u_{1z} is given by $(\Delta u_{1z})^2 = \left(\frac{\partial u_{1z}}{\partial v_{1z}}\Delta v_{1z}\right)^2 + \left(\frac{\partial u_{1z}}{\partial v_{0z_i}}\Delta v_{0z_i}\right)^2 = \left(\frac{1}{v_{0z_i}}\Delta v_{1z}\right)^2 + \left(\frac{-v_{1z}}{v_{0z_i}^2}\Delta v_{0z_i}\right)^2$. All the terms on the right side of this expression are known,

so we can get the numerical value of these parameters for any experimental measurements. With the numerical values it will also be easy to guess the relative importance of the individual terms as done above in the spectrometer-only case.

The KER due to the dissociation velocity along the z direction, denoted by (KER_z), is given by

$$\mathrm{KER_z} = \frac{1}{2}m_1 v_{1z}^2 + \frac{1}{2}m_2 v_{2z}^2 = \frac{1}{2}m_1 v_{1z}^2 \left(1 + \frac{m_1}{m_2}\right) \tag{A.15}$$

The uncertainty in $\mathrm{KER_z}$, denoted by $\Delta\mathrm{KER_z}$, is given by $\Delta\mathrm{KER_z} = \sqrt{\left(\frac{\partial \mathrm{KER_z}}{\partial v_{1z}}\Delta v_{1z}\right)^2} = m_1 v_{1x}\left(1 + \frac{m_1}{m_2}\right)\Delta v_{1z}$.

A.1.4 KER and cosθ

The KER is defined as in equation (2.9) *i.e.*

$$\mathrm{KER} = \frac{1}{2\mu}m_1^2 v_1^2 = \frac{1}{2\mu}(p_{1x}^2 + p_{1y}^2 + p_{1z}^2). \tag{A.16}$$

So the uncertainty in KER is denoted by ΔKER and is given by $(\Delta\mathrm{KER})^2 = \left(\frac{\partial \mathrm{KER}}{\partial p_{1x}}\Delta p_{1x}\right)^2 + \left(\frac{\partial \mathrm{KER}}{\partial p_{1y}}\Delta p_{1y}\right)^2 + \left(\frac{\partial \mathrm{KER}}{\partial p_{1z}}\Delta p_{1z}\right)^2$. Simplifying it we can write

$$\Delta\mathrm{KER} = \sqrt{\left(\frac{p_{1x}}{\mu}\Delta p_{1x}\right)^2 + \left(\frac{p_{1y}}{\mu}\Delta p_{1y}\right)^2 + \left(\frac{p_{1z}}{\mu}\Delta p_{1z}\right)^2}. \tag{A.17}$$

We define cosθ as before

$$cos\theta = \frac{p_{1z}}{\sqrt{p_{1x}^2 + p_{1y}^2 + p_{1z}^2}} = \frac{p_{1z}}{\sqrt{2\mu \mathrm{KER}}} = f(p_{1z}, \mathrm{KER}). \tag{A.18}$$

So the uncertainty in $cos\theta$ is given by $\Delta cos\theta = \sqrt{\left(\frac{\partial cos\theta}{\partial p_{1z}}\Delta p_{1z}\right)^2 + \left(\frac{\partial cos\theta}{\partial KER}\Delta KER\right)^2}$.

Next we discuss the kinematics of the longitudinal field imaging method.

A.2 Longitudinal field imaging (LFI)

When we use the LFI setup, the interaction region is within the spectrometer where the focused laser beam crosses the ion beam. The static electric field of the spectrometer allows

the separation of the fragments in their flight time to the detector and the breakup energy in the transverse direction allows the separation in their position on the detector. For this case, the displacement equations along the x and y directions are similar to that of the FFI. For time (equivalent to the z component) these equations are different as we have the static electric field of the spectrometer along the ion beam direction.

A.2.1 x direction

As the parameters v_{0x_i}, v_{1x}, p_{1x}, and KER_x and their uncertainties are similar to FFI. Here v_{1x} is given by equation (A.4) and v_{0x_i} by equation (A.5). We begin with the estimation of error on v_{0x_i} as it is needed for the error in v_{1x}. Error in v_{0x_i} is denoted by Δv_{0x_i} and is given by

$$(\Delta v_{0x_i})^2 = \left(\frac{\partial v_{0x_i}}{\partial x_1}\Delta x_1\right)^2 + \left(\frac{\partial v_{0x_i}}{\partial x_2}\Delta x_2\right)^2 + \left(\frac{\partial v_{0x_i}}{\partial x_{0_i}}\Delta x_{0_i}\right)^2 + \left(\frac{\partial v_{0x_i}}{\partial t_1}\Delta t_1\right)^2 + \left(\frac{\partial v_{0x_i}}{\partial t_2}\Delta t_2\right)^2,$$

where the partial derivatives are given as $\frac{\partial v_{0x_i}}{\partial x_1} = \frac{\beta}{1+\beta}\frac{1}{t_1}$, $\frac{\partial v_{0x_i}}{\partial x_2} = \frac{1}{1+\beta}\frac{1}{t_2}$, $\frac{\partial v_{0x_i}}{\partial x_{0_i}} = \frac{1}{1+\beta}(-\frac{\beta}{t_1} - \frac{1}{t_2})$, $\frac{\partial v_{0x_i}}{\partial t_1} = \frac{-\beta}{1+\beta}\frac{x_1 - x_{0_i}}{t_1^2}$, $\frac{\partial v_{0x_i}}{\partial t_2} = \frac{-1}{1+\beta}\frac{x_2 - x_{0_i}}{t_2^2}$.

Let us estimate the numerical values of some of the parameters that are needed later on for Δv_{1x}. For a 7 keV H_2^+ beam with spectrometer voltage V_s=1200 V, the beam energy at the interaction is $E_B = (7000 - 0.8\times1\times1200)$ eV=6040 eV=$\frac{6040}{27.2}$ a.u.=222.06 a.u.. The initial beam velocity along the ion beam direction (*i.e.* along the z-axis) is given by $v_{0z} = \sqrt{\frac{2E_B}{M}}$, where $M(= m_1 + m_2)$ is the total mass of the molecular ion. For H_2^+, $M = 2\times1836$ a.u. and hence $v_{0z} = \sqrt{\frac{2\times222.06}{2\times1836}} = 0.35$ a.u.=$0.35\times2.2\times10^6$ m/s=7.7×10^5 m/s. The total length from the interaction region (*i.e.* the point within the spectrometer where the laser and the ion beam cross each other) to the detector is $d = d_1 + d_2 = 945\times10^{-3}$ m where $d_1 = 27.3\times10^{-3}$ m is the region within the field of the spectrometer and $d_2 = 917.7\times10^{-3}$ m is the field free region. With these values the time of flight (TOF) of H^+ is $t_1 = 1.08\times10^{-6}$ s and that of the neutral is $t_2 = 1.24\times10^{-6}$ s. The energy of H^+ is given by $E_1 = \frac{m_1}{M}(7000 - 0.8\times1\times1200) + 0.8\times1\times1200$ eV=3980 eV=$\frac{3980}{27.2}$ a.u.=146.32 a.u. The dimensionless parameter (scaled energy) η_1 is defined as $\frac{0.8\times q\times V_s}{E_1}$ and is given by $\frac{0.8\times1\times1200}{3980} = 0.24$. In order to

Table A.1: *Values of different parameters using H_2^+ beam in a typical LFI measurements.*

Parameter	value	unit
Beam extraction voltage	7	kV
Spectrometer voltage (V_s)	1200	V
Beam energy at interaction (E_B)	6.04 222.06	keV a.u.
H_2^+ mass (M)	2×1836	a.u.
Initial beam velocity (v_{0z})	7.7×10^5 0.35	m/s a.u.
Interaction to detector length (d)	945	mm
Field region length (d_1)	27.3	mm
Field free region length (d_2)	917.7	mm
H^+ TOF (t_1)	1.08×10^{-6}	s
H TOF (t_2)	1.24×10^{-6}	s
H^+ energy (E_1)	146.32	a.u.
Scaled energy (η_1)	0.24	
Position resolution of detector (Δx_1 and Δy_1)	0.25	mm
Timing resolution of detector (Δt_1 and Δt_2)	0.25×10^{-9}	s

make it easy to follow the estimation, the numerical value of these parameters are listed in Table A.1.

For $x_1, x_2 \sim 10^{-3}$ m, $x_{0_i} \sim 10^{-4}$ m and $t_1, t_2 \sim 10^{-6}$ s, we have $v_{0x_i} = \frac{1}{2}[1\frac{10^{-3}}{10^{-6}} + \frac{10^{-3}}{10^{-6}}] \simeq 10^3$ m/s. In order to know which terms are significant for Δv_{0x_i} we make a rough estimate of the individual terms using position resolution $\Delta x_1 \simeq \Delta x_2 = 0.25 \times 10^{-3}$ m, $x_1 \simeq x_2 = 10^{-3}$ m, $\Delta x_{0_i} \simeq 10^{-4}$ m, $t_1 \simeq t_2 = 10^{-6}$ s, and timing resolution $\Delta t_1 \simeq \Delta t_2 = 0.25 \times 10^{-9}$ s. This gives $\Delta v_{0x_i} \approx \sqrt{\left(\frac{10^{-4}}{10^{-6}}\right)^2 + \left(\frac{10^{-4}}{10^{-6}}\right)^2 + \left(\frac{10^{-4}}{10^{-6}}\right)^2 + \left(\frac{10^{-13}}{10^{-12}}\right)^2 + \left(\frac{10^{-13}}{10^{-12}}\right)^2}$. So, we can neglect the last two terms within the square root. Then,

$$\Delta v_{0x_i} \cong \sqrt{\left(\frac{\beta}{1+\beta}\frac{1}{t_1}\Delta x_1\right)^2 + \left(\frac{1}{1+\beta}\frac{1}{t_2}\Delta x_2\right)^2 + \left(\frac{1}{1+\beta}\left(-\frac{\beta}{t_1} - \frac{1}{t_2}\right)\Delta x_{0_i}\right)^2} \qquad \text{(A.19)}$$

Here the numerical value of Δv_{0x_i} is given by

$$\Delta v_{0x_i} \cong \sqrt{\left(\frac{1}{2}\frac{0.25\times10^{-3}}{1.08\times10^{-6}}\right)^2 + \left(\frac{1}{2}\frac{0.25\times10^{-3}}{1.24\times10^{-6}}\right)^2 + \left(\frac{1}{2}\left(\frac{-1}{1.08\times10^{-6}} - \frac{1}{1.24\times10^{-6}}\right)10^{-4}\right)^2} = 1.8\times10^2 \text{ m/s}.$$

Now for uncertainty in v_{1x} we have

$$
\begin{aligned}
(\Delta v_{1x})^2 &= 2\left(\frac{\Delta x}{t_1+\beta t_2}\right)^2 + \left(\frac{(t_2-t_1)\Delta v_{0x_i}}{t_1+\beta t_2}\right)^2 + \left(\left(\frac{-v_{0x_i}}{t_1+\beta t_2} - \frac{x_1-x_2+v_{0x_i}(t_2-t_1)}{(t_1+\beta t_2)^2}\right)\Delta t\right)^2 \\
&\quad + \left(\left(\frac{v_{0x_i}}{t_1+\beta t_2} - \frac{x_1-x_2+v_{0x_i}(t_2-t_1)}{(t_1+\beta t_2)^2}\beta\right)\Delta t\right)^2 \\
&= 2\left(\frac{10^{-4}}{10^{-6}}\right)^2 + \left(\frac{10^{-5}}{10^{-6}}\right)^2 + \left(\left(\frac{10^{3}}{10^{-6}} - \frac{10^{-3}}{(10^{-6})^2}\right)10^{-10}\right)^2 \\
&\quad + \left(\left(\frac{-10^{3}}{10^{-6}} - \frac{10^{-3}}{(10^{-6})^2}\right)10^{-10}\right)^2.
\end{aligned}
$$

From the rough estimates of the parameters we need to keep only the first term and hence

$$\Delta v_{1x} \cong \sqrt{2\left(\frac{\Delta x}{t_1+\beta t_2}\right)^2} \cong \frac{\sqrt{2}}{t_1+\beta t_2}(\Delta x) \tag{A.20}$$

with $t_1+\beta t_2 = 2.32\times10^{-6}\,\mathrm{s}$, we have $\Delta v_{1x} \cong \frac{\sqrt{2}\times0.25\times10^{-3}}{2.32\times10^{-6}} = 152.39\,\mathrm{m/s}$=$6.9\times10^{-5}\,\mathrm{a.u.}$.

The momentum component along the x-direction is $p_{1x} = m_1 v_{1x}$ and its uncertainty is given (as in equation (A.6)) by

$$\Delta p_{1x} = m_1 \Delta v_{1x} \tag{A.21}$$

Then we have $\Delta p_{1x} = 1836\times6.9\times10^{-5}\,\mathrm{a.u.}$=$0.13\,\mathrm{a.u.}$.

A.2.2 y direction

For the LFI case the uncertainty in the momentum along the y direction ($p_{1y} = m_1 v_{1y}$) will be the same as along the x direction because the displacement equations of motion along the y direction are similar to those along the x direction. In addition, the position resolution of our detector is almost the same in both the x and y directions.

$$\Delta p_{1y} = \sqrt{\left(\frac{\partial p_{1y}}{\partial v_{1y}}\Delta v_{1y}\right)^2} = \sqrt{(m_1\Delta v_{1y})^2} = m_1\Delta v_{1y} \tag{A.22}$$

i.e. $\Delta p_{1y} = 1836\times6.9\times10^{-5}\,\mathrm{a.u.}$=$0.13\,\mathrm{a.u.}$.

For now let us continue with momentum along the z direction.

A.2.3 z direction

In this section we calculate the error in momentum and KER along the z direction (*i.e.* along the ion beam direction). Since we measure the TOF of the fragments, we need to get v_{1z} from the measured TOFs. The TOF of ions and neutrals is given by

$$t_1 = \frac{2d_1}{v_{0z_i}}\frac{1}{\eta_1}\left[\sqrt{(1+u_{1z})^2+\eta_1(1-z_i')}-(1+u_{1z})\right]+\frac{d_2}{v_{0z_i}}\frac{1}{\sqrt{(1+u_{1z})^2+\eta_1(1-z_i')}} \quad \text{(A.23)}$$

and

$$t_2 = \frac{d(1-z_i'')}{v_{0z_i}(1-\beta u_{1z})}, \quad \text{(A.24)}$$

where $z_i' = \frac{z_i}{d_1}$ and $z_i'' = \frac{z_i}{d}$ are the scaled initial position of the dissociation point. Also u_{1z} is the scaled dissociation velocity along the z direction, given by $u_{1z} = \frac{v_{1z}}{v_{0z_i}}$, where v_{1z} is the dissociation velocity of the first fragment along the z direction and v_{0z_i} is the velocity of a specific molecular ion at the dissociation point in the z direction. We solve these equations numerically. However, in order to estimate the error in v_{1z}, we also solve these equations for v_{1z} by expanding t_1 and t_2 to first order in u_{1z} as

$$t_1 \simeq t_i[1+bu_{1z}+O(u_{1z}^2)] \simeq t_i(1+bu_{1z}), \quad \text{(A.25)}$$

where $t_i = \frac{2d_1}{v_{0z_i}}\frac{1}{\eta_1}\left(\sqrt{1+\eta_1(1-z_i')}-1\right)+\frac{d_2}{v_{0z_i}}\frac{1}{\sqrt{1+\eta_1(1-z_i')}}$ and $bt_i = \frac{2d_1}{v_{0z_i}}\frac{1}{\eta_1}\left(\frac{1-\sqrt{1+\eta_1(1-z_i')}}{\sqrt{1+\eta_1(1-z_i')}}\right)-\frac{d_2}{v_{0z_i}}\frac{1}{(1+\eta_1(1-z_i'))^{\frac{3}{2}}}$. t_2 takes the form

$$t_2 \simeq t_n[1+\beta u_{1z}+O(u_{1z}^2)] \simeq t_n(1+\beta u_{1z}), \quad \text{(A.26)}$$

where $t_n = \frac{d}{v_{0z_i}}(1-z_i'')$. Solving these equations (A.25) and (A.26) we can write $u_{1z} = \frac{t_1-t_2-t_i+t_n}{bt_i-\beta t_n}$ and

$$v_{1z} = \frac{t_1-t_2-t_i+t_n}{bt_i-\beta t_n}v_{0z_i} = f(t_1,t_2,v_{0z_i}). \quad \text{(A.27)}$$

The uncertainty in v_{1z} is given by

$$\Delta v_{1z} = \sqrt{\left(\frac{\partial v_{1z}}{\partial t_1}\Delta t_1\right)^2+\left(\frac{\partial v_{1z}}{\partial t_2}\Delta t_2\right)^2+\left(\frac{\partial v_{1z}}{\partial v_{0z_i}}\Delta v_{0z_i}\right)^2}, \quad \text{(A.28)}$$

where the partial derivatives are given by $\frac{\partial v_{1z}}{\partial t_1} = \frac{v_{0z_i}}{bt_i - \beta t_n}$, $\frac{\partial v_{1z}}{\partial t_2} = -\frac{v_{0z_i}}{bt_i - \beta t_n}$, $\frac{\partial v_{1z}}{\partial v_{0z_i}} = \frac{t_1 - t_2 - t_i - t_n}{bt_i - \beta t_n}$, and $\Delta t_1 = \Delta t_2 = \Delta t$. Before estimating these parameters, let us find the uncertainty in v_{0z_i}. Again using the approximate solution for v_{0z_i} based on the first order expansions of t_1 and t_2 defined in equations (A.23) and (A.24), we can write

$$v_{0z_i} = \frac{d(1-z_i'')}{t_2}\left[\frac{\frac{2d_1}{d}\frac{1}{\eta_1}\left[1-\sqrt{1+\eta_1(1-z_i')}\right]\left(1+\beta\sqrt{1+\eta_1(1-z_i')}\right) - \frac{d_2}{d}\left(\beta + \frac{1}{1+\eta_1(1-z_i')}\right)}{\frac{2d_1}{d}\frac{1}{\eta_1}\left[1-\sqrt{1+\eta_1(1-z_i')}\right] - \frac{d_2}{d}\frac{1}{1+\eta_1(1-z_i')} - \beta(1-z_i'')\frac{t_1}{t_2}\sqrt{1+\eta_1(1-z_i')}}\right] \tag{A.29}$$

For z_i' and $z_i'' \ll 1$, we have $v_{0z_i} = \frac{d}{t_2}\left[\frac{\frac{2d_1}{d}\frac{1}{\eta_1}[1-\sqrt{1+\eta_1}](1+\beta\sqrt{1+\eta_1}) - \frac{d_2}{d}(\beta+\frac{1}{1+\eta_1})}{\frac{2d_1}{d}\frac{1}{\eta_1}[1-\sqrt{1+\eta_1}] - \frac{d_2}{d}\frac{1}{1+\eta_1} - \beta\frac{t_1}{t_2}\sqrt{1+\eta_1}}\right] = \frac{d[A(1+B)-C]}{At_2 - Dt_2 - dBt_1} = f(t_1, t_2, d, A, C, D)$, where $A = \frac{2d_1}{\eta_1}[1-\sqrt{1+\eta_1}]$, $B = \beta\sqrt{1+\eta_1}$, $C = d_2(\beta + \frac{1}{1+\eta_1})$, and $D = \frac{d_2}{1+\eta_1}$.

For a 7 keV H_2^+ beam with $V_s = 1200$ V, we have $t_i = \frac{2d_1}{v_{0z_i}}\frac{1}{\eta_1}[\sqrt{1+\eta_1}-1] + \frac{d_2}{v_{0z_i}}\frac{1}{\sqrt{(1+\eta_1)}} = \frac{1}{7.7\times10^5}[0.026+0.824] = 1.10\times10^{-6}$ s, $t_n = \frac{d}{v_{0z_i}} = \frac{945\times10^{-3}}{7.7\times10^5} = 1.23\times10^{-6}$ s, $bt_i = \frac{1}{\sqrt{1+\eta_1}}\{\frac{2d_1}{v_{0z_i}}\frac{1}{\eta_1}[1-\sqrt{1+\eta_1}] - \frac{d_2}{v_{0z_i}}\frac{1}{1+\eta_1}\} = \frac{0.9}{7.7\times10^5}[2\times27.3\times10^{-3}\times(-0.46) - 917.7\times10^{-3}\times0.8] = -8.9\times10^{-7}$ s, $\beta t_n = 1\times1.23\times10^{-6}$ s, $bt_i - \beta t_n = -2.12\times10^{-6}$ s, $t_1 - t_2 - t_i + t_n = -3.0\times10^{-8}$ s. With all these parameters, we have $A = \frac{2d_1}{\eta_1}[1-\sqrt{1+\eta_1}] = \frac{2\times27.3\times10^{-3}}{0.24}[1-1.11] = -0.025$, $B = \beta\sqrt{1+\eta_1} = 1\times1.11 = 1.11$, $C = d_2(\beta + \frac{1}{1+\eta_1}) = 917.7\times10^{-3}(1+0.8) = 1.65$, and $D = \frac{d_2}{1+\eta_1} = \frac{917.7\times10^{-3}}{1.24} = 0.74$. In addition, $A(1+B) - C = -0.025\times2.11 - 1.65 = -1.7$ and $At_2 - Dt_2 - dBt_1 = (-0.025\times1.24 - 0.74\times1.24 - 945\times10^{-3}\times1.11\times1.08)\times10^{-6}$ s$= -2.08\times10^{-6}$ s. In addition assuming $\Delta d_1 = \Delta d_2 = 1\times10^{-3}$ m, $\Delta A = \sqrt{(\frac{2[1-\sqrt{1+\eta_1}]}{\eta_1}\Delta d_1)^2} = \sqrt{(\frac{2[1-1.11]}{0.24}\times1\times10^{-3})^2} = 0.9\times10^{-3}$, $\Delta C = \sqrt{((\beta+\frac{1}{1+\eta_1})\Delta d_2)^2} = 1.8\times10^{-3}$, and $\Delta D = \sqrt{(\frac{\Delta d_2}{1+\eta_1})^2} = 0.8\times10^{-3}$. For a quick view, values of these parameters are listed in Table A.2.

Now the uncertainty in v_{0z_i}, denoted by Δv_{0z_i}, is given by

$$\begin{aligned}(\Delta v_{0z_i})^2 = &\left(\frac{\partial v_{0z_i}}{\partial t_1}\Delta t_1\right)^2 + \left(\frac{\partial v_{0z_i}}{\partial t_2}\Delta t_2\right)^2 + \left(\frac{\partial v_{0z_i}}{\partial d}\Delta d\right)^2 \\ &+ \left(\frac{\partial v_{0z_i}}{\partial A}\Delta A\right)^2 + \left(\frac{\partial v_{0z_i}}{\partial C}\Delta C\right)^2 + \left(\frac{\partial v_{0z_i}}{\partial D}\Delta D\right)^2\end{aligned} \tag{A.30}$$

where the partial derivatives are given by $\frac{\partial v_{0z_i}}{\partial t_1} = \frac{-d[A(1+B)-C](-dB)}{(At_2 - Dt_2 - dBt_1)^2} = -3.89\times10^{11}$, $\frac{\partial v_{0z_i}}{\partial t_2} = \frac{-d[A(1+B)-C](A-D)}{(At_2 - Dt_2 - dBt_1)^2} = 2.84\times10^{11}$, $\frac{\partial v_{0z_i}}{\partial d} = \frac{[A(1+B)-C]}{(At_2 - Dt_2 - dBt_1)} + \frac{-d[A(1+B)-C](-Bt_1)}{(At_2 - Dt_2 - dBt_1)^2} = 1.26\times10^6$,

Table A.2: *Values of different parameters for the evaluation of uncertainty along z direction*

Parameter	value	unit
t_i	1.1×10^{-6}	s
t_n	1.23×10^{-6}	s
bt_i	-8.9×10^{-7}	s
βt_n	1.23×10^{-6}	s
t_1-t_2-t_i+t_n	-3.0×10^{-8}	s
A	-0.025	m
B	1.11	
C	1.65	m
D	0.74	m
At_2-Dt_2-dBt_1	-2.08×10^{-6}	s
Δd_1=Δd_2=Δd	1	mm
ΔA	0.9×10^{-3}	m
ΔC	1.8×10^{-3}	m
ΔD	0.8×10^{-3}	m

$\frac{\partial v_{0z_i}}{\partial A} = \frac{d(1+B)}{(At_2-Dt_2-dBt_1)} + \frac{-d[A(1+B)-C](t_2)}{(At_2-Dt_2-dBt_1)^2} = -5.1\times10^5$, $\frac{\partial v_{0z_i}}{\partial C} = \frac{-d}{(At_2-Dt_2-dBt_1)} = 4.5\times10^5$, and $\frac{\partial v_{0z_i}}{\partial D} = \frac{-d[A(1+B)-C](-t_2)}{(At_2-Dt_2-dBt_1)^2} = -4.6\times10^5$. So we can write $(\Delta v_{0z_i})^2 = (-97.25)^2 + (71)^2 + (1260)^2 + (459)^2 + (810)^2 + (368)^2$. We have $\Delta v_{0z_i} = 1613\,\text{m/s} = \frac{1613}{2.2\times10^6}\,\text{a.u.} = 7.3\times10^{-4}\,\text{a.u.}$.

Also equation (A.28) can be written in the form

$$\Delta v_{1z} = \sqrt{\left(\frac{v_{0z_i}}{bt_i-\beta t_n}\Delta t_1\right)^2 + \left(\frac{-v_{0z_i}}{bt_i-\beta t_n}\Delta t_2\right)^2 + \left(\frac{t_1-t_2-t_i+t_n}{bt_i-\beta t_n}\Delta v_{0z_i}\right)^2} \tag{A.31}$$

and simplifying it we have $\Delta v_{1z} = \sqrt{\left(\frac{v_{0z_i}}{bt_i-\beta t_n}\right)^2\left(2(\Delta t)^2 + (t_1-t_2-t_i+t_n)^2\left(\frac{\Delta v_{0z_i}}{v_{0z_i}}\right)^2\right)} = \sqrt{(3.6\times10^{11})^2\,(1.25\times10^{-19}+4.1\times10^{-21})}$=129 m/s=$5.86\times10^{-5}$ a.u..

The momentum component along the z-direction is $p_{1z} = m_1 v_{1z}$ and the uncertainty in its measurement is given by

$$\Delta p_{1z} = \sqrt{\left(\frac{\partial p_{1z}}{\partial v_{1z}}\Delta v_{1z}\right)^2} = \sqrt{(m_1\Delta v_{1z})^2} = m_1\Delta v_{1z} \tag{A.32}$$

Then $\Delta p_{1z} = 1836\times5.96\times10^{-5}$ a.u.=0.107 a.u.=0.11 a.u.. The errors in the momentum components are summarized in Table A.3.

Table A.3: *Uncertainties in the momentum components*

Parameter	value	unit
$\Delta p_{1x}, \Delta p_{1y}$	0.13	a.u.
Δp_{1z}	0.11	a.u.

Next we consider the transverse field imaging case.

A.3 Transverse field imaging (TFI)

This case differs from the LFI case as the static electric field of the deflector is along the y direction. So, the displacement equation along this direction will be different from that of the FFI and LFI case. However, the displacement equations along the x and z direction will be the same as for the FFI case. That means we can use the expressions from the FFI case for the x and z direction, and for y we have to derive the expressions.

A.3.1 x direction

This is similar to the FFI case. See Sec. A.1.1.

A.3.2 z direction

This is similar to the FFI case. See Sec. A.1.3.

A.3.3 y direction

The displacement equation for the first particle along the y direction can be written as

$$y_1 - y_{0_i} = (v_{0y_i} + v_{1y})t_1 + G_d \frac{\eta_{D_1}}{(1+u_{1z})^2} \tag{A.33}$$

where y_1 is the measured position, t_1 is the measured time, v_{1y} is the dissociation velocity of the first particle in the y direction, v_{0y_i} is the velocity of a specific molecular ion at the dissociation point along the y direction, and y_{0_i} is the point of dissociation. $\eta_{D_1} = \frac{q_1 V_d}{E_{10z}}$ (in an internal document we have already defined η_1 for the spectrometer-only case so here we

use η_{D_1}) with $E_{10z} = \frac{1}{2}m_1 v_{0z_i}^2$. The geometry factor for the set up is $G_d = \frac{1}{2}\frac{L}{D}\left(d_D + \frac{L}{2}\right)$, where the length of the deflector is L(=64 mm), the separation between two outermost plates of the deflector is D(=30 mm), and the distance from the deflector edge to the detector is d_D(=668 mm) (in an internal document d_2 is already defined for some other distance so here we use d_D instead of d_2). $G_d = \frac{1}{2}\frac{64}{30}(668 + \frac{64}{2}) = 746.67$ mm. Using SIMION simulations we found that a correction factor of 1.2 is needed for the ideal deflector to match the real one, so $G_d = 1.2 \times 746.67$ mm=896 mm. The uncertainty in G_d is

$$\Delta G_d = \sqrt{\left(\frac{\partial G_d}{\partial d_D}\Delta d_D\right)^2}. \tag{A.34}$$

This is with the assumption that we know the length (L) and separation between outermost plates (D) of the deflector well and hence the main uncertainty is in d_D. So $\Delta G_d = \frac{L}{2D}\Delta d_D = \frac{64}{2\times 30} \times 1$ mm=1 mm.

In a similar way, for the second fragment we can write

$$y_2 - y_{0_i} = (v_{0y_i} + v_{2y})t_2 + G_d\frac{\eta_{D_2}}{(1+u_{2z})^2}. \tag{A.35}$$

Subtracting equation (A.35) from equation (A.33) and using $m_1 v_{1y} + m_2 v_{2y} = 0$, we have $y_1 - y_2 = v_{0y_i}(t_1 - t_2) + v_{1y}t_1 - v_{2y}t_2 + G_d\left(\frac{\eta_{D_1}}{(1+u_{1z})^2} - \frac{\eta_{D_2}}{(1+u_{2z})^2}\right)$. For two body dissociation, the second particle is a neutral and hence q_2 is zero, *i.e.* $\eta_{D_2} = 0$. Using this we can simplify for v_{1y} as

$$v_{1y} = \frac{y_1 - y_2 + v_{0y_i}(t_2 - t_1) - G_d\frac{\eta_{D_1}}{(1+u_{1z})^2}}{t_1 + \beta t_2} = f(y_1, y_2, v_{0y_i}, t_1, t_2, G_d, u_{1z}). \tag{A.36}$$

Then the uncertainty in v_{1y} can be expressed as

$$\begin{aligned}(\Delta v_{1y})^2 = &\left(\frac{\partial v_{1y}}{\partial y_1}\Delta y_1\right)^2 + \left(\frac{\partial v_{1y}}{\partial y_2}\Delta y_2\right)^2 + \left(\frac{\partial v_{1y}}{\partial v_{0y_i}}\Delta v_{0y_i}\right)^2 + \left(\frac{\partial v_{1y}}{\partial t_1}\Delta t_1\right)^2 \\ &+ \left(\frac{\partial v_{1y}}{\partial t_2}\Delta t_2\right)^2 + \left(\frac{\partial v_{1y}}{\partial G_d}\Delta G_d\right)^2 + \left(\frac{\partial v_{1y}}{\partial u_{1z}}\Delta u_{1z}\right)^2,\end{aligned}$$

where the partial derivatives are $\frac{\partial v_{1y}}{\partial y_1} = \frac{1}{t_1+\beta t_2}$, $\frac{\partial v_{1y}}{\partial y_2} = \frac{-1}{t_1+\beta t_2}$, $\frac{\partial v_{1y}}{\partial v_{0y_i}} = \frac{t_2-t_1}{t_1+\beta t_2}$, $\frac{\partial v_{1y}}{\partial t_1} = \frac{-v_{0y_i}}{t_1+\beta t_2} - \frac{y_1-y_2+v_{0y_i}(t_2-t_1)-G_d\frac{\eta_{D_1}}{(1+u_{1z})^2}}{(t_1+\beta t_2)^2}1$, $\frac{\partial v_{1y}}{\partial t_2} = \frac{v_{0y_i}}{t_1+\beta t_2} - \frac{y_1-y_2+v_{0y_i}(t_2-t_1)-G_d\frac{\eta_{D_1}}{(1+u_{1z})^2}}{(t_1+\beta t_2)^2}\beta$, $\frac{\partial v_{1y}}{\partial G_d} = \frac{-1}{t_1+\beta t_2}\frac{\eta_{D_1}}{(1+u_{1z})^2}$, $\frac{\partial v_{1y}}{\partial u_{1z}} = \frac{2}{t_1+\beta t_2}\frac{G_d\eta_{D_1}}{(1+u_{1z})^3}$.

Some of the parameters in these expressions have already been found in the discussion on for the z component (see Sec. A.3.2), which is one of the reasons the calculations along z precede those along the y direction. However, we have to calculate the velocity of a specific molecular ion at the interaction point along the y direction, *i.e.* v_{0y_i}. Using equations (A.33), (A.35), and $m_1 v_{1y} + m_2 v_{2y} = 0$ we can write $M v_{0y_i} = \frac{m_1(y_1 - y_{0_i})}{t_1} + \frac{m_2(y_2 - y_{0_i})}{t_2} - G_d \left(\frac{m_1 \eta_{D_1}}{t_1(1+u_{1z})^2} + \frac{m_2 \eta_{D_2}}{t_2(1+u_{2z})^2} \right)$. The second particle is neutral in the dissociation and this expression reduces to the form $v_{0y_i} = \frac{m_1(y_1 - y_{0_i})}{M t_1} + \frac{m_2(y_2 - y_{0_i})}{M t_2} - G_d \frac{m_1 \eta_{D_1}}{M t_1(1+u_{1z})^2} = f(y_1, y_2, y_{0_i}, t_1, t_2, G_d, u_{1z})$. So the uncertainty Δv_{0y_i} can be expressed as

$$
\begin{aligned}
(\Delta v_{0y_i})^2 = &\left(\frac{\partial v_{0y_i}}{\partial y_1} \Delta y_1 \right)^2 + \left(\frac{\partial v_{0y_i}}{\partial y_2} \Delta y_2 \right)^2 + \left(\frac{\partial v_{0y_i}}{\partial y_{0_i}} \Delta y_{0_i} \right)^2 + \left(\frac{\partial v_{0y_i}}{\partial t_1} \Delta t_1 \right)^2 \\
&+ \left(\frac{\partial v_{0y_i}}{\partial t_2} \Delta t_2 \right)^2 + \left(\frac{\partial v_{0y_i}}{\partial G_d} \Delta G_d \right)^2 + \left(\frac{\partial v_{0y_i}}{\partial u_{1z}} \Delta u_{1z} \right)^2
\end{aligned}
$$

where the partial derivatives are $\frac{\partial v_{0y_i}}{\partial y_1} = \frac{m_1}{M}\frac{1}{t_1}$, $\frac{\partial v_{0y_i}}{\partial y_2} = \frac{m_2}{M}\frac{1}{t_2}$, $\frac{\partial v_{0y_i}}{\partial y_{0_i}} = \frac{m_1}{M}\frac{-1}{t_1} + \frac{m_2}{M}\frac{-1}{t_2}$, $\frac{\partial v_{0y_i}}{\partial t_1} = \frac{m_1}{M}\frac{-(y_1 - y_{0_i})}{t_1^2} + \frac{m_1}{M} G_d \frac{\eta_{D_1}}{t_1^2(1+u_{1z})^2}$, $\frac{\partial v_{0y_i}}{\partial t_2} = \frac{-m_2}{M}\frac{(y_2 - y_{0_i})}{t_2^2}$, $\frac{\partial v_{0y_i}}{\partial G_d} = \frac{-m_1}{M}\frac{\eta_{D_1}}{t_1(1+u_{1z})^2}$, $\frac{\partial v_{0y_i}}{\partial u_{1z}} = \frac{m_1}{M}\frac{2 G_d \eta_{D_1}}{t_1(1+u_{1z})^3}$. With these expressions we can easily workout the numerical values using experimental parameters. Once v_{0y_i} and Δv_{0y_i} are known, we can get the Δv_{1y} and hence Δp_{1y}.

Now we will move on to the case of longitudinal and transverse field imaging.

A.4 Longitudinal and transverse field imaging (LATFI)

In this case the displacement equations along the x will be similar to those of the field free case. There is a static electric field of the spectrometer along the z direction and field of the deflector along the y direction. Neglecting the small correction in TOF due to the initial velocity of the particles along y, we use the displacement equations from the LFI case for the z direction.

A.4.1 x direction

This is similar to the FFI and LFI case (see Sec. A.1.1 and Sec. A.2.1). We can estimate the errors as follows.

Table A.4: *Values of different parameters using H_2^+ beam in a typical LATFI measurements.*

Parameter	value	unit
Beam extraction voltage	5	kV
Spectrometer voltage (V_s)	1200	V
Beam energy at interaction (E_B)	4.04 148.53	keV a.u.
H_2^+ mass (M)	2×1836	a.u.
Initial beam velocity (v_{0z})	6.16×10^5 0.28	m/s a.u.
Interaction to detector length (d)	945	mm
Field region length (d_1)	27.3	mm
Field free region length (d_2)	917.7	mm
H^+ TOF (t_1)	1.32×10^{-6}	s
H TOF (t_2)	1.52×10^{-6}	s
H^+ energy (E_1)	109.56	a.u.
Scaled energy (η_1)	0.32	
Position resolution of detector (Δx_1 and Δy_1)	0.25	mm
Timing resolution of detector (Δt_1 and Δt_2)	0.25×10^{-9}	s

The uncertainty in the measurement of the dissociation velocity along the x direction is given by equation (A.20). For a 5 keV H_2^+ beam with V_s=1200 V and V_d=81.1 V, we have β=1, M=2×1836 a.u., E_B=4040 eV=148.53 a.u., v_{0z}=0.28 a.u.=6.16×10^5 m/s. The times of flight of ion and neutrals are $t_1 = 1.32\times10^{-6}$ s, $t_2 = 1.52\times10^{-6}$ s, respectively. Then $t_1+\beta t_2 = 2.84\times10^{-6}$ s. And the position resolution of the detector $\Delta x = 0.25\times10^{-3}$ m. These parameters with their numerical values are listed in the Table A.4.

We have $\Delta v_{1x} = \frac{\sqrt{2}}{t_1+\beta t_2}(\Delta x) = \frac{\sqrt{2}\times0.25\times10^{-3}}{2.84\times10^{-6}} = 124.5$ m/s=$\frac{124.5}{2.2\times10^6}$ a.u.=5.7×10^{-5} a.u.. Therefore, $\Delta p_{1x} = m_1\Delta v_{1x} = 1836\times5.7\times10^{-5}$ a.u.=0.11 a.u..

Table A.5: *Values of different parameters Using LATFI method for the evaluation of uncertainty along z direction*

Parameter	value	unit
t_i	1.34×10^{-6}	s
t_n	1.53×10^{-6}	s
bt_i	-1.02×10^{-6}	s
βt_n	1.53×10^{-6}	s
t_1-t_2-t_i+t_n	-1.0×10^{-8}	s
A	-0.021	m
B	1.15	
C	1.61	m
D	0.69	m
At_2-Dt_2-dBt_1	-2.51×10^{-6}	s
$\Delta d_1=\Delta d_2=\Delta d$	1	mm
ΔA	1×10^{-3}	m
ΔC	1.8×10^{-3}	m
ΔD	0.8×10^{-3}	m

A.4.2 z direction

As in the LFI case, the uncertainty in the dissociation velocity along z direction is given by simplified form of equation (A.31), *i.e.*

$$\Delta v_{1z} = \sqrt{\left(\frac{v_{0z_i}}{bt_i - \beta t_n}\right)^2 \left(2(\Delta t)^2 + (t_1 - t_2 - t_i + t_n)^2 \left(\frac{\Delta v_{0z_i}}{v_{0z_i}}\right)^2\right)} \tag{A.37}$$

The initial velocity of a specific molecular ion at the interaction point along the z direction, *i.e.* v_{0z_i}, is given by the simplified form of equation (A.29) *i.e.*,

$$v_{0z_i} = \frac{d[A(1+B) - C]}{At_2 - Dt_2 - dBt_1} = f(t_1, t_2, d, A, C, D) \tag{A.38}$$

where $A = \frac{2d_1}{\eta_1}[1 - \sqrt{1+\eta_1}]$, $B = \beta\sqrt{1+\eta_1}$, $C = d_2(\beta + \frac{1}{1+\eta_1})$, and $D = \frac{d_2}{1+\eta_1}$. As in the LFI method, the values of these parameters are listed in Table A.5.

Let us calculate these parameters for 5 keV H_2^+ beam with $V_s = 1200$ V, and $V_d = 81.1$ V. We have $v_{0z_i} = v_{0z} = 6.16 \times 10^5$ m/s, β=1, $\eta_1 = \frac{0.8\times1\times1200}{2980} = 0.32$, $1 + \eta_1$=1.32,

$\sqrt{1+\eta_1} = 1.15$, $d = 945 \times 10^{-3}\,\mathrm{m}$, $d_1 = 27.3 \times 10^{-3}\,\mathrm{m}$, $d_2 = 917.7 \times 10^{-3}\,\mathrm{m}$. Therefore, $t_i = \frac{2d_1}{v_{0z_i}}\frac{1}{\eta_1}[\sqrt{1+\eta_1} - 1] + \frac{d_2}{v_{0z_i}}\frac{1}{\sqrt{(1+\eta_1)}} = 1.34 \times 10^{-6}\,\mathrm{s}$, $t_n = \frac{d}{v_{0z_i}} = \frac{945\times10^{-3}}{6.16\times10^5} = 1.53 \times 10^{-6}\,\mathrm{s}$, $bt_i = \frac{1}{\sqrt{1+\eta_1}}\{\frac{2d_1}{v_{0z_i}}\frac{1}{\eta_1}[1 - \sqrt{1+\eta_1}] - \frac{d_2}{v_{0z_i}}\frac{1}{1+\eta_1}\} = -1.02 \times 10^{-6}\,\mathrm{s}$, $\beta t_n = 1 \times 1.53 \times 10^{-6}\,\mathrm{s}$, $bt_i - \beta t_n = -2.55 \times 10^{-6}\,\mathrm{s}$, $t_1 - t_2 - t_i + t_n = -1.0 \times 10^{-8}\,\mathrm{s}$.

With all these parameters, we have $A = \frac{2d_1}{\eta_1}[1 - \sqrt{1+\eta_1}] = \frac{2\times27.3\times10^{-3}}{0.32}[1 - 1.15] = -0.021$, $B = \beta\sqrt{1+\eta_1} = 1 \times 1.15 = 1.15$, $C = d_2(\beta + \frac{1}{1+\eta_1}) = 917.7 \times 10^{-3}(1 + 0.76) = 1.61$, and $D = \frac{d_2}{1+\eta_1} = \frac{917.7\times10^{-3}}{1.32} = 0.69$. In addition, $A(1 + B) - C = -0.025 \times 2.11 - 1.65 = -1.66$ and $At_2 - Dt_2 - dBt_1 = (-0.021 \times 1.54 - 0.69 \times 1.52 - 945 \times 10^{-3} \times 1.15 \times 1.32) \times 10^{-6}\,\mathrm{s} = -2.51 \times 10^{-6}\,\mathrm{s}$. Also assuming $\Delta d_1 = \Delta d_2 = 1 \times 10^{-3}\,\mathrm{m}$, $\Delta A = \sqrt{(\frac{2[1-\sqrt{1+\eta_1}]}{\eta_1}\Delta d_1)^2} = \sqrt{(\frac{2[1-1.11]}{0.24} \times 1 \times 10^{-3})^2} = 1 \times 10^{-3}$, $\Delta C = \sqrt{((\beta + \frac{1}{1+\eta_1})\Delta d_2)^2} = 1.8 \times 10^{-3}$, $\Delta D = \sqrt{(\frac{\Delta d_2}{1+\eta_1})^2} = 0.8 \times 10^{-3}$.

Now the uncertainty in v_{0z_i}, denoted by Δv_{0z_i}, is given by equation (A.30)

$$(\Delta v_{0z_i})^2 = \left(\frac{\partial v_{0z_i}}{\partial t_1}\Delta t_1\right)^2 + \left(\frac{\partial v_{0z_i}}{\partial t_2}\Delta t_2\right)^2 + \left(\frac{\partial v_{0z_i}}{\partial d}\Delta d\right)^2 + \left(\frac{\partial v_{0z_i}}{\partial A}\Delta A\right)^2 + \left(\frac{\partial v_{0z_i}}{\partial C}\Delta C\right)^2 + \left(\frac{\partial v_{0z_i}}{\partial D}\Delta D\right)^2 \tag{A.39}$$

where the partial derivatives are given by $\frac{\partial v_{0z_i}}{\partial t_1} = \frac{-d[A(1+B)-C](-dB)}{(At_2-Dt_2-dBt_1)^2} = -2.7 \times 10^{11}$, $\frac{\partial v_{0z_i}}{\partial t_2} = \frac{-d[A(1+B)-C](A-D)}{(At_2-Dt_2-dBt_1)^2} = 1.77 \times 10^{11}$, $\frac{\partial v_{0z_i}}{\partial d} = \frac{[A(1+B)-C]}{(At_2-Dt_2-dBt_1)} + \frac{-d[A(1+B)-C](-Bt_1)}{(At_2-Dt_2-dBt_1)^2} = 1.04 \times 10^6$, $\frac{\partial v_{0z_i}}{\partial A} = \frac{d(1+B)}{(At_2-Dt_2-dBt_1)} + \frac{-d[A(1+B)-C](t_2)}{(At_2-Dt_2-dBt_1)^2} = -4.3 \times 10^5$, $\frac{\partial v_{0z_i}}{\partial C} = \frac{-d}{(At_2-Dt_2-dBt_1)} = 3.8 \times 10^5$, and $\frac{\partial v_{0z_i}}{\partial D} = \frac{-d[A(1+B)-C](-t_2)}{(At_2-Dt_2-dBt_1)^2} = -3.8 \times 10^5$.

So we can write $(\Delta v_{0z_i})^2 = (-67.5)^2 + (45)^2 + (1040)^2 + (-430)^2 + (668)^2 + (304)^2$. We have $\Delta v_{0z_i} = 1346\,\mathrm{m/s} = \frac{1346}{2.2\times10^6}\,\mathrm{a.u.} = 6.1 \times 10^{-4}\,\mathrm{a.u.}$.

From equation (A.37) we get $\Delta v_{1z} = \sqrt{(2.42 \times 10^{11})^2\,(1.25 \times 10^{-19} + 4.8 \times 10^{-22})} = 86\,\mathrm{m/s} = 4 \times 10^{-5}\,\mathrm{a.u.}$.

The momentum component along the z-direction is $p_{1z} = m_1 v_{1z}$ and the uncertainty in its measurement is given by $\Delta p_{1z} = 1836 \times 4 \times 10^{-5}\,\mathrm{a.u.} = 0.073\,\mathrm{a.u.} \cong 0.1\,\mathrm{a.u.}$.

A.4.3 y direction

The expressions used along the y direction require some modifications as the velocity of the ion beam and the individual ions entering the deflector field is different compared to the TFI method because of the static field of the spectrometer at the interaction region. The displacement equations along the y direction are given by equation (A.33) and equation (A.35) as

$$y_1 - y_{0_i} = (v_{0y_i} + v_{1y})t_1 + G_d \frac{\eta'_{D_1}}{(1+u_{1z_d})^2} \tag{A.40}$$

and

$$y_2 - y_{0_i} = (v_{0y_i} + v_{2y})t_2 + G_d \frac{\eta'_{D_2}}{(1+u_{2z_d})^2} \tag{A.41}$$

where the parameters have a similar meaning as defined in section A.3.3 except for the scaled energy η_{D_1} and η_{D_2}. Here we define $\eta'_{D_1} = \frac{q_1 V_d}{E_{10z_d}}$ (we have already defined η_1 for the LFI method and η_{D_1} for the TFI method, so here we use η'_{D_1}) with $E_{10z_d} = \frac{1}{2}m_1 v_{0z_d}^2 = \frac{1}{2}m_1 v_{0z_i}^2 + q_1 V(z_i)$. In addition, $u_{1z_d} = \frac{v_{1z}}{v_{0z_d}}$ where $v_{0z_d} = \sqrt{v_{0z_i}^2 + \frac{2q_1 V(z_i)}{m_1}}$. The parameters for the second particle are defined in a similar way by using the charge, mass, and velocity of the second particle.

For two-body dissociation the second particle is neutral and hence q_2 is zero, which implies $\eta'_{D_2} = 0$. We can write v_{1y} as (in a way similar to equation (A.36))

$$v_{1y} = \frac{y_1 - y_2 + v_{0y_i}(t_2 - t_1) - G_d \frac{\eta'_{D_1}}{(1+u_{1z_d})^2}}{t_1 + \beta t_2} = f(y_1, y_2, v_{0y_i}, t_1, t_2, G_d, u_{1z_d}). \tag{A.42}$$

Then the uncertainty in v_{1y} can be expressed as

$$\begin{aligned}(\Delta v_{1y})^2 = &\left(\frac{\partial v_{1y}}{\partial y_1}\Delta y_1\right)^2 + \left(\frac{\partial v_{1y}}{\partial y_2}\Delta y_2\right)^2 + \left(\frac{\partial v_{1y}}{\partial v_{0y_i}}\Delta v_{0y_i}\right)^2 + \left(\frac{\partial v_{1y}}{\partial t_1}\Delta t_1\right)^2 \\ &+ \left(\frac{\partial v_{1y}}{\partial t_2}\Delta t_2\right)^2 + \left(\frac{\partial v_{1y}}{\partial G_d}\Delta G_d\right)^2 + \left(\frac{\partial v_{1y}}{\partial u_{1z_d}}\Delta u_{1z_d}\right)^2,\end{aligned}$$

where the partial derivatives are $\frac{\partial v_{1y}}{\partial y_1} = \frac{1}{t_1+\beta t_2}$, $\frac{\partial v_{1y}}{\partial y_2} = \frac{-1}{t_1+\beta t_2}$, $\frac{\partial v_{1y}}{\partial v_{0y_i}} = \frac{t_2-t_1}{t_1+\beta t_2}$, $\frac{\partial v_{1y}}{\partial t_1} = \frac{-v_{0y_i}}{t_1+\beta t_2} - \frac{y_1-y_2+v_{0y_i}(t_2-t_1)-G_d\frac{\eta'_{D_1}}{(1+u_{1z_d})^2}}{(t_1+\beta t_2)^2}1$, $\frac{\partial v_{1y}}{\partial t_2} = \frac{v_{0y_i}}{t_1+\beta t_2} - \frac{y_1-y_2+v_{0y_i}(t_2-t_1)-G_d\frac{\eta'_{D_1}}{(1+u_{1z_d})^2}}{(t_1+\beta t_2)^2}\beta$, $\frac{\partial v_{1y}}{\partial G_d} = \frac{-1}{t_1+\beta t_2}\frac{\eta'_{D_1}}{(1+u_{1z_d})^2}$, and $\frac{\partial v_{1y}}{\partial u_{1z_d}} = \frac{2}{t_1+\beta t_2}\frac{G_d\eta'_{D_1}}{(1+u_{1z_d})^3}$.

Some of the parameters in these expressions have already been found in the expressions for the z component, which is one of the reasons the calculations along z precede those of the y direction. The uncertainty in the G_d is given by equation (A.34) as $\Delta G_d = \sqrt{\left(\frac{\partial G_d}{\partial d_D}\Delta d_D\right)^2}$ with the assumption that we know length and width of the deflector well and hence the main uncertainty is in d_D. So $\Delta G_d = \frac{L}{2D}\Delta d_D = \frac{64}{2\times 30} \times 1\,\text{mm}$=1 mm.

We also have to calculate the the velocity of specific molecular ion at the interaction along the y direction *i.e.* v_{0y_i}. We can write, $v_{0y_i} = \frac{m_1(y_1-y_{0_i})}{Mt_1} + \frac{m_2(y_2-y_{0_i})}{Mt_2} - G_d\frac{m_1\eta'_{D_1}}{Mt_1(1+u_{1z_d})^2} = f(y_1, y_2, y_{0_i}, t_1, t_2, G_d, u_{1z_d})$. So the uncertainty in v_{0y_i} can be written as

$$(\Delta v_{0y_i})^2 = \left(\frac{\partial v_{0y_i}}{\partial y_1}\Delta y_1\right)^2 + \left(\frac{\partial v_{0y_i}}{\partial y_2}\Delta y_2\right)^2 + \left(\frac{\partial v_{0y_i}}{\partial y_{0_i}}\Delta y_{0_i}\right)^2 + \left(\frac{\partial v_{0y_i}}{\partial t_1}\Delta t_1\right)^2 + \left(\frac{\partial v_{0y_i}}{\partial t_2}\Delta t_2\right)^2 + \left(\frac{\partial v_{0y_i}}{\partial G_d}\Delta G_d\right)^2 + \left(\frac{\partial v_{0y_i}}{\partial u_{1z_d}}\Delta u_{1z_d}\right)^2.$$

The partial derivative terms can be written as $\frac{\partial v_{0y_i}}{\partial y_1} = \frac{m_1}{M}\frac{1}{t_1}$, $\frac{\partial v_{0y_i}}{\partial y_2} = \frac{m_2}{M}\frac{1}{t_2}$, $\frac{\partial v_{0y_i}}{\partial y_{0_i}} = \frac{m_1}{M}\frac{-1}{t_1} + \frac{m_2}{M}\frac{-1}{t_2}$, $\frac{\partial v_{0y_i}}{\partial t_1} = \frac{m_1}{M}\frac{-(y_1-y_{0_i})}{t_1^2} + \frac{m_1}{M}G_d\frac{\eta'_{D_1}}{t_1^2(1+u_{1z_d})^2}$, $\frac{\partial v_{0y_i}}{\partial t_2} = \frac{-m_2}{M}\frac{(y_2-y_{0_i})}{t_2^2}$, $\frac{\partial v_{0y_i}}{\partial G_d} = \frac{-m_1}{M}\frac{\eta'_{D_1}}{t_1(1+u_{1z_d})^2}$, and $\frac{\partial v_{0y_i}}{\partial u_{1z_d}} = \frac{m_1}{M}\frac{2G_d\eta'_{D_1}}{t_1(1+u_{1z_d})^3}$.

These are the necessary expressions for all the required parameters for the evaluation of the uncertainty in the measurement of the dissociation velocity along the y direction. Let us calculate the numerical values for the experimental conditions.

For a 5 keV H_2^+ beam with $V_s = 1200\,\text{V}$ and $V_d = 81.1\,\text{V}$, we have $E_B = (5000 - 0.8 \times 1 \times 1200) = 4040\,\text{eV}$ =148.53 a.u., $E_1 = (\frac{4040}{2} + 0.8 \times 1 \times 1200) = 2980\,\text{eV}$ =109.56 a.u., β=1, $t_1 = 1.32\times10^{-6}\,\text{s}$, $t_2 = 1.52\times10^{-6}\,\text{s}$, $t_i = 1.34\times10^{-6}\,\text{s}$, $bt_i = -1.02\times10^{-6}\,\text{s}$, $t_n = 1.53\times10^{-6}\,\text{s}$, $bt_i - t_n = -2.55 \times 10^{-6}\,\text{s}$, $t_1 - t_2 - t_i + t_n = -1.0 \times 10^{-8}\,\text{s}$, $t_1 + \beta t_2 = -2.84 \times 10^{-6}\,\text{s}$, $\eta_1 = 0.32$, $1 + \eta_1 = 1.32$, $\sqrt{1+\eta_1} = 1.15$, $\eta'_{D_1} = \frac{q_1\times V_d}{E_1} = \frac{81.1}{2980} = 0.027$. Then we can also write $v_{1z} = \frac{t_1-t_2-t_i+t_n}{bt_i-\beta t_n}v_{0z_i} = 2.42 \times 10^3\,\text{m/s}$ and the uncertainty as obtained above as $\Delta v_{1z} = 86\,\text{m/s}$.

We know that $v_{0z_d}^2 = v_{0z_i}^2 + \frac{2q_1V(z_i)}{m_1}$. This gives $v_{0z_d}^2 = (6.16 \times 10^5)^2 + \frac{2\times1.6\times10^{-19}\times0.8\times1200}{1.67\times10^{-27}}$ *i.e.* $v_{0z_d} = 7.51 \times 10^5\,\text{m/s}$. The uncertainty in v_{0z_d} is denoted by Δv_{0z_d} and is given by $(\Delta v_{0z_d})^2 = \left(\frac{\partial v_{0z_d}}{\partial v_{0z_i}}\Delta v_{0z_i}\right)^2 + \left(\frac{\partial v_{0z_d}}{\partial V(z_i)}\Delta V(z_i)\right)^2$. Assuming $\Delta V(z_i) = 1\,V$ and simplifying

for the numerical value, we get $\Delta v_{0z_d} = 1118.03\,\mathrm{m/s}$. So $u_{1z_d} = \frac{v_{1z}}{v_{0z_d}} = 3.22 \times 10^{-3}$ and the uncertainty in its value, Δu_{1z} is given by $(\Delta u_{1z_d})^2 = \left(\frac{\partial u_{1z_d}}{\partial v_{1z}}\Delta v_{1z}\right)^2 + \left(\frac{\partial u_{1z_d}}{\partial v_{0z_d}}\Delta v_{0z_d}\right)^2$. Simplifying for the numerical value one can get $\Delta u_{1z_d} = 1.15 \times 10^{-4}$.

Let us look at the relative contribution of the individual terms in the Δv_{0y_i}

$$(\Delta v_{0y_i})^2 = \left(\frac{10^{-4}}{10^{-6}}\right)^2 + \left(\frac{10^{-4}}{10^{-6}}\right)^2 + \left(\frac{2\times10^{-4}}{10^{-6}}\right)^2 + \left(\left(\frac{10^{-3}}{10^{-12}} - \frac{10^{-1}\times10^{-2}}{10^{-12}}\right)\times10^{-10}\right)^2 + \left(\frac{10^{-3}}{10^{-12}}\times10^{-10}\right)^2 + \left(\frac{10^{-2}\times10^{-3}}{10^{-6}}\right)^2 + \left(\frac{10^{-1}\times10^{-2}\times10^{-3}}{10^{-6}}\right)^2.$$

With this we can keep only the first three terms *i.e.*

$$(\Delta v_{0y_i})^2 = \left(\frac{\partial v_{0y_i}}{\partial y_1}\Delta y_1\right)^2 + \left(\frac{\partial v_{0y_i}}{\partial y_2}\Delta y_2\right)^2 + \left(\frac{\partial v_{0y_i}}{\partial y_{0_i}}\Delta y_{0_i}\right)^2. \tag{A.43}$$

Simplifying this we can write $(\Delta v_{0y_i})^2 = \left(\frac{m_1}{M}\frac{\Delta y_1}{t_1}\right)^2 + \left(\frac{m_2}{M}\frac{\Delta y_2}{t_2}\right)^2 + \left(\left(-\frac{m_1}{M}\frac{1}{t_1} - \frac{m_2}{M}\frac{1}{t_2}\right)\Delta y_{0_i}\right)^2$. With the position resolution of the detector $\Delta y = 0.25 \times 10^{-3}\,\mathrm{m}$ and $\Delta y_{0_i} = 10^{-4}\,\mathrm{m}$, we have $(\Delta v_{0y_i})^2 = \left(\frac{1}{2}\frac{2.5\times10^{-4}}{1.32\times10^{-6}}\right)^2 + \left(\frac{1}{2}\frac{2.5\times10^{-4}}{1.52\times10^{-6}}\right)^2 + \left(\frac{1}{2}\left(\frac{1}{1.32\times10^{-6}} + \frac{1}{1.52\times10^{-6}}\right)10^{-4}\right)^2$. This gives $\Delta v_{0y_i} = 144.1\,\mathrm{m/s}$=$6.5 \times 10^{-5}\,\mathrm{a.u.}$.

Now we will look for the contribution of individual terms for Δv_{1y}.

$$\begin{aligned}(\Delta v_{1y})^2 &= \left(\frac{\partial v_{1y}}{\partial y_1}\Delta y_1\right)^2 + \left(\frac{\partial v_{1y}}{\partial y_2}\Delta y_2\right)^2 + \left(\frac{\partial v_{1y}}{\partial v_{0y_i}}\Delta v_{0y_i}\right)^2 + \left(\frac{\partial v_{1y}}{\partial t_1}\Delta t_1\right)^2 \\ &\quad + \left(\frac{\partial v_{1y}}{\partial t_2}\Delta t_2\right)^2 + \left(\frac{\partial v_{1y}}{\partial G_d}\Delta G_d\right)^2 + \left(\frac{\partial v_{1y}}{\partial u_{1z_d}}\Delta u_{1z_d}\right)^2 \\ &= \left(10^2\right)^2 + \left(10^2\right)^2 + \left(10^1\right)^2 \\ &\quad + \left(10^{-1}\right)^2 + \left(10^{-1}\right)^2 + \left(10^1\right)^2 + \left(10^{-1}\right)^2.\end{aligned}$$

Here the main factors are the position resolution terms. So we can write, $(\Delta v_{1y})^2 = \left(\frac{\partial v_{1y}}{\partial y_1}\Delta y_1\right)^2 + \left(\frac{\partial v_{1y}}{\partial y_2}\Delta y_2\right)^2 = \left(\frac{1}{t_1+\beta t_2}\Delta y_1\right)^2 + \left(\frac{-1}{t_1+\beta t_2}\Delta y_2\right)^2$. Then $\Delta v_{1y} = \frac{\sqrt{2}}{t_1+\beta t_2}\Delta y = \frac{1.4\times2.5\times10^{-4}}{2.84\times10^{-6}} = 124.5\,\mathrm{m/s}$=$5.7 \times 10^{-5}\,\mathrm{a.u.}$.

The momentum component along the y direction is $p_{1y} = m_1 v_{1y}$ and the uncertainty in its measurement is given by $\Delta p_{1y} = m_1 \Delta v_{1y}$. Then $\Delta p_{1y} = 1836 \times 5.7 \times 10^{-5}\,\mathrm{a.u.}$=$0.11\,\mathrm{a.u.}$. This value is the same as that of the Δp_{1x} (see Table A.6). This is because the dominant

Table A.6: *Uncertainties in the momentum components in the LATFI method*

Parameter	value	unit
Δp_{1x}	0.11	a.u.
Δp_{1z}	0.1	a.u.
Δp_{1y}	0.11	a.u.

contribution of the error in both cases is from the position resolution of the detector, which is the same for x and y directions.

Appendix B

Details of spectrometer and deflector

We introduced the different imaging methods in Chapter 2. Except for field-free imaging, a static electric field is applied to separate the fragments, *i.e.* either longitudinal (in LFI) or transverse (in TFI) or a combination of both (in LATFI). The longitudinal and transverse fields are provided by an electrostatic spectrometer and a parallel plate deflector, respectively. A schematic of the setup with both spectrometer and deflector is shown in Fig. B.1. The laser beam crosses the ion beam within the spectrometer.

The spectrometer consists of stainless steel rings (1 mm in thickness and 60 mm outer diameter). The inner diameter of the rings is 30 mm except for the first and the fifth rings which have 2 mm diameter apertures as shown in Fig. B.2 (details are presented in [65]). The rings are stacked with 4 mm separation and the stack is aligned such that their axis lies close to the ion beam axis. The rings at the entrance and exit of the ion beam are kept at ground (0 V) potential. The spectrometer voltage (V_s) with respect to ground is applied to the fifth plate, and the other plates are connected to each other with resistors to produce a uniform field. This sets the voltage at the interaction to be $0.8 \times V_s$. The static electric field produced by this spectrometer is directed along the spectrometer axis and accelerates ions compared to the neutrals.

The details of the electrostatic deflector, used in the TFI and LATFI methods, are as follows. This deflector consists of two parallel plates separated by 30 mm (Fig. B.3(a)) with extra five plates of thickness 1 mm equally spaced by 4 mm from each other (see Fig. B.3(b))

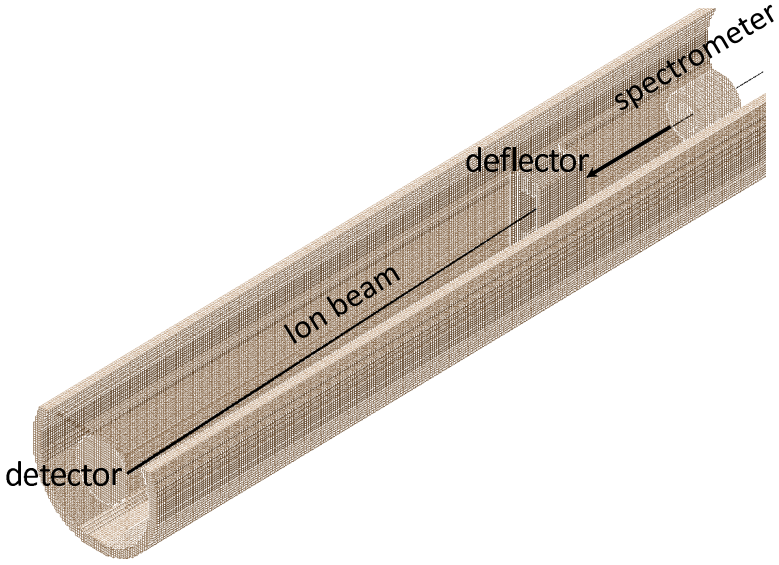

Figure B.1: *Schematic diagram, generated using SIMION, showing the spectrometer and deflector. The arrow is pointing the direction of the ion beam.*

in order to produce a uniform field and reduce the fringe field. There are two guard electrodes of thickness 3.175 mm and in addition ground metallic strips are used to keep the pieces together and also to prevent the charging of the ceramic balls by scattered ions. The length (L) of the deflector along the ion beam is 64 mm, the height (H) is 114 mm (along the vertical direction in the lab), and the width (D) is 30 mm (the separation between the parallel plates, parallel to the laser propagation). The static electric field of the deflector is thus parallel to the laser propagation direction.

The deflection of an ion in the electric field of an ideal electrostatic parallel plate deflector is given by, $y = \frac{L}{2D}\frac{q_j V_d}{\frac{1}{2}m_j(v_{0zi}+v_{jz})^2}(\frac{L}{2}+d_D)$, where q_j is the charge of an ion, V_d is the voltage difference between the two extreme plates, m_j is the mass of the ion, v_{ozi} is the initial velocity of the ion fragment at the interaction (assuming no longitudinal field in the spectrometer, i.e. the TFI method), v_{jz} is the fragment velocity resulting from the breakup of the ion, and d_D is the distance from the deflector exit to the detector, *i.e.* the field free region. We write the geometry factor for the electrostatic deflector as $G_d = \frac{1}{2}\frac{L}{D}\left(d_D + \frac{L}{2}\right)$ where

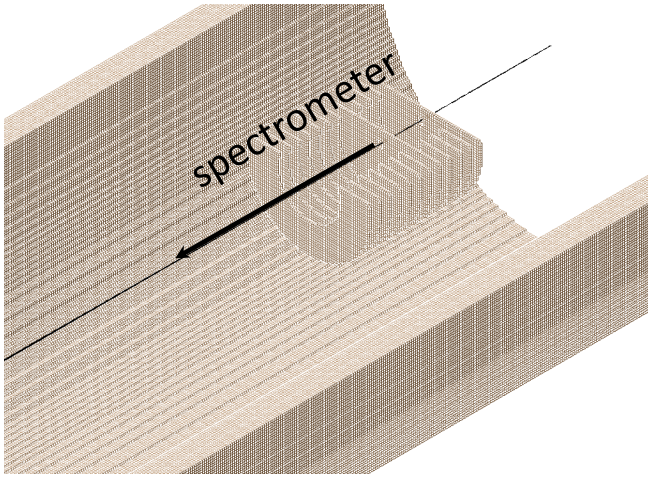

Figure B.2: *Schematic diagram showing the spectrometer. The static electric field generated by this spectrometer allows the separation of the fragments by their TOF in the LFI and LATFI methods.*

the quantities on the right are already defined. In addition, we usually refer to the ratio $\frac{q_j V_d}{\frac{1}{2}m_j(v_{0zi}+v_{jz})^2} = \frac{q_j V_d}{E_j}$ as a scaled energy ratio.

We have measured the deflection of protons (H^+) and compared them with the calculations using the ideal deflector formula and the values obtained from SIMION simulations as shown in Fig. B.4(a). The SIMION results are closer to the measurements. The differences in the real and ideal cases suggest the need for corrections. We find that using a scaling factor of 1.2 matches the two cases as shown in Fig. B.4(b). This is equivalent to having a virtual deflector with a longer length compared to the real deflector.

In addition to the scaling factor, we also have small distortions in the y deflections and TOF of the ions due to the fringe field of the deflector. The ions are deflected upon entering and leaving the fringe field region of the deflector, and typically these two deflections do not cancel each other, leading to distortions. The correction terms are found using SIMION simulations resulting in

$$y = 1.2 \times \frac{L}{2D}\frac{q_j V_d}{\frac{1}{2}m_j(v_{0z_i}+v_{jz})^2}(\frac{L}{2}+d_2) + v_{0y_i}t_{measured} \tag{B.1}$$

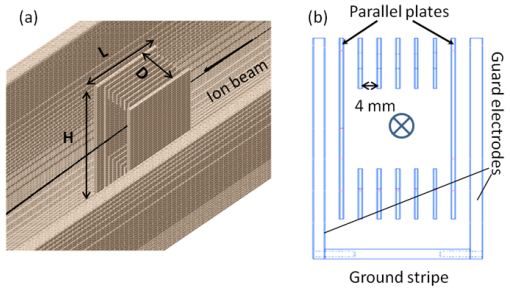

Figure B.3: *Diagram showing deflector (a) using SIMION and (b) schematic geometry with the plates. This deflector is used in the TFI and LATFI methods. The ion beam is into the page as indicated with a cross in (b).*

where $t_{measured}$ is the TOF obtained using the SIMION simulations. In a similar way, the corrections in t are given by a third order polynomial

$$t_{measured} = \frac{d}{v_{0z_i}} + 3092x^3 + 283.74x^2 - 2.1394x \tag{B.2}$$

where x is the scaled energy ratio $\frac{q_i V_d}{E_i}$.

Note that in the LATFI measurements, *i.e.* using both spectrometer and deflector, the expression for the deflection of a charged particle, e.g. equation (B.1), needs to be corrected in order to account for the fact that the ion velocity reaching the deflector field v_{0zd} is different than its velocity at the interaction (v_{0z_i}), that is

$$v_{0z_d} = \sqrt{\frac{2q_i V(z_i)}{m_i} + v_{0z_i}^2}, \tag{B.3}$$

where $V(z_i)$ is the voltage at the interaction, and q_i and m_i are the charge and mass of the ion, respectively. Obviously, for the TFI measurements, there is no voltage in the spectrometer and hence $V(z_i)$=0. This gives v_{0zd}=v_{0z_i}.

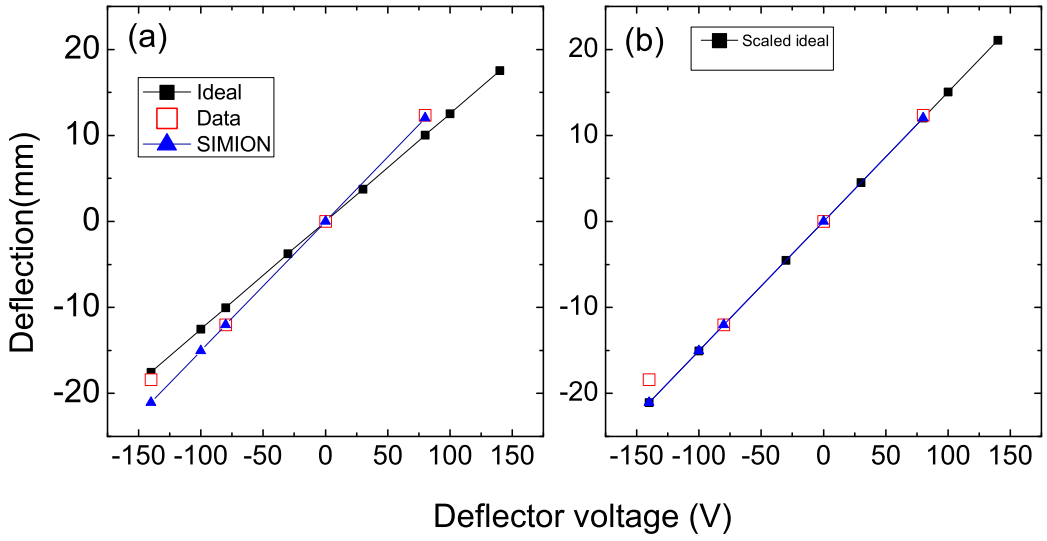

Figure B.4: *(a) Deflection of the ions from experimental measurements, ideal deflector calculations, and SIMION simulations. (b) Deflections for the ideal deflector calculations are scaled by 1.2 in order to match the data and SIMION simulations.*

Appendix C

Channel separation in TFI measurements

Imaging experiments employing only transverse field *i.e.* using the TFI method, require a different way to separate the breakup channels than that used in the longitudinal field imaging (LFI) case. The main challenge is that we do not know the order of the hits as all the fragments have almost the same TOF, as shown in Fig. C.1 (c) and (d). Here are the steps we use for channel separation, e.g. dissociation and ionization, and also to determine the order of the hits, e.g. the first or the second fragment to reach the detector within the same channel, in the TFI method:

1. We find the x and y positions in the lab coordinate from the measured positions of the hit on the detector (x, y) and the rotation angle of the detector delay line anode (the raw and rotated xy density plots are shown in Fig. C.1 (a) and (b)). These figures are generated, by the screen capture of the data analysis program called SpecTcl, in order to demonstrate the steps involved in the channel separation. Using x (and y), we find the X_{CM} (and Y_{CM}), for the two different time order of the pair of hits, specifically,

$$X_{CM_{12}} = \frac{m_1 x_1(t) + m_2 x_2(t)}{m_1 + m_2} \tag{C.1}$$

$$X_{CM_{21}} = \frac{m_2 x_1(t) + m_1 x_2(t)}{m_1 + m_2} \tag{C.2}$$

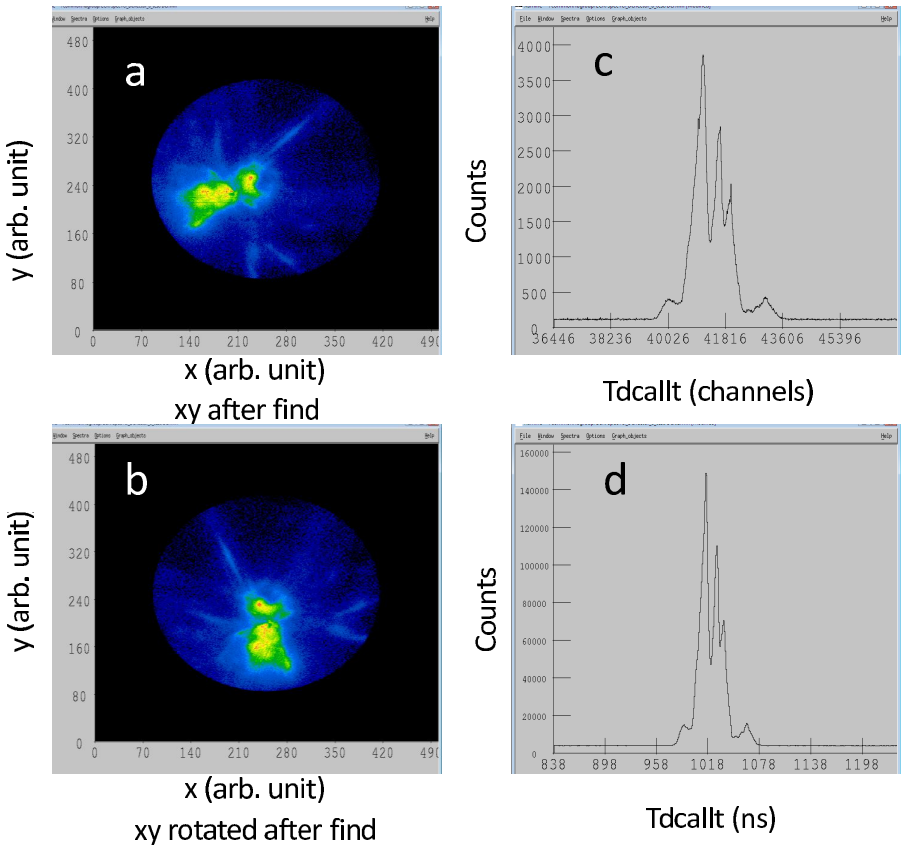

Figure C.1: *Detector image for position XY of fragment pairs (a) before and (b) after rotation (using rotation angle of the detector in the lab co-ordinate) and TOF of fragments (c) in channels and (d) in ns using the TFI measurements. Figures are taken from the screen image of the data analysis programm, called SpecTcl.*

We then plot all the possible values of X_{CM} (and Y_{CM}) in order to separate real dissociation and ionization events from the false pair of hits. As indicated in the equations, each CM should be calculated using positions measured at the same time. In the TFI method, however t_1 and t_2 are nearly equal and allow us to approximate the CM by using the measured x_1 and x_2, even though they are technically measured at different times.

2. In the density plots of X_{CM} versus Y_{CM} shown in Fig. C.2, we can see the distinct dissociation and ionization CMs. Then, we find the mass ratio (β) using the measured

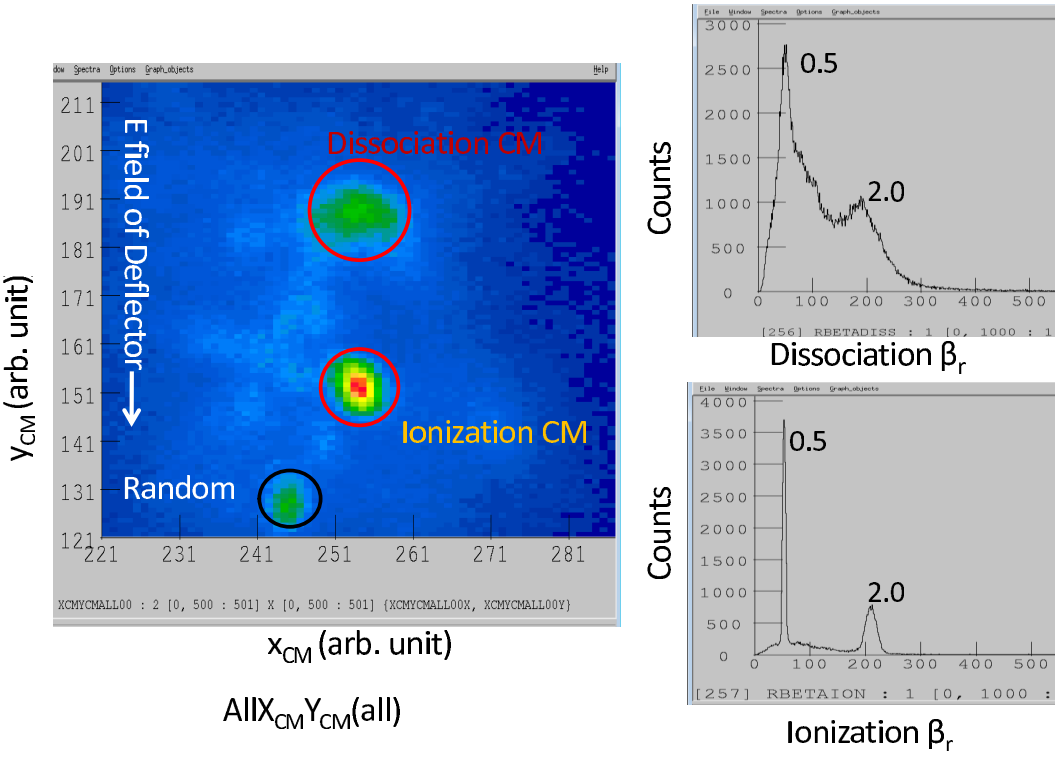

Figure C.2: *Plots of X_{CM}, Y_{CM} and β_r in the TFI measurements for heteronuclear HD^+ molecule. Figures are taken from the screen image of the data analysis programm, called SpecTcl. The β_r plot (scaled up by 100 so 50 is 0.5) indicates that we have better separation in ionization than in dissociation as the ionization fragments have higher energy from the breakup.*

position and time information. We define β_r as

$$\beta_r = \sqrt{\frac{(x_2 - X_{CM})^2 + (y_2 - Y_{CM})^2 + (v_{0z}(t_2 - T_{CM}))^2}{(x_1 - X_{CM})^2 + (y_1 - Y_{CM})^2 + (v_{0z}(t_1 - T_{CM}))^2}} \tag{C.3}$$

We use dissociation and ionization CMs (values evaluated directly from Fig. C.2 when using the program) for the beta of dissociation and ionization, respectively. Setting gates on β_r will reduce the background from false pairs of hits as shown in Fig. C.3.

3. We calculate the difference $(y_1 - y_2)$ and sum $(y_1 + y_2)$ in y for all possible combinations of the events, that have satisfied the CM and beta gates, and plot them, as shown in the upper panels of Fig. C.3. One can see the tilted stripes, which are horizontal for

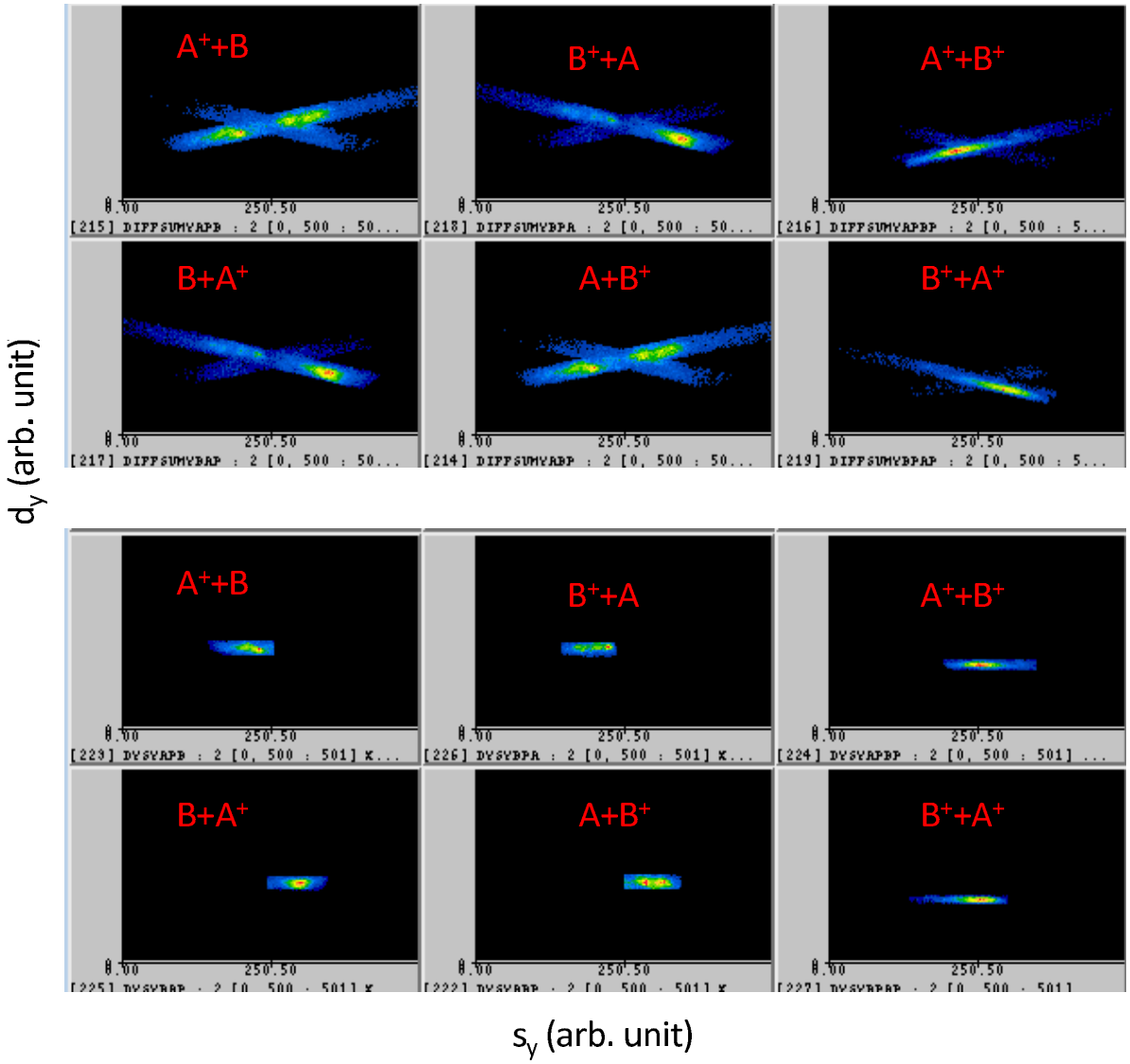

Figure C.3: *Plots of difference and sum of the measured y values of the two hits, upper pannels for uncorrected mass ratio and the lower panels with correct mass ratio.*

homonuclear molecules. But for heteronuclear molecules, we need to scale them with the correct mass ratio, β. That is we define $d_y(= \beta y_1 - y_2)$ and $s_y(= \beta y_1 + y_2)$, and then plot these parameters as a density plot. The plots are shown in the lower panel of Fig. C.3. Now only channels with the correct mass ratio, hence correct order, are horizontal. We set the gates using these new variables, d_y and s_y, and finalize the identification process of all channels.

4. Once the channels are separated and gated properly, we use the right position and time information of each event to evaluate the momentum of the fragments as described in Appendix A.

Appendix D

Normalization of different data sets

When comparing data sets measured under different experimental conditions we need to normalize them to each other in order to keep the number of molecules exposed per laser pulse similar. Here we explain this normalization procedure.

The number of target ions exposed to the laser pulses during the whole measurementtime, T is given by

$$N = \int_0^T f_{rep}\, n\, A\, dy\, \Delta t \tag{D.1}$$

where f_{rep} is the repetition rate of the laser, A is the interaction area in the lab vertical xz plane, dy is the horizontal ion beam width, and Δt is the time step for recording the signals. n is the ion beam current density, related to the ion beam particle current (I/q) as

$$I/q = n\, dx\, dy\, v_B \tag{D.2}$$

where q is the charge of the ions, dx is the vertical ion beam width and v_B is the ion beam velocity. Substituting n from equation (D.2) into equation (D.1) yields

$$N = \int_0^T f_{rep} \frac{I}{q\, dx\, dy\, v_B} A\, dy\, dt = \frac{f_{rep}\, A}{q\, dx\, v_B} \int_0^T I\, dt \tag{D.3}$$

The expression on the right side is obtained by assuming that the area, beam velocity, and size of the ion beam is not changing with time during the collection of the data.

We obtain the parameters in equation (D.3) with assumptions as follows:

1. The ion current is measured by the Faraday cup and the signal is recorded. This signal is integrated over the duration of the measurement to yield $\int_0^T I\,dt$.

2. The laser signal is also recorded using the output of a photodiode exposed to a reflected beam (e.g. from a half wave plate, used to change desired the laser polarization). We get f_{rep} by repeatedly integrating the photodiode signal over 1 second intervals, although we note that f_{rep} is very stable and does not change significantly over the course of a measurement.

3. We assume the laser beam has a Gaussian profile with the area $\pi\omega^2$.

4. We assume the laser intensity is not changing much along the laser propagation direction. This is fulfilled when $2z_R \gg dy$, where z_R is the Rayleigh range, – typically the case in our measurements.

5. We assume the laser beam size is smaller compared to the vertical ion beam width *i.e.* $\omega \ll dx$.

To conclude, the normalization factor between two measurements is given by

$$F = \frac{\frac{f_{rep_1} A_1}{q_1\, dx_1\, v_{B_1}} \int_0^{T_1} I_1\, dt}{\frac{f_{rep_2} A_2}{q_2\, dx_2\, v_{B_2}} \int_0^{T_2} I_2\, dt} \tag{D.4}$$

Note that when using the same laser beam $f_{rep_1} = f_{rep_2}$, and same ion beam $q_1 = q_2$, $v_{B_1} = v_{B_2}$, $dx_1 = dx_2$, $I_1 = I_2$, and $\frac{A_1}{A_2} = 1$ when reducing the laser intensity by using a neutral density filter or $\frac{A_1}{A_2} \neq 1$, when moving the position of the focus, in which case $\frac{A_1}{A_2}$ is given by the ratio of the laser intensities used. Then the factor above simplifies to

$$F' = \frac{A_1}{A_2} \frac{\int_0^{T_1} dt}{\int_0^{T_2} dt}. \tag{D.5}$$

Appendix E

Measurements of detection efficiency

When one compares the yield of two different processes that produce a different number of hits on the detector, e.g. dissociative and non-dissociative ionization as discussed in Chapter 5, it is necessary to correct for the different detection efficiencies. This correction is also necessary when comparing two different breakup channels, for example A^++B and A+B^+ dissociation channels of molecule AB^+ [145]. To that end, it is important to determine the detection efficiency of each particle. In this Appendix, we present how to determine the detection efficiencies of the fragments and the dication ions produced by the interaction of the laser with a CO^+ beam.

In an intense laser field the CO^+ molecules either dissociate or ionize as mentioned in Chapter 5. We choose measurements at lower intensities to evaluate the detection efficiencies as it reduces the number of reaction channels, and therefore the number of equations to be solved [145]. Between the two possible C^++O and C+O^+ dissociation channels, C^++O is favorable at very low intensities due to its lower dissociation threshold. So, we begin with the case where we observed only the C^++O dissociation channel.

E.1 Low intensity: C^++O channel only

In the case that only the C^++O channel is observed, we have three measured numbers *i.e.* M_{C^+O}, M_{C^+}, and M_O. Following the formalism similar to the one outlined in Ref. [145], we

can write the measured number of C^++O coincidences as

$$M_{C^+O} = \varepsilon_{C^+}\varepsilon_O N_{C^+O} \tag{E.1}$$

where ε_{C^+} and ε_O are the efficiencies of detecting the C^+ ions and O atoms, respectively, and N_{C^+O} is the total number of events in the C^++O channels. The measured number of C^+ and O is given by

$$M_{C^+} = \varepsilon_{C^+} N_{C^+O} \tag{E.2}$$

$$M_O = \varepsilon_O N_{C^+O}, \tag{E.3}$$

respectively. We have three equations and three unknowns, which we can solve. Dividing equation (E.1) by equation (E.2) and equation (E.3), respectively, we get

$$\varepsilon_O = \frac{M_{C^+O}}{M_{C^+}} \tag{E.4}$$

$$\varepsilon_{C^+} = \frac{M_{C^+O}}{M_O} \tag{E.5}$$

In addition, the total number of events in the C^++O channel is given by

$$N_{C^+O} = \frac{M_{C^+}}{\varepsilon_{C^+}} \tag{E.6}$$

The uncertainty in the measurement of ε_O is denoted by $\Delta\varepsilon_O$ and given by

$$\Delta\varepsilon_O = \varepsilon_O \sqrt{\left(\frac{\Delta M_{C^+O}}{M_{C^+O}}\right)^2 + \left(\frac{\Delta M_{C^+}}{M_{C^+}}\right)^2} \tag{E.7}$$

In a similar way, we can write the uncertainties in ε_{C^+} and N_{C^+O} as

$$\Delta\varepsilon_{C^+} = \varepsilon_{C^+} \sqrt{\left(\frac{\Delta M_{C^+O}}{M_{C^+O}}\right)^2 + \left(\frac{\Delta M_O}{M_O}\right)^2} \tag{E.8}$$

$$\Delta N_{C^+O} = N_{C^+O} \sqrt{\left(\frac{\Delta M_{C^+}}{M_{C^+}}\right)^2 + \left(\frac{\Delta\varepsilon_{C^+}}{\varepsilon_{C^+}}\right)^2} \tag{E.9}$$

Next we consider the case of intermediate laser intensity such that we observe both C^++O and C+O^+ dissociation channels but ionization channels are negligible.

E.2 Intermediate intensity: both C^++O and C+O^+ channels

When both dissociation C^++O and C+O^+ channels are observed we have five measured numbers: M_{C^+O}, M_{CO^+}, M_{C^+}, M_{O^+} and $M_{C(O)}$. M_{C^+O} and M_{C^+} are defined in Section E.1. In a similar way, we can write the measured number of C+O^+ events in coincidence, M_{CO^+} and the number of O^+ ions M_{O^+}. The measured number of neutrals has an extra term as we have two neutral fragments (C and O) that are indistinguishable by our detector. We thus have the following equations

$$M_{C^+O} = \varepsilon_{C^+}\varepsilon_O N_{C^+O} \tag{E.10}$$

$$M_{C^+} = \varepsilon_{C^+} N_{C^+O} \tag{E.11}$$

$$M_{CO^+} = \varepsilon_C \varepsilon_{O^+} N_{CO^+} \tag{E.12}$$

$$M_{O^+} = \varepsilon_{O^+} N_{CO^+} \tag{E.13}$$

$$M_{C(O)} = \varepsilon_C N_{CO^+} + \varepsilon_O N_{C^+O} \tag{E.14}$$

where ε_C and ε_{O^+} are the efficiencies of detecting the C and O^+ fragments and N_{CO^+} is the total number of events in the C+O^+ channel. Thus for the case considered here, we have five equations and six unknowns ε_{C^+}, ε_O, ε_C, ε_{O^+}, N_{C^+O}, and N_{CO^+}. By using the solutions for ε_{C^+} from Section E.1 we can overcome this deficiency and solve for all unknowns without the need for any assumptions. Note that we can solve for ε_O independently and verify that it is similar to what was obtained from equation (E.4) in Section E.1.

We solve for ε_C upon dividing equation (E.12) by equation (E.13), *i.e.*

$$\varepsilon_C = \frac{M_{CO^+}}{M_{O^+}} \tag{E.15}$$

We solve for N_{CO^+} using equation (E.14) as

$$N_{CO^+} = \frac{M_{C(O)} - \varepsilon_O N_{C^+O}}{\varepsilon_C} = \frac{\varepsilon_{C^+} M_{C(O)} - \varepsilon_O M_{C^+}}{\varepsilon_C \varepsilon_{C^+}} \tag{E.16}$$

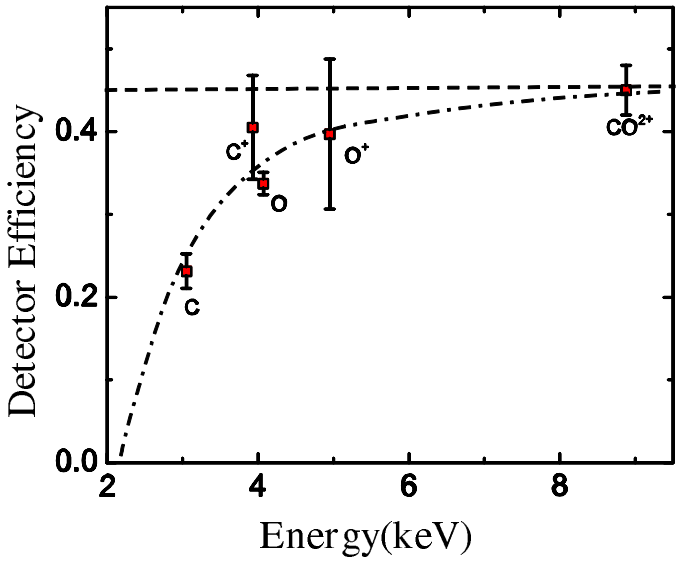

Figure E.1: *Detection efficiency of CO^+ beam fragments and CO^{2+} dications as a function of energy. Error bars indicate the statistical errors. The dashed horizontal line represents the maximum detection efficiency defined by the open area ratio of our detector. The dash-dotted curve indicates the qualitative detector efficiency as a function of the particle energy and is shown here as a guide.*

where N_{C^+O} is replaced with the value found by using equation (E.11). The efficiency ε_{O^+} of detecting O^+ is found, by substitution of equation (E.16) into equation (E.13), to be

$$\varepsilon_{O^+} = \frac{M_{O^+}}{N_{CO^+}} = \frac{M_{O^+}\varepsilon_C\varepsilon_{C^+}}{\varepsilon_{C^+}M_{C(O)} - \varepsilon_O M_{C^+}} \tag{E.17}$$

We can also write the measured number of dications ($M_{CO^{2+}}$) as

$$M_{CO^{2+}} = \varepsilon_{CO^{2+}} N_{CO^{2+}}, \tag{E.18}$$

where $\varepsilon_{CO^{2+}}$ is the efficiency of detecting CO^{2+} and $N_{CO^{2+}}$ is the total number of CO^{2+} produced in the laser molecule interaction. Obviously, $\varepsilon_{CO^{2+}}$ can not be evaluated from equation (E.18) as $N_{CO^{2+}}$ is not known, therefore it is necessary to estimate it. We base this estimate on the known fact that the efficiency of detecting particles depends on their impact energy on the detector [146] as indicated by a dash-dotted curve in Fig. E.1. For CO^{2+} dications the impact energy will be much higher than the fragment energies as indicated

by the example in Fig. E.1. We expect the efficiency $\varepsilon_{CO^{2+}}$ to be higher or similar to ε_{C^+} and ε_{O^+}, but it can not be more than the open area ratio of our detector (which is about 45% for our present detector and is denoted by a dashed line in Fig. E.1). Thus, by using these lower and upper limits as a guide we estimate $\varepsilon_{CO^{2+}}$ to be 0.43±0.03. These detection efficiencies were used in Section 5.2.